Singularities in Gravitational Lensing

Ashish Kumar Meena

A thesis submitted for the partial fulfillment of

the degree of Doctor of Philosophy

Department of Physical Sciences,

Indian Institute of Science Education and Research Mohali

Knowledge city, Sector 81, SAS Nagar, Manauli PO, Mohali 140306, Punjab, India.

May 2021

Declaration

The work presented in this thesis has been carried out by me under the guidance of Prof. Jasjeet Singh Bagla at the Indian Institute of Science Education and Research, Mohali. This work has not been submitted in part or in full for a degree, a diploma, or a fellowship to any other university or institute. Whenever contributions of others are involved, every effort is made to indicate this clearly, with due acknowledgment of collaborative research and discussions. This thesis is a bonafide record of original work done by me and all sources listed within have been detailed in the bibliography.

Ashish Kumar Meena
(Candidate)

In my capacity as the supervisor of the candidate's thesis work, I certify that the above statements by the candidate are true to the best of my knowledge.

Prof. Jasjeet Singh Bagla
(Supervisor)

Acknowledgements

Initially, I thought that I should skip writing acknowledgment as I am not very good at this, and (I think) this is not easy. But then I realized that there are people who helped and supported me a lot during the last five years, and I should thank them properly at least once before finishing this journey.

First and foremost, I would like to thank and express my sincere gratitude towards my Ph.D. guide, Prof. Jasjeet Singh Bagla, for introducing gravitational lensing in my life as my thesis project. If he introduced me to something else, I am not sure whether it would have been as much fun as lensing is for me. I would also like to thank him for his continuous support and guidance throughout my PhD. Whenever I thought of some possible problem, he always listened to me very patiently and helped in further refining the problem. He always encouraged me to explore and try to solve different problems by myself and always gave me complete freedom in choosing the project on which I wanted to work.

I would like to thank my doctoral committee, Dr. Harvinder Kaur Jassal, Prof. Sudeshna Sinha, for fruitful discussions during committee meetings, and Prof. Sandeep Sahijpal from Panjab University for their valuable suggestions during annual review meetings. I am also very grateful to Prof. Liliya LR Williams from University of Minnesota, USA, for providing the mass models for the HFF clusters and answering my queries (a lot) related to their mass models. I would also like to thank Dr. Adi Zitrin from the Ben-Gurion University of the Negev, Isreal, for answering queries related to HFF cluster mass models provided by their group. I would also like to thank all of the members of the astrophysics group at IISER Mohali.

It was a wonderful experience to work with Agniva Ghosh and Prof. Liliya LR Williams from University of Minnesota, USA, and Anuj Mishra, Dr. Anupreeta More, and Prof. Sukanta Bose from IUCAA Pune. I would like to thank Dr. Anupreeta More for hosting my visits to IUCAA, Pune, and discussing several problems related to strong lensing and microlensing. Thanks to these visits, I was able to meet and discuss my work with various people.

I would like to acknowledge the funding support that I have received from the Council of Scientific and Industrial Research (CSIR) for carrying out my research. I would like

to acknowledge HPC@IISERM for their computational facility and thank people from the IISER computer center for their continuous help. I would like to acknowledge the IISER Mohali library for its facilities, which were very helpful during my coursework.

Finally, I would like to thank my family for everything.

Abstract

Image formation near point singularities in strong gravitational lensing is a less explored field as the number of such lensed systems is small. However, with the ongoing and upcoming surveys, the number of strong lens systems is expected to increase by more than several orders of magnitude. Hence, the probability of observation of strong lens systems with image formation near point singularities is also expected to increase. Thus, it is timely to explore these point singularities in strong lensing. In this thesis, we look at the various properties of point singularities and the possibility of their detection with upcoming facilities. We also study the effects of strong lensing and microlensing on the gravitational wave signals. The work reported in this thesis is as follows.

Finding Singularities in Gravitational Lensing

In order to study the point singularities in detail, the first step is to locate these singularities for a given lens model. In this work, we developed an algorithm to find various point singularities (swallowtail, hyperbolic umbilic, elliptic umbilic) in strong gravitational lensing. The output of our algorithm is a singularity map comprising of A_3-lines and all the point singularities for the given lens model. Such a singularity map locates all the regions in the lens plane with high magnification. Hence, these are optimal sites for deep surveys to probe the high redshift universe. We have applied and validated our algorithm in the case of ideal and actual lenses. In this work, we have also studied the stability of the point singularities in presence of external effects in ideal lens models. We find that the hyperbolic umbilic is least sensitive to the external effects, followed by swallowtail and elliptic umbilic, respectively. We also find that the length of A_3-lines also increases in the presence of external effects.

Exotic Image Formation in Cluster Lenses – I: Cross-Section

In this work, we have applied our algorithm to ten different cluster lenses. Out of these ten clusters, five were chosen from the *Hubble Frontier Fields* (HFF) survey and five were selected from the *Reionization Lensing Cluster Survey* (RELICS). In these clusters, we have identified regions with high magnification for sources up to redshift ten. To determine the dependence of unstable (point) singularities on the lens mass model reconstruction techniques, we compared singularity maps corresponding to the different mass models (provided by various groups in the HFF survey) for each cluster lens. We find that the non-parametric (free-form) lens mass reconstruction method yields the least number of point singularities. In contrast, mass models reconstructed by various groups using a parametric approach have a significantly larger number of point singularities. We also estimate the expected number of galaxies lying near these unstable (point) singularities, which can be observed with the *James Webb Space Telescope* (JWST). We find that we expect to get at least one hyperbolic umbilic and one swallowtail image formation for a source at $z > 1$ for every five clusters with JWST.

Exotic Image Formation in Cluster Lenses – II: Uncertainties

Due to the finite amount of observational data, the best-fit parameters corresponding to the reconstructed cluster mass have uncertainties. In turn, these uncertainties affect the inferences made from these mass models. In this work, we studied the effect of such uncertainties on the singularity maps in simulated and actual galaxy clusters. The mass models for both simulated and real clusters have been constructed using Grale. We find that the final best-fit mass models created using Grale give the simplest singularity maps and a lower limit on the number of point singularities that a lens has to offer. Hence, the estimates of point singularity cross-section presented in our earlier work is the lower limit. The simple nature of these singularity maps also puts a lower limit on the number of three image (tangential and radial) arcs that a cluster lens has to offer. Hence, we estimate the number of galaxy sources giving rise to the three image arcs, which can be observed with the *James Webb Space Telescope* (JWST). We find that we expect to observe at least 20-30 tangential and 5-10 radial three-image arcs in the Hubble Frontier Fields cluster lenses with JWST with $m_{AB} = 29$.

Gravitational lensing of gravitational waves: wave nature and prospects for detection

We discuss the gravitational lensing of gravitational wave (GW) signals from coalescing binaries. We delineate the regime where wave effects are significant from the regime where geometric limit can be used. Further, we focus on the combined effect of strong lensing and microlensing. We find that microlensing combined with strong lensing can introduce time varying phase shift in the signal and hence can lead to significant differences in the signal observed for different images produced by strong lensing. This, coupled with the coarse localization of signal source in the sky for GW detections, can make it difficult to identify the common origin of signal corresponding to different images and use observables like time delay. Sources of gravitational waves can undergo microlensing due to lenses in the disc/halo of the Galaxy, or due to lenses in an intervening galaxy even in absence of strong lensing.

List of Publications

This thesis is mainly based on the following publications:

- **Meena, A. K.**, Bagla J. S., "Finding singularities in gravitational lensing", **MNRAS**, 492, 3294 (2020).
- **Meena, A. K.**, Bagla J. S., "Exotic Image Formation in Strong Gravitational Lensing by Clusters of Galaxies. I: Cross-Section", **MNRAS**, 503, 2097 (2021).
- **Meena, A. K.**, Ghosh, A., Bagla J. S., Williams, L. L. R., "Exotic Image Formation in Strong Gravitational Lensing by Clusters of Galaxies. II: Uncertainties", **2103.13617**, Submitted to MNRAS.
- **Meena, A. K.**, Bagla J. S., "Gravitational lensing of gravitational waves: wave nature and prospects for detection", **MNRAS**, 492, 1127 (2020).

Other work, done during Ph.D., which are not part of this thesis:

- Mishra, A., **Meena, A. K.**, More, A., Bose,S., Bagla J. S., "Gravitational Lensing of Gravitational Waves: Effect of Microlens Population in Lensing Galaxies", **2102.03946**, Submitted to MNRAS.

Contents

Chapter 1

Introduction

This chapter provides a brief overview of gravitational lensing and describes various notions related to it. This chapter is organized as follows: Section 1.1 contains a very brief history of gravitational lensing. Section 1.2 and 1.3 contain discussion of deflection of light in Newtonian and General theory of gravity, respectively. Relevant basics of cosmology for lensing are reviewed in Section 1.4. Section 1.5 describes the basics of the gravitational lens equation and its various properties. Section 1.6 discusses different type of singularities in gravitational lensing.

1.1 Historic Remarks

The concept of bending of light due to gravity has a fascinating history and goes all the way back to Newton. Newton, in his *Opticks* (the first edition came out in 1704 and later reprinted based on the fourth edition Newton 1952), listed 31 queries to be further explored by upcoming generations, and the first of these queries was: *Do not Bodies act upon Light at a distance, and by their action bend its Rays; and is not this action (cæteris paribus) strongest at the least distance?* In 1783, in a letter to Henry Cavendish, John Michell (Michell, 1784) discussed the possibility of light emitted by a body falling onto itself under its gravity. Henry Cavendish did calculate the light deflection due to gravity but never published (see Will 1988 for more details). Independent of Michell and Cavendish, in 1795, Peter Simon Laplace (de Laplace, 1795, please also see appendix A in Hawking & Ellis 1973) also arrived at the similar idea of light unable to escape its source due to gravity. In 1801, Johann Von Soldner (Soldner, 1804, please also see Jaki 1978) published a paper with a detailed calculation about the bending of light in Newtonian theory. However, no observational follow-up was possible at

that time due to the small expected value of the deflection angle. Later, during most of the 19th century, Newton's corpuscular theory was disfavored due to the success of the wave theory of the light, and along with it the possibility of bending of light as the waves do not have a mass associated with them.

At the beginning of the 20th century, Albert Einstein revived the particle nature of light (Einstein, 1905) and, a few years later, the deflection of light. In 1911, when Einstein was working on his theory of gravity (Einstein, 1911), he came to the same deflection value as Soldner and tried to persuade astronomers to observe this effect. However, the observations could not be successfully finished at that time due to World War I. In 1915, when Einstein finalized his theory of gravity, he revisited the deflection angle calculation to see that the value is twice the value that he got earlier (Einstein, 1915). After that, it became crucial to observe the deflection of light as the results were different from Newton's theory of gravitation, which was consistent with all experiments. In 1919, a team led by F. Dyson and A. Eddington determined the light deflection value due to the Sun during a total solar eclipse (Dyson et al., 1920) (please also see Kennefick 2019 for further details about various aspects of the observation of the 1919 solar eclipse). The final verdict was in favor of Einstein. The exciting thing about all this is that from the time of Newton, people were quite comfortable with the bending of light due to gravity. The only problem that existed was the smallness of the deflection angle, which hindered the observations of the bending of light.

Although the bending of light due to gravity was observationally confirmed, however, owing to the smallness of the deflection angle, in the first half of the 20th century, only a handful of people (excluding Einstein himself) were interested in the phenomena. One of these was F. Zwicky, who pointed out the possibility of deflection of light due to a whole galaxy or a cluster of galaxies (Zwicky, 1937a,b). In the 20th century, development of technology enabled many discoveries in astrophysics, and it became increasingly feasible to look for the deflection of light coming from distant extragalactic sources due to the massive intermediate structures. In 1964, during his Ph.D., Sjur Refsdel looked into light deflection in a cosmological scenario and its applications and pointed out the possibility of measuring the Hubble constant (Refsdal, 1964a,b, 1966a,b). In 1979, the light deflection was observed in a cosmological scenario (Walsh et al., 1979), and an entirely new field to study the universe came into the picture. The light coming from a distant quasar, Q0957+561, was deflected by an intermediate galaxy. Due to this bending of light, multiple images of the background quasar were observed around the deflector galaxy.

Today, light deflection (also known as *gravitational lensing*) is an important tool to

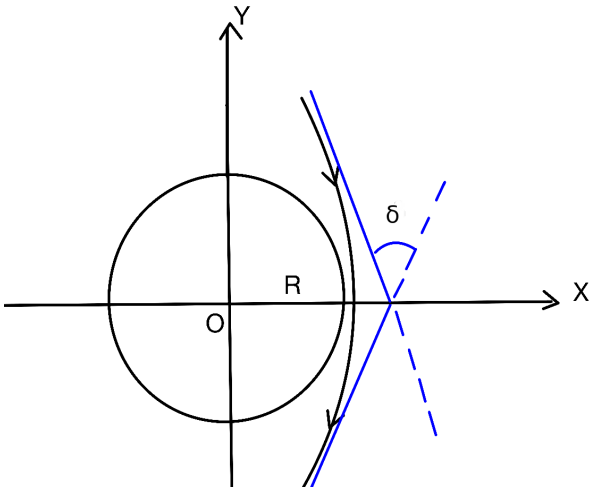

Figure 1.1: Orbit of the light around the Sun: The black solid line represents the path of light near the surface of the Sun. R is the radius of the Sun. The Blue lines represent the asymptotes to the hyperbolic path of the Sun. δ represents the angle by which the light has been deflected due to the gravity of the Sun.

study our Universe. After the discovery of the first lens system in 1979, the field evolved very rapidly. Its applications range from planetary scales to the scale of observable universe. There are more than a dozen books and review articles covering various applications of gravitational lensing. Some of these are: Schneider et al. (1992) (hereafter SEF), Narayan & Bartelmann (1996), Petters et al. (2001), Lewis & Challinor (2006), Ellis (2010), Kneib & Natarajan (2011), Dodelson (2017), Congdon & Keeton (2018). Thanks to gravitational lensing, we are able to map the distribution of visible and dark matter in galaxy clusters (Paraficz et al., 2016), observed very distant galaxies (Coe et al., 2013), and witnessed multiple images of a supernova (Kelly et al., 2016).

1.2 Light Deflection in Newtonian Theory

Let us assume that a light ray coming from a distant star passes near the Sun. As we know, gravity behaves as a central force in Newtonian theory. Hence, the path of the light ray can be described by a hyperbolic orbit around the Sun as the speed of light is significantly greater than the escape velocity for the Sun. As shown in Figure 1.1, the black line shows the hyperbolic path of the light as it passes near the surface of the Sun centered at O. The radius of the Sun is denoted by R. The blue lines represent the asymptotes to the path of the light. Near the Sun, due to gravity, light gets deflected by an angle δ. The eccentricity of the light path (ε) and the deflection angle (δ) are related

to each other as,

$$\delta = 2\sin^{-1}\left(\frac{1}{\varepsilon}\right). \tag{1.1}$$

If the light particles has mass m, total Energy E, and angular momentum L, then the eccentricity (ε) of the path of the light with respect to the center of the Sun is,

$$\varepsilon = \left(1 + \frac{2EL^2}{G^2 m^3 M_s^2}\right)^{1/2} \tag{1.2}$$

where G is the Newton's gravitational constant and M_s is the mass of the Sun. As mentioned above, gravity is a central force, as a result, the total energy (E) and the angular momentum (L) are constants of motion and given as,

$$E = \frac{1}{2}mc^2 - \frac{GmM_s}{R}, \qquad L = mcR, \tag{1.3}$$

where R is the radius of the Sun and c is the speed of light. From Equation (1.2) and (1.3),

$$\varepsilon = \left(1 + \frac{c^2R^2}{G^2M_s^2}\left[c^2 - \frac{2GM_s}{R}\right]\right)^{1/2} \approx \frac{c^2R}{GM_s}. \tag{1.4}$$

The approximation is based on the fact that speed of light is significantly larger than the other terms. Hence, from Equation (1.1) and (1.4), the light deflection angle in Newtonian theory is,

$$\delta = 2\sin^{-1}\left(\frac{GM_s}{c^2R}\right) \approx \frac{2GM_s}{c^2R}$$

$$\boxed{\delta = \frac{2GM_s}{c^2R}.} \tag{1.5}$$

Soldner got this result in 1801 (Soldner, 1804) and Einstein (unaware of Soldner's work) recalculated this result in 1911 (Einstein, 1911) using Equivalence principle. As expected, the deflection of the light ray is directly proportional the total mass of the deflector as the increment in the deflector mass will increase the magnitude of gravitational force on the light. On the other hand, the deflection angle is inversely proportional to the distance of the light ray from the deflector as the gravity becomes weaker as one goes away from the source. However, this is not the correct result. The correct deflection value is twice the above value and can be derived using the Einstein's theory of gravitation, which is discussed in the next section.

1.3 Light Deflection in General Relativity

Hermann Minkowski (Lorentz, 1952) very well describes the crucial difference between Newton's theory of gravity and Einstein's theory of gravity (also known as the *general theory of relativity*) in words as, '*Henceforth space by itself, and time by itself, are doomed to fade away into mere shadows, and only a kind of union of the two will preserve an independent reality*.' Although these words were originally said in the context of special relativity, they are also equally valid for the general theory of relativity. In Newton's theory, space and time are absolute and independent entities, whereas in the (special and) general theory of relativity, space and time do not exist independently, and the properties of their coexistence (generally called as spacetime) can be described by the differential geometry. As a result, in the general theory of relativity, the so-called gravitational force is only an apparent force due to the curved geometry of the spacetime. In general relativity, spacetime geometry around an isolated Sun-like star can be very well described by the Schwarzschild metric (Ryder, 2009),

$$ds^2 = -\left(1-\frac{2GM_s}{rc^2}\right)c^2dt^2 + \frac{1}{\left(1-\frac{2GM_s}{rc^2}\right)}dr^2 + r^2(d\theta^2+\sin^2\theta d\phi^2), \tag{1.6}$$

where ds is the interval, (t,r,θ,ϕ) are the spacetime coordinates, G is the Newton's gravitational constant, M_s is the mass of the Sun, c is the speed of light. In general relativity, the motion of light around the Sun is described by the geodesic equation,

$$\frac{d^2x^\mu}{d\lambda^2} + \Gamma^\mu_{\nu\rho}\frac{dx^\nu}{d\lambda}\frac{dx^\rho}{d\lambda} = 0, \tag{1.7}$$

where λ is an affine parameter. Solving Equation (1.7), for $\mu = 0,2,3$.
For $\mu = 0$,

$$\left(1-\frac{2GM_s}{rc^2}\right)\frac{dt}{d\lambda} = constant = b. \tag{1.8}$$

For $\mu = 2$,

$$\frac{d^2\theta}{d\lambda^2} + \frac{2}{r}\frac{dr}{d\lambda}\frac{d\theta}{d\lambda} - \sin\theta\theta\left(\frac{d\phi}{d\lambda}\right)^2 = 0. \tag{1.9}$$

For $\mu = 3$,

$$\frac{d^2\phi}{d\lambda^2} + \frac{2}{r}\frac{dr}{d\lambda}\frac{d\phi}{d\lambda} + 2\cot\theta\frac{d\theta}{d\lambda}\frac{d\phi}{d\lambda} = 0. \tag{1.10}$$

Consider a geodesic in the equatorial plane ($\theta = \pi/2$) and $d\theta/d\lambda = 0$. Then, from Equation (1.9), $d^2\theta/d\lambda^2 = 0$, as a result, $d\theta/d\lambda$ will always be zero and from (1.10),

$$r^2\frac{d\phi}{d\lambda} = constant = a \quad \Rightarrow \quad \frac{dr}{d\lambda} = \frac{dr}{d\phi}\frac{a}{r^2}. \tag{1.11}$$

As we know, for light $ds^2 = 0$, hence, Equation (1.6) can be written as

$$\left(1-\frac{2GM_s}{rc^2}\right)\left(\frac{dt}{d\lambda}\right)^2-\left(1-\frac{2GM_s}{rc^2}\right)^{-1}\frac{1}{c^2}\left(\frac{dr}{d\lambda}\right)^2 -\frac{r^2}{c^2}\left[\left(\frac{d\theta}{d\lambda}\right)^2+\sin^2\theta\left(\frac{d\phi}{d\lambda}\right)^2\right]=0,$$

using Equation (1.8) and (1.11) and simplifying a little bit gives,

$$\boxed{\frac{d^2}{d\phi^2}\left(\frac{1}{r}\right)+\frac{1}{r}=\frac{3GM_s}{r^2c^2}.} \tag{1.12}$$

Equation (1.12), describes the orbit of light near the Sun or a Sun-like star. As the right hand side is very small compared to one, the equation can be solved iteratively. The zeroth-order solution is

$$\frac{d^2}{d\phi^2}\left(\frac{1}{r}\right)+\frac{1}{r}=0 \quad \Rightarrow \quad \frac{1}{r}=\frac{1}{r_0}\cos\phi, \tag{1.13}$$

corresponding to a straight line. The first-order solution can be calculated by substituting the zeroth-order solution in the right side of Equation (1.12),

$$\frac{d^2}{d\phi^2}\left(\frac{1}{r}\right)+\frac{1}{r}=\frac{3GM_s}{c^2r_0^2}\cos\phi \quad \Rightarrow \quad \frac{1}{r}=\frac{GM_s}{c^2r_0^2}\left(1+\sin^2\theta\right). \tag{1.14}$$

From Equation (1.13) and (1.14), the general solution is,

$$\frac{1}{r}=\frac{1}{r_0}\cos\phi+\frac{GM_s}{c^2r_0^2}\left(1+\sin^2\theta\right). \tag{1.15}$$

Now again considering asymptotes from Figure 1.1, $r\to\infty$, $\phi\to\pm\pi/2+\delta/2$ and from Equation (1.15) $\delta = 4GM_s/r_0c^2$. For light passing from near the surface of the Sun, the closest distance will be equal to the radius of the Sun (R),

$$\boxed{\delta=\frac{4GM_s}{c^2R}.} \tag{1.16}$$

Equation (1.16), represents the deflection of light due to the Sun or a Sun-like star with mass M_s and radius R. Comparing Equation (1.5) and (1.16), one can see that the deflection in the general relativity is twice the deflection in the Newtonian theory.

As one can see from Equation (1.6), the line element becomes singular at the so called Schwarzschild radius $R_{sch} = 2GM_s/c^2$. Our calculation is not valid near the

Schwarzschild radius as the curvature of spacetime near the Schwarzschild radius becomes significant and one will need to solve the geodesic equation explicitly without approximations (Virbhadra & Ellis, 2000). However, near the surface of the Sun, $R_{sch}/R \ll 1$, as a result, the above derived result is valid as it is well within the weak field limit.

1.4 Basic Cosmology

This section briefly discuss the basic cosmology. For an in-depth coverage of cosmology, interested readers are encouraged to look into the following references: Weinberg (1972), Dodelson (2003), Hartle (2003), Ryder (2009).

1.4.1 The Spacetime Metric

According to observations, the Universe is homogeneous and isotropic at large scales ($\gg$100Mpc). In general relativity, such a universe can be described by the Friedmann-Robertson-Walker (FRW) metric,

$$ds^2 = c^2dt^2 - a^2(t)\left[d\chi^2 + f_K^2(\chi)\left(d\theta^2 + \sin^2\theta\, d\phi^2\right)\right], \tag{1.17}$$

where, c is the speed of light. $a(t) = a$ is the time dependent *scale factor* that describes cosmological expansion (or contraction). The scale factor is normalized such that $a(t = t_0) = 1$. (t, χ, θ, ϕ) represent a coordinate system based upon the *physical time* or *cosmic time* t, line-of-sight *comoving distance* χ, and two angular coordinates (θ, ϕ). $f_K(\chi)$ represents the comoving angular diameter distance

$$f_k(\chi) = \begin{cases} \sin\left(\sqrt{K}\chi\right)/\sqrt{K} & K > 0, \\ \chi & K = 0, \\ \sinh\left(\sqrt{-K}\chi\right)/\sqrt{-K} & K < 0, \end{cases}$$

where K is the curvature of space. $K = 1, 0, -1$ implies space with positive, zero (flat), and negative curvature.

1.4.2 The Cosmological Redshift

The definition of the cosmological redshift is based on the light propagation in the FRW metric. Consider a source at a fixed comoving distance χ. For a photon that travels along the null geodesic, from Equation (1.17),

$$d\chi = \frac{cdt}{a} \quad \Rightarrow \quad \chi = c\int \frac{dt}{a}.$$

Let us assume that the source emits a photon at a time t_e and it propagates radially, $(\theta = 0, \phi = 0)$, and it is observed by the observer at a time t_o. A second photon is emitted by the source at a time $t_e + \Delta t_e$ and observed at $t_o + \Delta t_o$. Hence, for a fixed comoving distance,

$$\chi = \int_{t_e}^{t_o} \frac{dt}{a} = \int_{t_e+\Delta t_e}^{t_o+\Delta t_o} \frac{dt}{a}. \tag{1.18}$$

As the comoving distance does not depend on time, the above equation can also be written as,

$$\int_{t_e}^{t_o} \frac{dt}{a} = \left(\int_{t_e}^{t_o} + \int_{t_o}^{t_o+\Delta t_o} - \int_{t_e}^{t_e+\Delta t_e}\right) \frac{dt}{a},$$

which implies

$$\int_{t_o}^{t_o+\Delta t_o} \frac{dt}{a} = \int_{t_e}^{t_e+\Delta t_e} \frac{dt}{a}.$$

For small time intervals,

$$\frac{\Delta t_o}{a_o} = \frac{\Delta t_e}{a_e}. \tag{1.19}$$

Now let us assume that Δt_e is equal to the period of the emitted photon, $\Delta t_e = \lambda_e/c$. Then the relation between the emitted and observed wavelength of the photon is (again assuming $a_o = 1$)

$$(1+z) \equiv \frac{\lambda_o}{\lambda_e} = \frac{1}{a_e}, \tag{1.20}$$

where z is defined as the redshift of the source. In general, the redshift (also known as Doppler shift) of an object is defined as the fractional change in the observed wavelength of the emitted photon due to the radial motion of the object. However, cosmological redshift is not a consequence of the object's motion. Instead, it is a result of the expansion of the Universe itself. In addition to the expansion, if the light source also has a radial motion relative to the observer, then the final redshift will be a combination of both Doppler shift and cosmological redshift.

1.4.3 Cosmological Parameters

One can solve the Einstein's field equation for Equation (1.17) to get the so-called *Friedmann Equations*,

$$H^2(t) \equiv \left(\frac{\dot{a}}{a}\right)^2 = \frac{8\pi \mathrm{G}}{3}\rho - \frac{Kc^2}{a^2}, \tag{1.21}$$

$$\frac{\ddot{a}}{a} = -\frac{4\pi G}{3}(\rho + 3p), \tag{1.22}$$

where G is the Newton's gravitational constant, ρ is the energy density of the Universe at a cosmic time t, and p is the corresponding pressure. The dot represents the derivative with respect to the cosmic time and $H(t)$ is the *Hubble parameter*. The present value of the Hubble parameter is known as the *Hubble constant* and denoted as H_0.

According to observations (Planck Collaboration et al., 2020), our Universe can be very well described by the standard ΛCDM model with the cosmological constant (as the dark energy), cold dark matter, Baryons and Radiation. Hence, the energy density, ρ, in Equation (1.21) has three different components: (i) the pressure-less cold dark matter density and Baryons, ρ_m, (ii) the radiation density, ρ_{rad}, (iii) the cosmological constant, ρ_Λ. Using the continuity equation, these three density values (ρ_m, ρ_{rad}, ρ_Λ) at a cosmic time t can be related to their present values ($\rho_{m,0}$, $\rho_{rad,0}$, ρ_Λ) as

$$\rho_m = \frac{\rho_{m,0}}{a^3}, \qquad \rho_{rad} = \frac{\rho_{rad,0}}{a^4}, \qquad \rho_\Lambda = \rho_\Lambda. \tag{1.23}$$

One can define the *critical density* as

$$\rho_c \equiv \frac{3H^2(t)}{8\pi G} \tag{1.24}$$

and the Friedmann Equation (1.21), can be written as

$$H^2(t) = H_0^2\left(\frac{\Omega_{m,0}}{a^3} + \frac{\Omega_{rad,0}}{a^4} + \Omega_\Lambda\right), \tag{1.25}$$

where $\Omega_{m,0} = \rho_{m,0}/\rho_{c,0}$, $\Omega_{rad,0} = \rho_{rad,0}/\rho_{c,0}$ and $\Omega_\Lambda = \rho_\Lambda/\rho_{c,0}$ are dimensionless density parameters with $\rho_{c,0}$ being the present critical density of the Universe.

In our current work, until mentioned otherwise, the present values of different cosmological parameters are as follows: $K = 0$, $H_0 = 70$ km/s/Mpc, $\Omega_{m,0} = 0.3$, $\Omega_\Lambda = 0.7$, and $\Omega_{rad,0} = 0.0$.

1.4.4 Cosmological Distances

Due to the expansion of the Universe, measures of distances, which would have been the same in a non-expanding universe, are different from each other. However, one cannot say that one is correct and the others are not. One of these is the *comoving distance* between two objects which is mentioned above. The line-of-sight (or radial) comoving distance between two objects is independent of the cosmic time unless they have motion other than the expansion of the Universe. From Equation (1.17), the comoving distance between two objects is defined as

$$\chi = \int d\chi = c \int \frac{dt}{a}. \tag{1.26}$$

Using Equation (1.25), the comoving distance in terms of dimensionless density parameters can be written as,

$$D_c \equiv \chi = \frac{c}{H_0} \int \frac{da}{\sqrt{\frac{\Omega_{m,0}}{a^3} + \frac{\Omega_{rad,0}}{a^4} + \Omega_\Lambda}}. \tag{1.27}$$

Measurement of the angular extent of an object gives another measure of the distance to the object known as the *angular diameter distance* (D_A). The angular diameter distance and the comoving distance are related to each other as

$$D_A = a D_c = \frac{D_c}{1+z} \tag{1.28}$$

Another way to measure distances is to measure the observed flux from an object with known luminosity. The *luminosity distance*, D_L, is related to other distances as (Hogg, 1999)

$$D_L = (1+z) D_C = (1+z)^2 D_A. \tag{1.29}$$

1.5 Basics of Gravitational Lensing

In the last section, we have derived the deflection angle due to a spherically symmetric and static object. However, for most of the astrophysical objects, the assumption of spherical symmetry is not valid. Hence, one needs to have a general lensing formalism applicable for both spherical and non-spherical objects. In subsection 1.5.1, we discuss the general lensing configuration in astrophysics. Later, following SEF, in subsection 1.5.2, we derive the fundamental quantity in lensing, the so-called gravita-

tional lens equation. Various properties of gravitational lens equation are discussed in subsection 1.5.3.

1.5.1 General Lensing Scenario

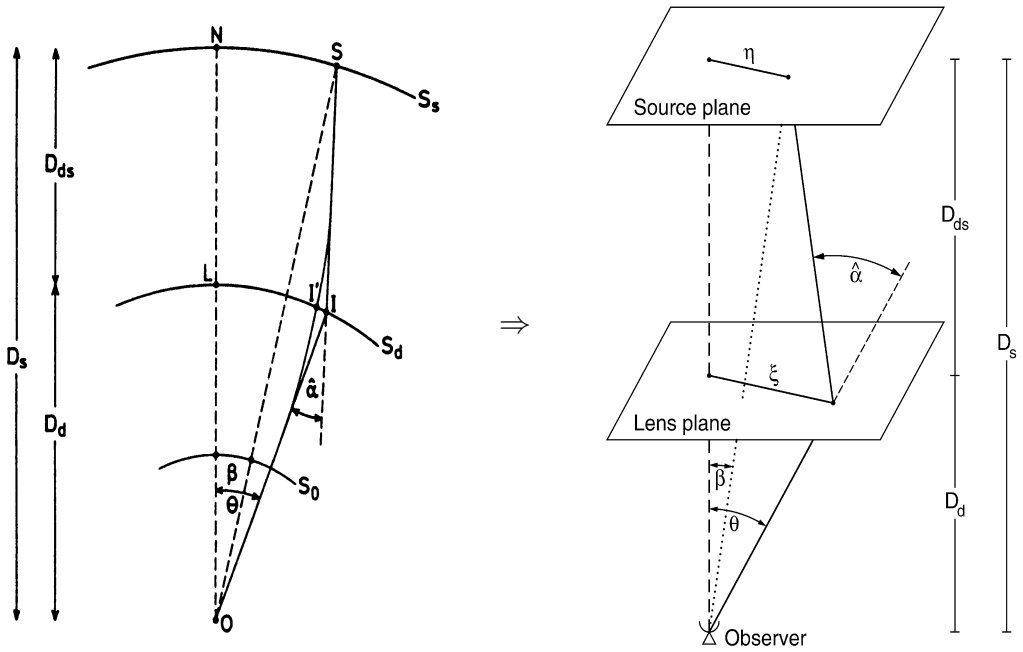

Figure 1.2: Schematic diagram of a general lens system: The left panel shows the typical lens system without approximations. The lens, source, and observer are centered at L, S, and 0, respectively. In the absence (presence) of lensing, the source is located at angle β (θ) with respect to the observer. The right panel is the same lens system with small angle and thin lens approximations. The angular diameter distances from observer to lens, observer to source, and lens to source are represented by D_d, D_s, D_{ds}, respectively. (Image credit: SEF)

As mentioned above, gravitational lensing is the bending of light due to the presence of a massive object along its path. Hence, as shown in the left panel of Figure 1.2, a *gravitational lens system* consists of three components: (i) source (S): object that emits light, (ii) gravitational lens (L): intermediate-mass distribution responsible for the bending of light coming from source, and (iii) observer (O): us. In the left panel of Figure 1.2, OLN represents an arbitrarily defined reference line, the so-called *optical axis*, with respect to which different angles and distances will be measured. The dashed SO line represents the light ray path in the absence of the lens (L) with an angle $\vec{\beta}$ with respect to the optical axis measured by the observer. However, due to the presence of the lens (L), SO is no longer physical and light travels along the SI′O with an angle $\vec{\theta}$ with respect to the optical axis. One can see that SI′O is not a straight line like SO. Instead, it gets curved near the gravitational lens (L). In all of the cases discussed in this thesis, the

deflection angle is very small (of the order of arcseconds). Hence, only a small region around the optical axis needs to be considered. As a result, one can replace the source (S_s) and lens sphere (S_d) by the so-called *source plane* and *lens plane*, respectively, and the light path can be approximated by two asymptotes (SI and IO) to SI′O meeting each other in the lens plane. As a result of this assumpation, one can say that all the deflection $\vec{\hat{\alpha}}$ is taking place in the lens plane.

In principle, the above mentioned approximations are enough to derive the lens equation. However, there is one more approximation, the *thin lens approximation*, which is also very crucial for gravitational lensing. In general, the lens mass distribution is three dimensional in nature. However, the extension of lens mass distribution along the line of sight is very small compared to other relevant scales like D_d, D_{ds}, D_s. Hence, instead of treating the lens mass distribution as three-dimenstional, one can safely assume that lens mass disribution is two dimensional and distributed in the lens plane. With the above mentioned approximations, the left panel in Figure 1.2, can be transformed into the right panel. In the right panel of figure 1.2, the source lies in the source plane, and its distance from the optical axis is given by a two-dimensional vector, $\vec{\eta} = D_s\vec{\beta}$. Similarly, in the lens plane, the distance of the light ray from the optical axis is given by a two-dimensional vector, $\vec{\xi} = D_d\vec{\theta}$, with a deflection angle, $\vec{\hat{\alpha}}$, in the lens plane.

1.5.2 Deflection Angle and Lens Equation

As discussed in section 1.3, the deflection angle due to a point mass lens can be given by Equation (1.16). As one can see from Equation (1.16), the deflection angle is linearly proportional to the mass of the object. As a result, the deflection due to the N point mass lenses, distributed in the lens plane, can be written as a linear superposition,

$$\vec{\hat{\alpha}}(\vec{\xi}) = \sum_{i=1}^{N} \frac{4GM_i}{c^2} \frac{\vec{\xi} - \vec{\xi}_i}{|\vec{\xi} - \vec{\xi}_i|^2}, \tag{1.30}$$

where M_i and $\vec{\xi}_i$ are the mass and position of ith point mass lens, respectively. For a continuous mass distribution, with the projected mass density $\Sigma(\vec{\xi})$, the above equation can be written as,

$$\vec{\hat{\alpha}}(\vec{\xi}) = \frac{4G}{c^2} \int \Sigma(\vec{\xi}')d^2\xi' \frac{\vec{\xi} - \vec{\xi}'}{|\vec{\xi} - \vec{\xi}'|^2}, \tag{1.31}$$

where the integration is over the lens plane. One should keep in mind that the deflection angle written in this form is the consequence of the thin lens approximation and the

weak field limit. One can also see that for general mass distribution, the deflection angle is a vector quantity, unlike the spherically symmetric case discussed above, where only radial dependence in deflection angle was meaningful. Similar to the projected mass density, one can also define the projected lens potential as,

$$\psi(\vec{\xi}) \equiv \int dz\, \phi(\vec{\xi}, z), \tag{1.32}$$

where $\phi(\vec{\xi}, z)$ is the three dimensional potential corresponding to the lens mass distribution. Following SEF, the deflection angle in terms of projected lens potential can be written as,

$$\vec{\hat{\alpha}}(\vec{\xi}) = \vec{\nabla}_{\vec{\xi}} \psi(\vec{\xi}), \tag{1.33}$$

where

$$\psi(\vec{\xi}) = \frac{4G}{c^2} \int d^2\xi'\, \Sigma(\vec{\xi}')\, ln\left(\frac{|\vec{\xi} - \vec{\xi}'|}{\xi_0}\right) + constant \tag{1.34}$$

and ξ_0 is an arbitrary length scale. The lens potential can only be determined up to an additive constant.

Based on the geometry of the Figure 1.2, one can derive a relation between the lensed and unlensed position of the source known as the *lens equation*,

$$\vec{\eta} = \frac{D_s}{D_d}\vec{\xi} - D_{ds}\vec{\hat{\alpha}}(\vec{\xi}), \tag{1.35}$$

where $\vec{\eta}$ is the distance of source in the source plane from the optical axis and $\vec{\xi}$ is the impact parameter of light ray in the lens plane (minimum distance of light ray from the optical axis in the lens plane). It is a common practice to write down the lens equation in dimensionless form by introducing an arbitrary length scale ξ_0 on the lens plane and a corresponding length scale in the source plane $\eta_0 = \xi_0 D_s / D_d$. Using Equation (1.33), (1.34), (1.35), the lens equation in dimensionless form is written as,

$$\vec{y} = \vec{x} - \vec{\alpha}(\vec{x}), \tag{1.36}$$

where $\vec{y} = \vec{\eta}/\eta_0$, $\vec{x} = \vec{\xi}/\xi_0$ are dimensionless source and lens position in the source and lens plane, respectively and the dimensionless potential $\Psi(\vec{x})$ and dimensionless deflection angle $\vec{\alpha}(\vec{x})$ are given as

$$\Psi(\vec{x}) = \frac{1}{\pi}\int d^2x'\, \kappa(\vec{x}')\, ln|\vec{x} - \vec{x}'|,$$

$$\vec{\alpha}(\vec{x}) = \vec{\nabla}_{\vec{x}}\Psi(\vec{x}) = \frac{1}{\pi}\int d^2x'\, \kappa(\vec{x}')\frac{\vec{x} - \vec{x}'}{|\vec{x} - \vec{x}'|^2}, \tag{1.37}$$

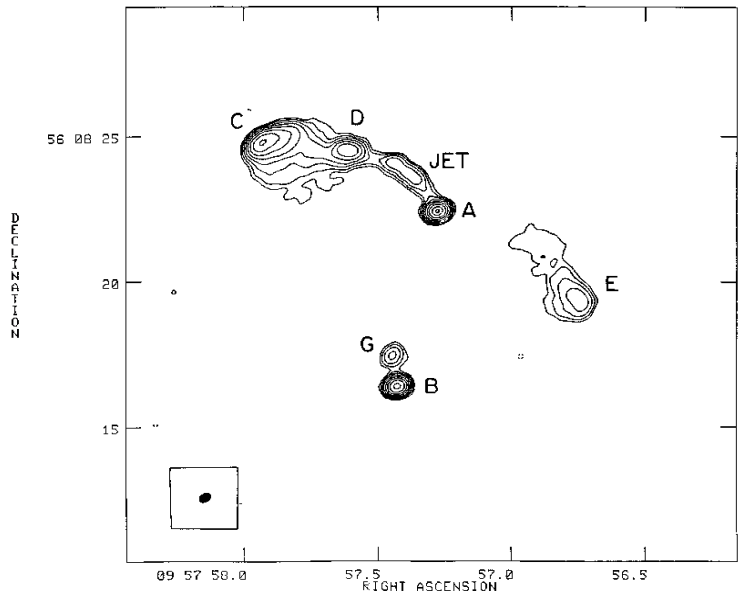

Figure 1.3: Radio image of double quasar Q0957+561 at $\lambda = 6cm$: **A** and **B** represent the two images of the background quasar because of the lensing galaxy **G**. **C**, **D**, **E** are radio structures associated with the quasar image **A**. (Image credit: Roberts et al. 1985)

where $\kappa(\vec{x}) = \Sigma(\vec{x})/\Sigma_{cr}$ is the convergence and $\Sigma_{cr} = \frac{c^2}{4\pi G}\frac{D_s}{D_d D_{ds}}$ is the critical density. We discuss this in more details in the next section.

1.5.3 Properties of Lens Equation

Multiple Image Formation: As one can see from Equation (1.36), the gravitational lens equation describes a mapping from the lens plane to the source plane. For a given lens mass distribution, the mapping is surjective, i.e., for every point in the lens plane, there is a corresponding point in the source plane. However, the inverse is not true, i.e., one point in the source plane can be mapped to multiple points in the lens plane. As a result, due to the presence of a gravitational lens, a distant source can be observed at multiple positions in the sky. This phenomenon is known as multiple image formation, and one of the example of this, Q0957+561 (Walsh et al., 1979), is shown in Figure 1.3. For different lens systems, the number of multiple images of the source is different depending on the lens mass distribution and the overall geometry of the lens system.

Magnification: Apart from giving rise to multiple image formation, gravitational lensing also distorts the individual images and changes their flux. This distortion can be

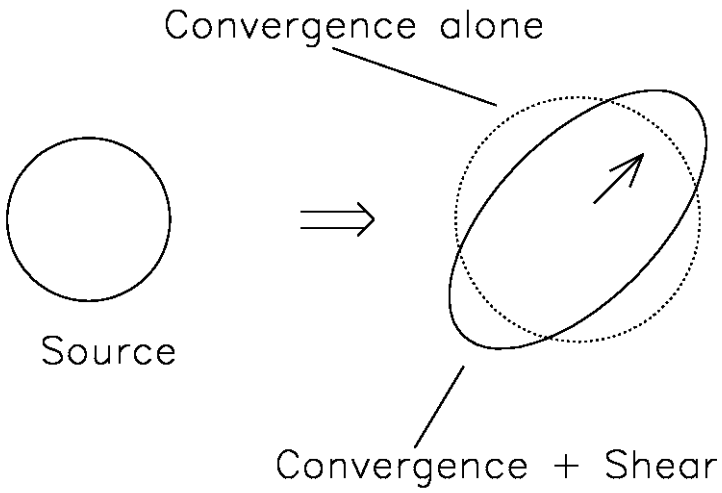

Figure 1.4: Effect of convergence and shear on a circular source: The left panel shows the unlensed circular source. The presence of convergence affect the source size isotropically which is denoted by the dotted circle on the right. On the other hand, presence of both shear and convergence affect the size as well as its shape and transform it into an ellipse. (Image credit: Narayan & Bartelmann 1996)

described by the Jacobian (matrix) of the lens equation,

$$\mathbb{A} \equiv \frac{\partial \vec{y}}{\partial \vec{x}} = \delta_{ij} - \frac{\partial \alpha_i(\vec{x})}{\partial x_j} = \delta_{ij} - \frac{\partial^2 \Psi(\vec{x})}{\partial x_i \partial x_j}, \tag{1.38}$$

where $x_i\,(i = 1,2)$ represents the ith component of the $\vec{x}$ on the lens plane. For convenience, the $\frac{\partial^2 \Psi}{\partial x_i \partial x_j}$ can also be written as Ψ_{ij}. Hence, the Equation (1.38) can be written as

$$\mathbb{A}_{ij} = \delta_{ij} - \Psi_{ij}, \tag{1.39}$$

and one can see that the Jacobian matrix can be written in terms of the second derivatives of the lens potential, Ψ_{ij}, also known as the *deformation tensor*. Now, let us define the so-called *convergence* (κ) and *shear* ($\gamma = (\gamma_1, \gamma_2)$) as

$$\kappa = \frac{1}{2}\left(\Psi_{11} + \Psi_{22}\right), \qquad \gamma_1 = \frac{1}{2}\left(\Psi_{11} - \Psi_{22}\right), \qquad \gamma_2 = \Psi_{12} = \Psi_{21}. \tag{1.40}$$

The Jacobian matrix can be written as

$$\mathbb{A} = \begin{pmatrix} 1-\kappa-\gamma_1 & -\gamma_2 \\ -\gamma_2 & 1-\kappa+\gamma_1 \end{pmatrix} = \begin{pmatrix} 1-\kappa & 0 \\ 0 & 1-\kappa \end{pmatrix} - \begin{pmatrix} \gamma_1 & \gamma_2 \\ \gamma_2 & -\gamma_1 \end{pmatrix}. \tag{1.41}$$

The meaning of convergence and shear can be explained using Equation (1.41). The Ja-

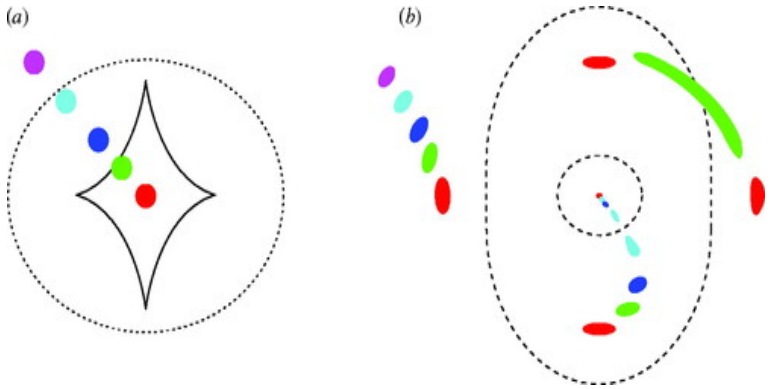

Figure 1.5: Image formation due to an elliptical lens: The panel (a) represents the source plane and the panel (b) represents the lens plane. The dotted and solid lines in the panel (a) represent the radial and tangential caustics, respectively. The inner and outer dotted lines in panel (b) represent the corresponding radial and tangential critical lines. The various colored circles in the panel (a) are different sources and the corresponding images are shown in the panel (b). (Image credit: Ellis 2010)

cobian matrix determines the distortion of images by lensing. As the convergence only appears in the diagonal part of the Jacobian, the distortions induced by it are isotropic in nature. On the other hand, shear stretches the image in a preferred direction based on the values of (γ_1, γ_2). As one can see from Figure 1.4, the unlensed circular source is mapped into a circle if the convergence is non-zero, whereas if shear (or both shear and convergence) is non-zero, then the circular source is mapped into an ellipse with semi-major (a) and semi-minor (b) axis given as

$$a = \frac{r}{1-\kappa-\gamma}, \qquad b = \frac{r}{1-\kappa+\gamma},$$

where r is the radius of the unlensed circular source and $\gamma = \sqrt{\gamma_1^2 + \gamma_2^2}$. The major and minor-axis of the ellipse are aligned with the principal axis of the Jacobian and the amount of stretching depends on the corresponding eigenvalues.

The change in the shape implies a change in the observed solid angle of the source. If there is no emission or absorption of photons during the gravitational lensing, then it implies that the surface brightness of the source remains conserved. Hence, the change in solid angle means a change in the flux coming from the source. From Equation (1.38), the magnification of a lensed image is defined as

$$\mu = \frac{1}{\det\mathbb{A}} = \frac{1}{\lambda_t \lambda_r} = \frac{1}{(1-\kappa-\gamma)(1-\kappa+\gamma)}, \tag{1.42}$$

where λ_t and λ_r are the tangential and radial eigenvalues of the Jacobian of the lens equation describing the tangential and radio distortion of the lensed image, respectively.

Critical lines and caustics: As one can see from above Equation (1.42), the magnification value diverges for an image if $\lambda_t = 0$ or $\lambda_r = 0$ at the image position. Points in the lens plane where $\lambda_t = 0$ ($\lambda_r = 0$) form smooth closed curves and these curves are known as tangential (radial) critical curves. Panel (a) and panel (b) in Figure 1.5 represent the source and lens plane for a typical elliptical lens, respectively. The critical lines for the elliptical lens are shown in the panel (b) by the dashed lines. The outer dashed line is the tangential critical line and the inner dashed line is the radial critical line. The corresponding curve in the source plane are known as caustics and they are not necessarily smooth. The caustics for the elliptical lens are shown in the panel (a). The diamond shaped caustic is known as tangential caustic as it is corresponding to the tangetial critical line in the panel (b). Similarly, the dotted circular line represents the radial caustic corresponding to the radial critical line in the panel (b). One can see that the tangential (diamond-shaped) caustic is made of two different parts, smooth curves (known as folds) and points where two of these smooth curves meet with each other (known as cusps).

If a source lies on the caustics then, in principle, the corresponding images will be infinitely magnified. However, this in not true in reality as all the sources are extended in nature and the total magnification is given as

$$\mu = \frac{\int \mu_p(\vec{y}) I(\vec{y}) d^2y}{\int I(\vec{y}) d^2y}, \tag{1.43}$$

where $I(\vec{y})$ is the surface brightness profile of the source and $\mu_p(\vec{y})$ represents the magnification of a point source located at $\vec{y}$. The above equation always gives a finite magnification value for an extended source.

From Figure 1.5, we also notice that whenever a source crosses a caustic, two additional images appear or disappear in the lens plane. If the source resides outside all of the caustics, then there is only one image in the lens plane (violet source in the panel (a)). As the source crosses the radial caustic (aqua color source in the panel (a)), two additional radially elongated images appear near the radial critical curve in the lens plane, making the total image count in the lens plane three. Once the source crosses the tangential diamond-shaped caustics, two additional tangentially elongated images appear near the tangential critical curve in the lens plane, and the total number of images become five. One can also see that the images are more distorted if the source lies near the caustics.

From the image formation corresponding to various source positions in Figure 1.5,

one can also notice that if the source lies outside the caustics, there is only one image, and the multiple images only form if the source is inside the caustic. Hence, one can divide the gravitational lens systems into two different categories, (I) *Strong gravitational lens system:* (Kochanek, 2006) gravitational lens system with multiple image formation and, (II) *weak gravitational lens system:* (Schneider, 2005) gravitational lens system with only one image formation. Although there are other categories of lensing like *Microlensing* (Wambsganss, 2006), *Femtolensing* (Ulmer & Goodman, 1995), but as these are not relevant for this thesis, we are not going to define these categories.

Time Delay: In the case of light deflection, the light ray follows a longer path compared to the undeflected light ray. Hence, the time taken by light to reach the observer from the source will be greater than the time taken by the undeflected light ray. This extra time taken by light is known as the *geometric time delay*. Apart from the geometric time delay, the presence of the lens itself introduces an additional time delay known as the *Shapiro time delay*. As a result, following SEF, the total time delay with respect to the undeflected light ray is given as

$$\begin{aligned} T\left(\vec{x},\vec{y}\right) =& \frac{\xi_0^2}{c}\frac{D_s}{D_d D_{ds}}\left(1+z_d\right)\varphi\left(\vec{x},\vec{y}\right) \\ =& \frac{\xi_0^2}{c}\frac{D_s}{D_d D_{ds}}\left(1+z_d\right)\left[\frac{\left(\vec{x}-\vec{y}\right)^2}{2}-\Psi\left(\vec{x}\right)\right], \end{aligned} \tag{1.44}$$

where different symbols have their usual meaning as defined above. The first term in the square bracket represents the contribution from the geometric time delay and the second term represents the Shapiro time delay. $\varphi\left(\vec{x},\vec{y}\right)$ is a scalar function known as the *Fermat potential* (Schneider, 1985; Blandford & Narayan, 1986). One can see that the lens Equation (1.36) satisfies the condition $\nabla_x\varphi = 0$, hence, the stationary points of the Fermat potential represent the solutions of lens equations.

One cannot measure the time delay in the absence of the lens. Hence, Equation (1.44) is not an observational quantity. Instead, one can only measure the time delay between two images given by

$$\Delta T_{ij} = \frac{\xi_0^2}{c}\frac{D_s}{D_d D_{ds}}\left(1+z_d\right)\left[\varphi\left(\vec{x}_i,\vec{y}\right)-\varphi\left(\vec{x}_j,\vec{y}\right)\right], \tag{1.45}$$

where $\varphi\left(\vec{x}_i,\vec{y}\right)$ and $\varphi\left(\vec{x}_j,\vec{y}\right)$ are the Fermat potentials corresponding to ith and jth images, respectively.

Image Type: From the definition of the Fermat potential, for a given value of $\vec{y}$, it defines a two-dimensional surface in $\vec{x}$. The *ordinary images* (when the source does not

Figure 1.6: Parity of different type of images: The left most circle shows the unlensed source. The '+' and '-' represent the sign of eigenvalue of Jacobian matrix. The '+ +' represents the minima image. The '- -' represents the maxima image. The '+ -' and '- +' represent the saddle images.

lie on a caustic) are the stationary points ($\nabla_x \varphi = 0$) on this two-dimensional surface and the coresponding magnification matrix is $\mathbb{A} = \varphi_{ij}$. Based on the sign of eigenvalues of Jacobian (1.38), these ordinary images can be divided into three types:

- Type I: Minina Image: Minima point of Fermat potential,
  - Condition: $\det\mathbb{A} > 0$ and $\mathrm{tr}\mathbb{A} > 0$
- Type II: Saddle Image: Saddle point of Fermat potential,
  - Condition: $\det\mathbb{A} < 0$
- Type III: Maxima Image: Maxima point of Fermat potential.
  - Condition: $\det\mathbb{A} > 0$ and $\mathrm{tr}\mathbb{A} < 0$

The minima and maxima images ($\det\mathbb{A} > 0$) have a positive parity, whereas the saddle image ($\det\mathbb{A} < 0$) has negative parity. The meaning of parity can be further understood from Figure 1.6. The leftmost circle represents the unlensed source. The source has been divided into four quadrants with different colors. The '+' and '-' symbol represent the sign of the eigenvalue. The next figure with '+ +' represents the minima type image. One can see that the unlensed source and the minima image are similar to each other. But the '- -' image, which denotes the maxima image, is rotated by an angle of 180°. The saddle images '+ -' and '- +' are the mirror images of the unlensed source with respect to the y and x axis, respectively.

1.6 Image Formation near Critical Points

Gravitational lens equation defines a gradient mapping, $f : \mathbb{R}^2 \to \mathbb{R}^2$, from lens plane ($\vec{x}$) to source plane ($\vec{y}$). This mapping can also be described by the Fermat potential,

$$\varphi(\vec{x},\vec{y};\vec{p}) = \frac{(\vec{x}-\vec{y})^2}{2} - \Psi(\vec{x};\vec{p}), \tag{1.46}$$

where $\vec{p}$ denotes the parameters of the lens potential. For given $(\vec{y},\vec{p})$ the image positions are the stationary points ($\nabla_x\varphi = 0$) of the Fermat potential. At ordinary images, the $\det\mathbb{A} \neq 0$, hence, the lens mapping is locally invertible. As a result, for such images, the number of images in the lens plane remains a constant under an infinitesimal change in $(\vec{y},\vec{p})$.

However, the same does not hold for the *critical images* (images formed on critical curves) as the $\mathbb{D} \equiv \det\mathbb{A} = 0$, and an infinitesimal change in $(\vec{y},\vec{p})$ can lead to a change in the observed number of lensed images. Such violent discontinuous variations in the final state of the system, given the smooth continuous changes in the initial state of the system, are known as catastrophes, and their study comes under the so-called catastrophe theory (Stewart, 1982; Arnold, 1983; Gilmore, 2007) A detailed discussion of singularities in gravitational lensing is given in Blandford & Narayan (1986); Schneider & Weiss (1986); Petters et al. (2001); Kovner (1987) and chapter 6 of SEF. Here, we will only review the basics of the theory.

As $\mathbb{D} = 0$ for a critical image, the corresponding Jacobian matrix, $\mathbb{A}$, either has rank 1 (one vanishing eigenvalue) or rank 0 (two vanishing eigenvalues). If, for a given $\left(\vec{x}^{(0)},\vec{p}^{(0)}\right)$, the Jacobian matrix has a rank one ($\mathrm{rank}(\mathbb{A}) = 1$ and $\mathbb{A}_{22} = 0$), and $\nabla\mathbb{D} \neq 0$. Then, by introducing a cartesian coordinate system at $x^{(0)}$ in the lens plane and at $y^{(0)}$ in the source plane such that the x and y-axis are parallel to each other, one can see that x_2 direction get annihilated due to $\mathbb{A}_{22} = 0$. In such a case, one can introduce a second direction at the $x^{(0)}$ along the critical curve given by $\mathbb{D} = 0$. The normal vector to the critical curve at $x^{(0)}$ is given by

$$\nabla\mathbb{D}^{(0)} = \varphi_{11}^{(0)}\left(\varphi_{221}^{(0)},\varphi_{222}^{(0)}\right),$$

and the corresponding tangent vector is,

$$\vec{\mathrm{T}}^{(0)} = R\left(\frac{\pi}{2}\right)\nabla\mathbb{D}^{(0)} = \varphi_{11}^{(0)}\left(-\varphi_{222}^{(0)},\varphi_{122}^{(0)}\right).$$

Again due to the $\mathbb{A}_{22} = 0$, there are two distinct possibilities

$$\varphi^{(0)}_{222} \neq 0 \quad \Rightarrow \quad \mathbb{A}^{(0)}.\vec{\mathrm{T}}^{(0)} \neq 0, \tag{1.47}$$

and

$$\varphi^{(0)}_{222} = 0 \quad \Rightarrow \quad \mathbb{A}^{(0)}.\vec{\mathrm{T}}^{(0)} = 0. \tag{1.48}$$

The first condition, Equation (1.47), represents the points on the critical lines in the lens plane that have a well-defined tangent vector at the corresponding caustic points in the source plane. These points in the source plane form smooth curves known as the *folds*. On the other hand, the second condition, Equation (1.48), marks the points in the source plane where the tangent vector is not necessarily well-defined. Such points are known as *cusp* points in the source plane.

1.6.1 Fold

As mentioned above, the fold is described by

$$\mathbb{D}^{(0)} = 0, \quad \mathrm{tr}\mathbb{A} \neq 0, \quad \nabla\mathbb{D} \neq 0, \quad \mathbb{A}^{(0)}.\vec{\mathrm{T}}^{(0)} \neq 0. \tag{1.49}$$

The lens mapping near the lens plane can be described by Taylor series expansion of the Fermat potential and dropping the higher degree insignificant terms (please see Section 6.2 in SEF for rules of truncating the Taylor series) as

$$\begin{aligned} y_1 &= \varphi^{(0)}_{11} x_1 + \frac{1}{2}\varphi^{(0)}_{122} x_2^2 + \varphi^{(0)}_{112} x_1 x_2, \\ y_2 &= \frac{1}{2}\varphi^{(0)}_{112} x_1^2 + \varphi^{(0)}_{122} x_1 x_2 + \frac{1}{2}\varphi^{(0)}_{222} x_2^2. \end{aligned} \tag{1.50}$$

The corresponding Jacobian matrix is given by

$$\mathbb{A} = \begin{pmatrix} \varphi^{(0)}_{11} + \varphi^{(0)}_{112} x_2 & \varphi^{(0)}_{112} x_1 + \varphi^{(0)}_{122} x_2 \\ \varphi^{(0)}_{112} x_1 + \varphi^{(0)}_{122} x_2 & \varphi^{(0)}_{122} x_1 + \varphi^{(0)}_{222} x_2 \end{pmatrix}, \tag{1.51}$$

and the corresponding tangent to the critical curve in the lens plane can be obtained using the condition $\mathbb{A}_{22} = 0$ as

$$\varphi^{(0)}_{122} x_1 + \varphi^{(0)}_{222} x_2 = 0, \tag{1.52}$$

and the corresponding caustic in the source plane can be obtained by using Equations (1.50) and (1.52) as

$$Q(y) := 2(\varphi_{11}^{(0)})^2\varphi_{222}^{(0)}y_2 - \left(\varphi_{122}^{(0)}\varphi_{222}^{(0)}\left[\varphi_{122}^{(0)}\right]^2\right)y_1^2 = 0. \tag{1.53}$$

For a given source position (y_1, y_2) near the fold in the source plane, the corresponding image positions in the lens plane are given as

$$(x_1, x_2) = \left(\frac{\varphi_{222}^{(0)}y_1 - \varphi_{122}^{(0)}y_2}{\varphi_{11}^{(0)}\varphi_{222}^{(0)}}, \frac{-\varphi_{122}^{(0)}y_1 \pm \sqrt{Q(\vec{y})}}{\varphi_{11}^{(0)}\varphi_{222}^{(0)}}\right). \tag{1.54}$$

If the $Q < 0$, then there is no real image of the source in the image plane whereas if the $Q > 0$, then there are two images. Here the images near the region of interest are considered and it is possible that there may be other images away from this region. This can been seen in Figure 1.5, where two additional images appear in the image plane when the source crosses a fold in the source plane and there were extra images far from the region where these new images appear.

Using Equation (1.50), (1.51), and (1.52), one can calculate the variation of magnification near fold singularities in lens plane as

$$|\mu| = \frac{1}{|\varphi_{11}^{(0)}|\sqrt{2\varphi_{222}^{(0)}\Delta y_2}}, \tag{1.55}$$

where Δy_2 is the normal ($y_1 = 0$) distance from fold in the source plane. The corresponding relation in the lens plane is given as

$$|\mu| = \frac{1}{|\varphi_{11}^{(0)}||\varphi_{222}^{(0)}|\Delta x_2}, \tag{1.56}$$

where the Δx_2 is the image distance from the critical line in the lens plane. This formula represents the magnification of the images that are near the critical line. In order to get total magnification, we need to include any other images in the lens plane.

1.6.2 Cusp

Unlike folds, at a cusp point, the tangent vector in the source plane cannot be uniquely defined as the tangent vector is annihilated by the $\mathbb{A}_{22} = 0$ condition. The cusp points

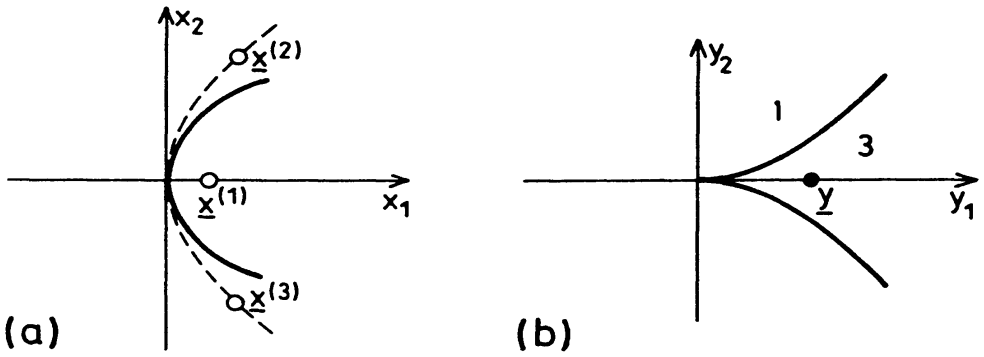

Figure 1.7: The critical curves (a) in the lens plane and the corresponding caustics structure (b) in the source plane near a cusp singularity. Inside and outside of the caustic the source will have three and one image as marked in the panel(b). The dotted line represents the path along which the outer images will move and merge with the inner image as source moves towards the origin from the inside of the caustic. (Image credit: SEF)

are described by

$$\mathbb{D}^{(0)} = 0, \quad \mathrm{tr}\mathbb{A} \neq 0, \quad \nabla\mathbb{D} \neq 0, \quad \mathbb{A}^{(0)}.\vec{\mathrm{T}}^{(0)} = 0. \tag{1.57}$$

Again, retaining the leading order terms in the Taylor series leads to the lens mapping

$$\begin{aligned} y_1 &= \varphi^{(0)}_{11} x_1 + \frac{1}{2}\varphi^{(0)}_{222} x_2^2 + \varphi^{(0)}_{112} x_1 x_2, \\ y_2 &= \frac{1}{2}\varphi^{(0)}_{112} x_1^2 + \varphi^{(0)}_{2222} x_1 x_2 + \frac{1}{6} x_2^3, \end{aligned} \tag{1.58}$$

and the corresponding Jacobian is

$$\mathbb{A} = \begin{pmatrix} \varphi^{(0)}_{11} + \varphi^{(0)}_{112} x_2 & \varphi^{(0)}_{112} x_1 + \varphi^{(0)}_{122} x_2 \\ \varphi^{(0)}_{112} x_1 + \varphi^{(0)}_{122} x_2 & \varphi^{(0)}_{122} x_1 + \frac{1}{2}\varphi^{(0)}_{2222} x_2^2 \end{pmatrix}. \tag{1.59}$$

The critical curve and caustic equations can be obtained using the condition $\mathbb{D} = 0$ as given in Section 6.2 of SEF and as shown in Figure 1.7. As one can see, the critical line in the image plane is a parabola whereas the corresponding source plane shows a cusp connecting two fold lines. The number of images for a given source position are also denoted in the source plane. The dotted line represents the path of the images $x^{(2)}$ and $x^{(3)}$ as we move the source towards the origin. Once source reaches the origin, $x^{(2)}$ and $x^{(3)}$ merges with $x^{(1)}$ and becomes one image. The position of these three images as a

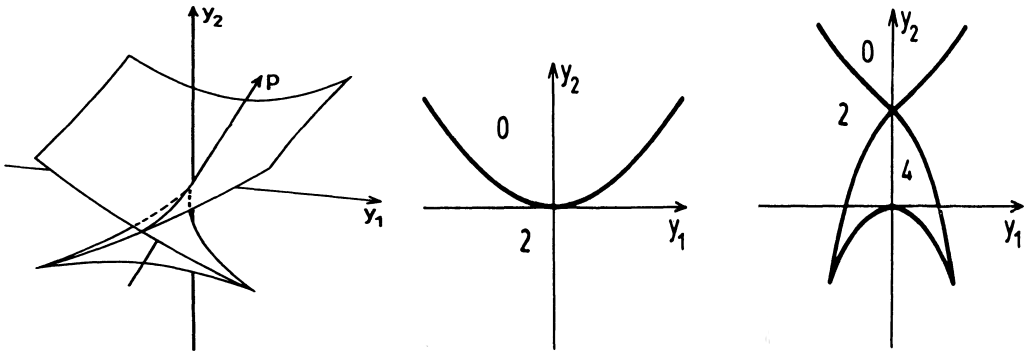

Figure 1.8: Caustic structure near a swallowtail singularity: The left panel represents the caustic structure in source plane with one control parameter, p, at the third axis. The middle panel and the right panel represent the caustic structure for two different value of $p \leq 0$ and $p > 0$, respectively. The different numerical values in the middle and right panel represent the image multiplicity of the source. (Image credit: SEF)

function of source position are given as

$$\vec{x}^{(1)} = \left(\frac{y_1}{c}, 0\right),$$

$$\vec{x}^{(2,3)} = \left(\frac{\varphi^{(0)}_{2222} y_1/3}{\varphi^{(0)}_{11}\varphi^{(0)}_{2222}/3 - \left[\varphi^{(0)}_{122}\right]^2}, \pm \sqrt{\frac{2y_1\varphi^{(0)}_{122}}{\varphi^{(0)}_{11}\varphi^{(0)}_{2222}/3 - \left[\varphi^{(0)}_{122}\right]^2}} \right), \tag{1.60}$$

and the corresponding magnification value are given as

$$\mu^{(1)} = \frac{1}{\varphi^{(0)}_{122} y_1}, \quad \mu^{(2,3)} = -\frac{1}{2\varphi^{(0)}_{122} y_1}. \tag{1.61}$$

One can see that the $x^{(1)}$ image has the opposite parity compared to the $x^{(2)}$ and $x^{(3)}$ and near the cusp the total magnification of $x^{(2)}$ and $x^{(3)}$ is equal to the magnification of $x^{(1)}$.

The fold and cusp are the only *stable* singularities of the lens mapping, i.e., slight perturbation in the parameter $p^{(0)}$ values cannot make the fold and cusp disappear entirely from the source plane. Instead, such a change can only shift the position of the fold and cusp in the source plane. A very simple example of this is the redshift evolution of the fold and cusp. The fact that change in the redshift only change the position of the fold and cusp in the source plane implies their stability. Other singularities of the lens mapping discussed in the following subsections are the *unstable* singularities of the lens mapping, i.e., a small perturbation in the lens system parameters can remove these singularities from the lens mapping entirely, leaving only fold and cusp.

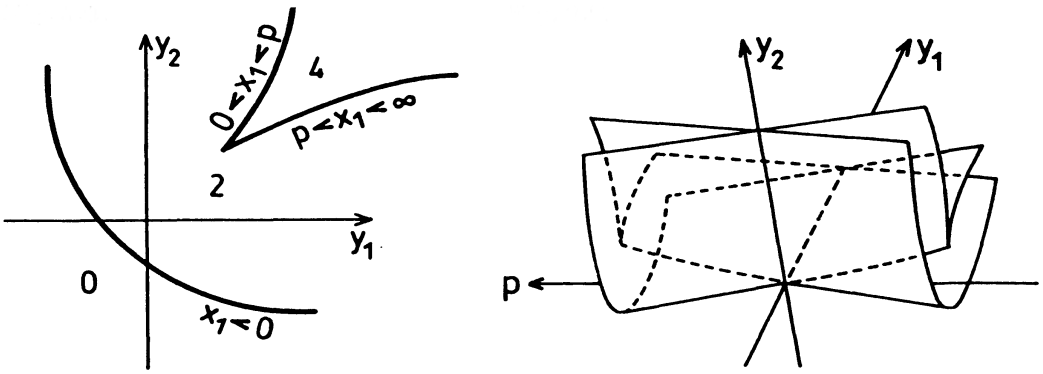

Figure 1.9: Caustic structure near an hyperbolic umbilic: The left panel represents the caustic structure for one specific value of control parameter p in the source plane. The different numerical values represent the image multiplicity of the source. The right panel shows the large caustic in $(\vec{y}, p)$-space. (Image credit: SEF)

1.6.3 Swallowtail

A swallowtail kind of singularity is given by the condition,

$$\mathbb{A}^{(0)}.\vec{\mathrm{T}}^{(0)} = 0, \quad (\vec{\mathrm{T}}.\nabla(\mathbb{A}.\vec{\mathrm{T}}))^{(0)} = 0. \tag{1.62}$$

At a swallowtail singularity, the Jacobian matrix has a rank one like fold and cusp. The lens equation near a swallowtail singularity can again be obtained using the above condition (please see SEF for more details). The corresponding caustic structure is shown in Figure 1.8. From the left panel, one can see that the caustic structure is very sensitive to the values of control parameter p. For $p \leq 0$, the caustic only show a fold line with image multiplicity of 0 and 2. However, as p becomes positive two extra cusps appear and take an overall form of swallowtail (as its name suggests). The corresponding caustic structure divides the local source plane in three different regions with image multiplicity of 0, 2, 4.

1.6.4 Umbilics

The umbilic is given by the condition,

$$\mathbb{A} = 0. \tag{1.63}$$

It means that at an umbilic point both the eigenvalues of the Jacobian matrix are zero,

$$1 - \kappa - \gamma = 0 = 1 - \kappa + \gamma. \tag{1.64}$$

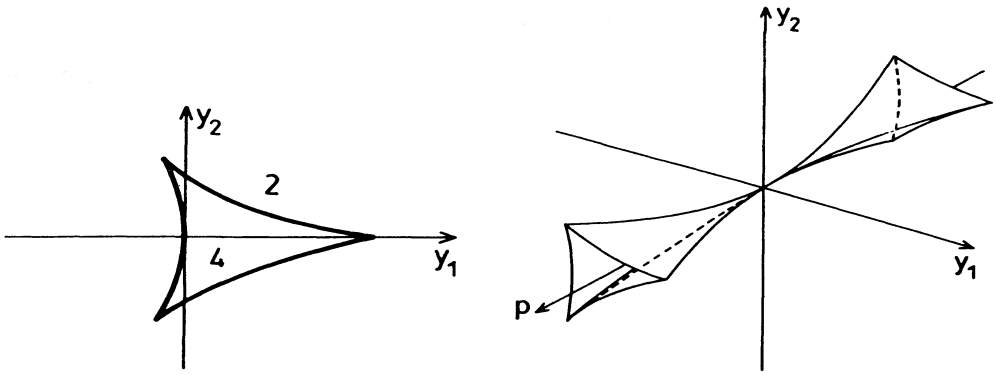

Figure 1.10: Caustic structure near an elliptic umbilic: The left panel represents the caustic structure for one specific value of control parameter p in the source plane. The different numerical values represent the image multiplicity of the source. The right panel shows the large caustic in $(\vec{y}, p)$-space. (Image credit: SEF)

This above condition can only be satisfied if the shear is zero and the convergence is equal to one. Hence, at the umbilic point in the lens plane the projected lens mass density is equal to the critical density defined below Equation (1.37).

Following Equation (1.63) one can see that at an umbilic point, $\mathbb{D}^{(0)} = 0$ and $\nabla\mathbb{D}^{(0)} = 0$. Assuming that the "$\Delta$" represents the determinant of the Hessian matrix of $\mathbb{D}$, one can divide the umbilics in two types:

- $\Delta^{(0)} > 0 :\Rightarrow$ Elliptic umbilic,
- $\Delta^{(0)} < 0 :\Rightarrow$ Hyperbolic umbilic,

where

$$\Delta^{(0)} = \big(6\varphi_{111}\varphi_{112}\varphi_{122}\varphi_{222} - 4\varphi_{111}\varphi_{122}^3 - 4\varphi_{112}^3\varphi_{222} + 3\varphi_{112}^2\varphi_{122}^2 - \varphi_{111}^2\varphi_{222}^2\big)^{(0)}. \quad (1.65)$$

The caustic structures near hyperbolic and elliptic umbilic are shown in Figure 1.9 and 1.10, respectively. We can notice that, unlike swallowtail, there is an exchange of (one/three) cusps between caustics in the source plane at (hyperbolic/elliptic) umbilics such that the total number of cusps in the source plane remains unchanged. The caustic structure near hyperbolic umbilic divides the local source plane in three different regions with image multiplicity of 0, 2, 4. On the other hand, the local source plane near elliptic umbilic is divided in two regions with image multiplicity of 2, 4.

In gravitational lensing with three control parameters, other unstable singularities

like lips and beak-to-beak can also manifest themselves (see SEF). At both of these singularities, two extra cusps appear in the source plane. If we increase the number of control parameters, then we can also observe the manifestation of other higher-order singularities. However, these singularities are not subject to our current analysis.

All of these unstable singularities are related to the cusps in the source plane. Hence, one does not expect to observe them in the circular lenses as they have only one fold caustic and one point caustic in the source plane. The point caustic maps into a circular (tangential) critical curve and the tangent vector to every point on this curve is an eigenvector of the Jacobian with zero eigenvalue. Any perturbation (without rotational symmetry) will turn this point caustic into a diamond-shaped caustic with four cusps. The other important observation from the above analysis is that the number of cusps in the source plane is always even for a transparent lens. It can be seen from the fact that the unstable singularities change the number of cusps in the source plane by 0 or 2, and only lips have the property of creating two cusps from nothing (see SEF).

In this chapter, different singularities are discussed using the Fermat potential. However, these singularities can also be addressed using eigenvalues and eigenvectors of the deformation tensor. This method is used and described in details in the following chapters.

Chapter 2

Finding Singularities in Gravitational Lensing

This chapter is based on:

Meena, A. K., Bagla J. S., "Finding singularities in gravitational lensing", **MNRAS**, 492, 3294 (2021).

2.1 Introduction

Strong gravitational lenses are unique probes of the Universe. By producing multiple images, they provide constraints on the lens mass distribution (Kneib & Natarajan, 2011). The high magnification due to lensing gives us the opportunity to look further into the history of the Universe by observing magnified sources which otherwise would have remained unobserved, (e.g., Atek et al., 2018). In a given lensing system, the observed configuration and magnification of multiple images depends on properties of the lens and the location of the source with respect to the lens. The set of all points in the plane of the lens is called the image plane: here we are working in the small angle approximation. Each point on the image plane can be mapped to a plane at the source redshift, the so-called source plane. For a given lens, and the distance to the source, there is a set of directions where the magnification is formally infinite. The set of points on the image plane representing these directions form the critical curves. As all sources have a finite size, magnification is always finite. The critical curves, mapped to the source plane form the caustics. High magnification images are formed if the source lies on or close to a caustic (Blandford et al., 1989; Schneider et al., 1992).

We have mentioned above that the critical curves and caustics correspond to infinite magnification. This happens because the lens mapping at these points is singular: a finite solid angle element in the image plane gets mapped to a line or a point in the source plane. The structure of the caustic depends on the form of the singularity: singularities of the lensing map can be classified using catastrophe theory (Berry & Upstill, 1980; Gilmore, 2007). The use of catastrophe theory in gravitational lensing was first discussed by Blandford & Narayan (1986) in the case of elliptical lenses. Later this was discussed by Nityananda (1990), Kassiola et al. (1992), SEF and Petters et al. (2001). Independently, classification of singularities in the same map in the context of Zel'dovich approximation was done by Arnold et al. (1982).

One can divide singularities of the lensing map into two types: stable (fold and cusp) and unstable singularities (swallowtail, umbilics). Stable caustics are called so because a small perturbation in the lensing potential leads to a correspondingly small shift in the location of the fold and cusp. On the other hand, the so-called unstable caustics may disappear entirely on the introduction of a small perturbation. In view of this, the focus of most of the studies has been on stable caustics with only a few efforts to improve our understanding of image formation and characteristics of unstable singularities in realistic lens maps (Bagla, 2001; Orban de Xivry & Marshall, 2009) though these caustics have been known and studied theoretically (SEF).

In this work, we propose that unstable caustics can be potentially useful to constrain lens models much more strongly than the stable caustics. The unstable caustics have a stronger variation of magnification around the singular points as compared to stable caustics. Further, if we can predict the location of unstable singularities in the image plane then these regions may be targeted for deep surveys to look for highly magnified sources (Yuan et al., 2012; Zheng et al., 2012; Coe et al., 2013; McLeod et al., 2015; Ebeling et al., 2018). The high magnification comes with a characteristic image formation, and due to the unstable nature of the singularity, the characteristic image formation is visible only for a small range of source redshift. With the upcoming observing facilities like: Euclid: (Laureijs, 2009), James Webb Space Telescope: (JWST, Gardner et al., 2006), Nancy Grace Roman Space Telescope: (WFIRST, Akeson et al., 2019), Vera Rubin Observatory: (LSST, Ivezić et al., 2019), the number of strongly lensed system is expected to increase by more than an order of magnitude. Thus the possibility of observing lensing near unstable singularities is higher and therefore it is timely that we carry out a detailed study. Preliminary results of this study were reported in Bagla (2001). We use algorithms described briefly in that work. We have developed and refined these algorithms further and used them in the case of simple lens models. The algorithms make use of the definitions of singularities, e.g., see (Arnold et al., 1982)

and are similar to those reported in Hidding et al. (2014) for the case of Zel'dovich approximation in two dimensions. These algorithms allow us to locate *all* singularities of the lensing map in the image plane starting from the lensing potential. We then proceed to analyse lens models with one or two major components and study the singularities. We also study variation in singularities in presence of perturbing shear. We illustrate characteristic image formations for each type of unstable singularity. This effort is complementary to an atlas of observed images in exotic lenses (Orban de Xivry & Marshall, 2009) and makes the task of predicting possibility of such image formations much easier.

This chapter is organized as follows. In Section 2.2, we review the classification of singularities and their properties. Section 2.3 contains a description of the algorithm used. Results are given in Section 2.4 for a variety of lenses. Summary and conclusions are presented in Section 2.5. We discuss possibilities for future work in this section.

2.2 Classification of Singularities

In Section 1.6, the stable and unstable singularities are introduced using the Fermat potential. However, here we use the deformation tensor (Equation 1.39) for the same. Here, we redefine the *deformation tensor* as

$$\Psi_{ij} \coloneqq \Psi_{ij}/a, \tag{2.1}$$

where a is the distance ratio D_{ds}/D_s. Redefining the deformation tensor in such a way remove the dependency on the source plane. Then the magnification can be written as

$$\mu = \frac{1}{(1-a\alpha)(1-a\beta)}, \tag{2.2}$$

where α and β are the eigenvalues of the deformation tensor and the magnification goes to infinity if $\alpha = 1/a$ or $\beta = 1/a$ or $\alpha = \beta = 1/a$. Following Equation (2.2), one can see that the critical curves are the eigenvalue contours of the deformation tensor with a value $1/a$. This implies that for a given lens system, the position of critical curves in the image plane can be completely determined by the deformation tensor. The following subsection uses the deformation tensor in terms of its eigenvalues and eigenvectors to classify the different kinds of singularities that can occur in strong gravitational lensing.

2.2.1 A_3-Lines

A_3-lines are the essential elements of the singularity map for a given lens model. In the image plane, these are the lines on which cusps form. As all point singularities are associated with creation, destruction or exchange of cusps, our first goal is to identify the A_3-lines for a lensing potential.

In the image plane A_3-lines pass through the points where the gradient of the eigenvalue of the deformation tensor is orthogonal to the corresponding eigenvector n_λ,

$$n_\lambda . \nabla_x \lambda = 0. \tag{2.3}$$

which implies that at A_3-lines the eigenvector n_λ is tangent to the corresponding eigenvalue contour. The reader may note that this is also true at points where the eigenvalues have extrema, however such points are isolated. At generic points along these lines an infinitesimal portion of the critical curve, which essentially is a contour level for the eigenvalue, is mapped onto itself as we go from the image plane to the source plane.

In case of a spherically symmetric lens, every point on the tangential critical in the lens plane satisfies Equation (2.3) and the corresponding caustic in the source plane is a point caustic. Hence, one cannot use the underlying method for spherically symmetric lenses.

In general, we observe two different sets of A_3-lines in lens plane, one for each eigenvalue of the deformation tensor. The points in the lens plane where A_3-lines and the corresponding eigenvalue contour (with α or $\beta = 1/a$) cross each other correspond to the cusp singularities in source plane at that redshift.

These lines do not intersect each other though as we shall see, lines corresponding to the two eigenvalues can meet at degenerate points ($\alpha = \beta$). The presence of A_3-lines itself proves the stability of cusp singularities in lens mapping: changing the redshift of the source plane merely shifts the cusp to a neighbouring point.

2.2.2 Swallowtail Singularity

The characteristic image formation for a swallowtail singularity is an elongated arc. This *arc* is made up of four images. As we move away from swallowtail singularity the arc changes into multiple images. At a swallowtail singularity, the number of cusps in source plane change by two. In lens plane, swallowtail singularities mark the points

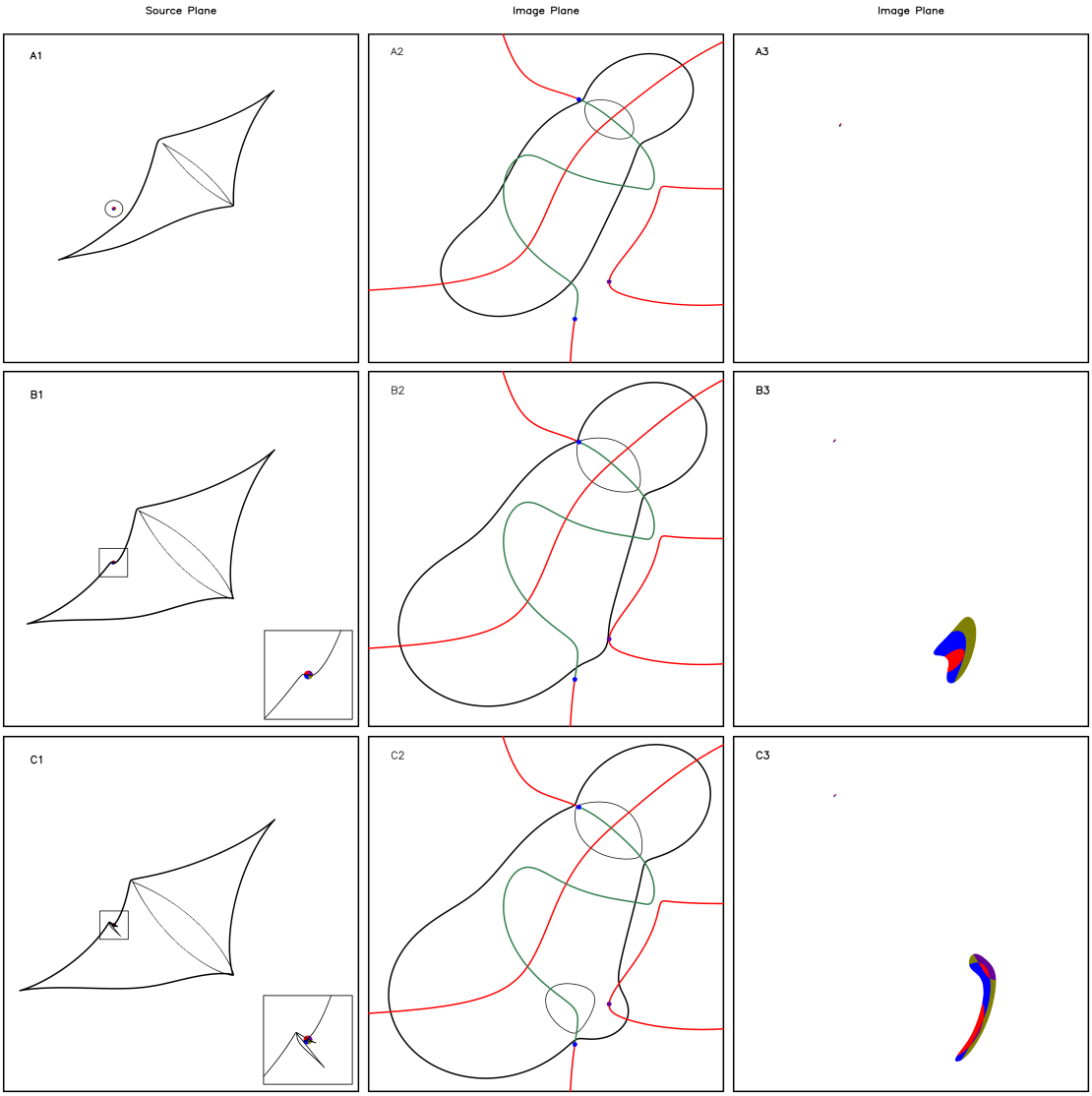

Figure 2.1: Evolution of caustics and critical lines around a swallowtail singularity. The left column (A1, B1, C1) shows the caustics in source plane for three different redshifts including redshift at which swallowtail singularity becomes critical (panel B1). The middle column (A2, B2, C2) shows the corresponding critical lines and the singularity map including A_3-lines (red and dark green lines), swallowtail (violet point), hyperbolic umbilics (blue points). And the right column (A3, B3, C3) shows the image formation.

where eigenvector n_λ of deformation tensor is tangent to the corresponding A_3-line. Which implies that at a swallowtail singularity, the corresponding eigenvalue λ reaches a local maxima along A_3-lines, but this is not a true local maxima. We use this method to identify swallowtail singularity in lens maps.

Figure 2.1 illustrates the caustics and critical curves in source and lens plane around a redshift at which a swallowtail singularity becomes critical. The lens model used here is a two-component softened elliptical isothermal lens. The first column shows the formation of tangential (radial) caustics, denoted by thick (thin) lines, in the source

plane for three different redshifts including redshift z_s, at which the swallowtail singularity becomes critical (panel B1). The second column shows the corresponding critical curves and the singularity map consisting of A_3-lines (red for α and dark green for β eigenvalue) and other singularities in the lens plane. Position of the swallowtail singularity is denoted by a violet point on the A_3-line: this is the point where the A_3 line is tangential to the critical curve. The blue points denote the position of hyperbolic umbilics, discussed in the following subsection. The third column shows the corresponding image formation in lens plane for a given source position in source plane. To see the multiple image formation, we take a circular source: a different color in each quadrant. Such a multi-color source is helpful to recognize positive and negative parity images. The source is shown in the source plane in panels in the left column. A circle is plotted around the source for easy localisation, this circle is not used in the lensing map. The top-left panel (A1) shows the caustics for a redshift smaller than the z_s with a circular source lying outside to both caustics. In the lens plane (top-right panel (A3)), we observe a single distorted image. As the source redshift is set to z_s (panel (B1)), we can see a kink (origin of two extra cusps) in the tangential caustic near the source position. In panel (B1), the centre of the source in source plane lies on this kink. In the corresponding lens plane (B2) at swallowtail singularity three vectors: tangent to the A_3-line, tangent to the eigenvalue contour and the local eigenvector are parallel to each other. The corresponding image formation (B3) shows the formation of a tangential arc made of four images. The magnification factor ($|\mu(r)|$) around a swallowtail singularity is proportional to $r^{-3/4}$, where r is the distance from the singular point. Whereas in the case of fold (cusp), the magnification factor is proportional to the $r^{-1/2}$ ($r^{-2/3}$). Hence, the slope of the magnification factor around the swallowtail singularities is steeper than fold and cusp.

As we further increase the source redshift (C1), the newly formed cusps in source plane move away from each other and the corresponding arc in lens plane (C3) become more stretched. One can see that the arc in the lens plane is made of four images, two of them have positive parity and two of them have negative parity. Due to the finite size of the source, the images shown here are merging into one another. And the image on the upper left corner has positive parity. Eventually, the gradual increment in the source redshift changes the arc into four individual images. Formation of such giant arcs around swallowtail singularities has been already encountered in investigations of strong lens systems (e.g., Abdelsalam et al., 1998; Suyu & Halkola, 2010)

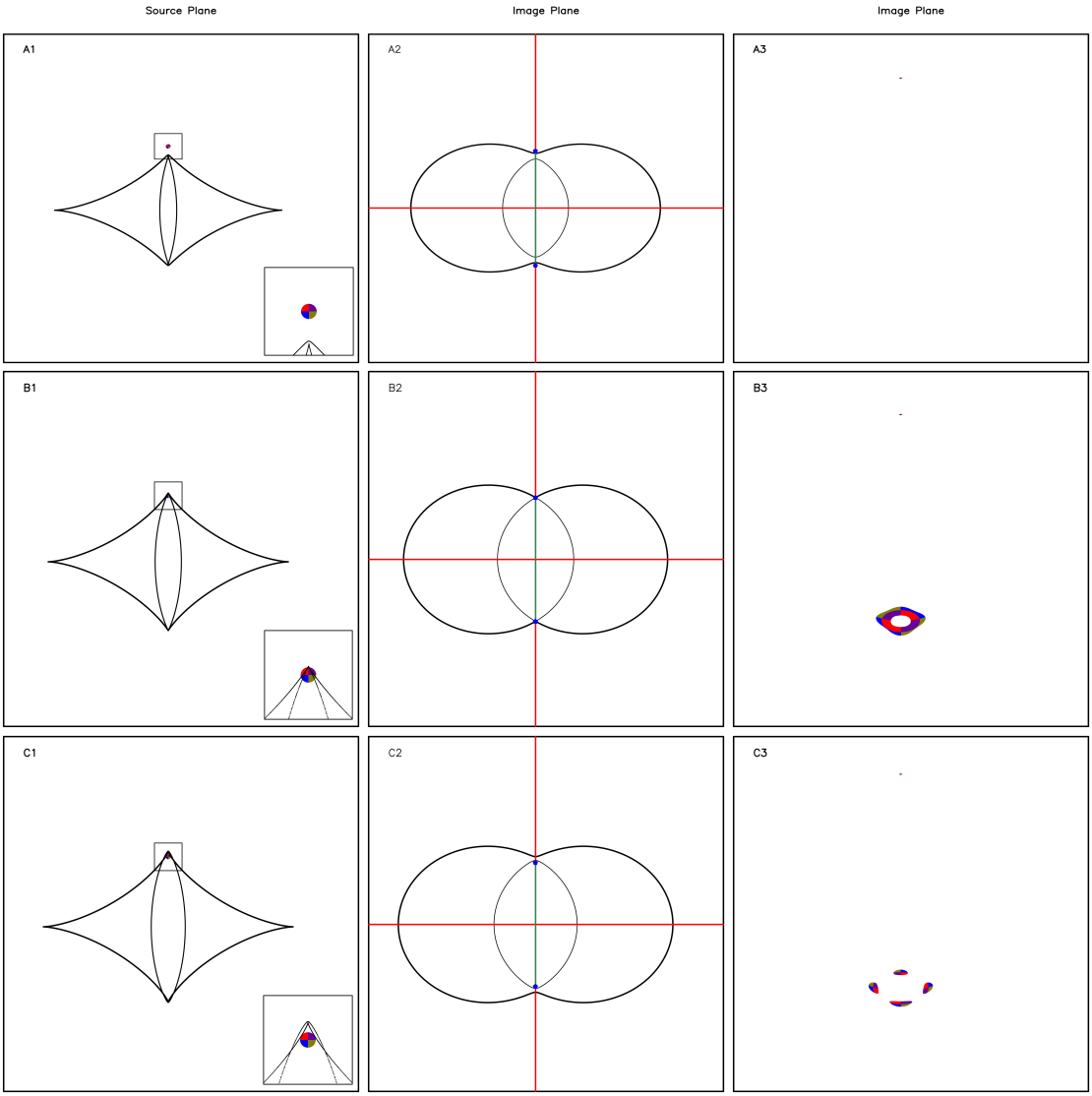

Figure 2.2: Evolution of caustics and critical lines around a hyperbolic umbilic (purse). The left column (A1, B1, C1) shows the caustics in source plane for three different redshifts including redshift at which purse singularity becomes critical (panel B1). The middle column (A2, B2, C2) shows the corresponding critical lines and the singularity map including A_3-lines (red and dark green lines) and purse (blue point). And the right column (A3, B3, C3) shows the image formation. One can notice the exchange of the cusp between radial and tangential caustics (panel B1) and the ring shaped image formation (panel B3) at hyperbolic umbilic. Kindly note that as the umbilics are symmetric, the image formation about either one will be the same apart from a reflection. Here, we show images corresponding to one of the umbilics, as marked by the source position in the left column.

2.2.3 Umbilics

For a given lens model, the presence of umbilics in the corresponding singularity map denote the points with zero shear (γ) in lens plane. At these points, both of the eigenvalues of the deformation tensor are equal to each other ($\alpha = \beta$). The dependence

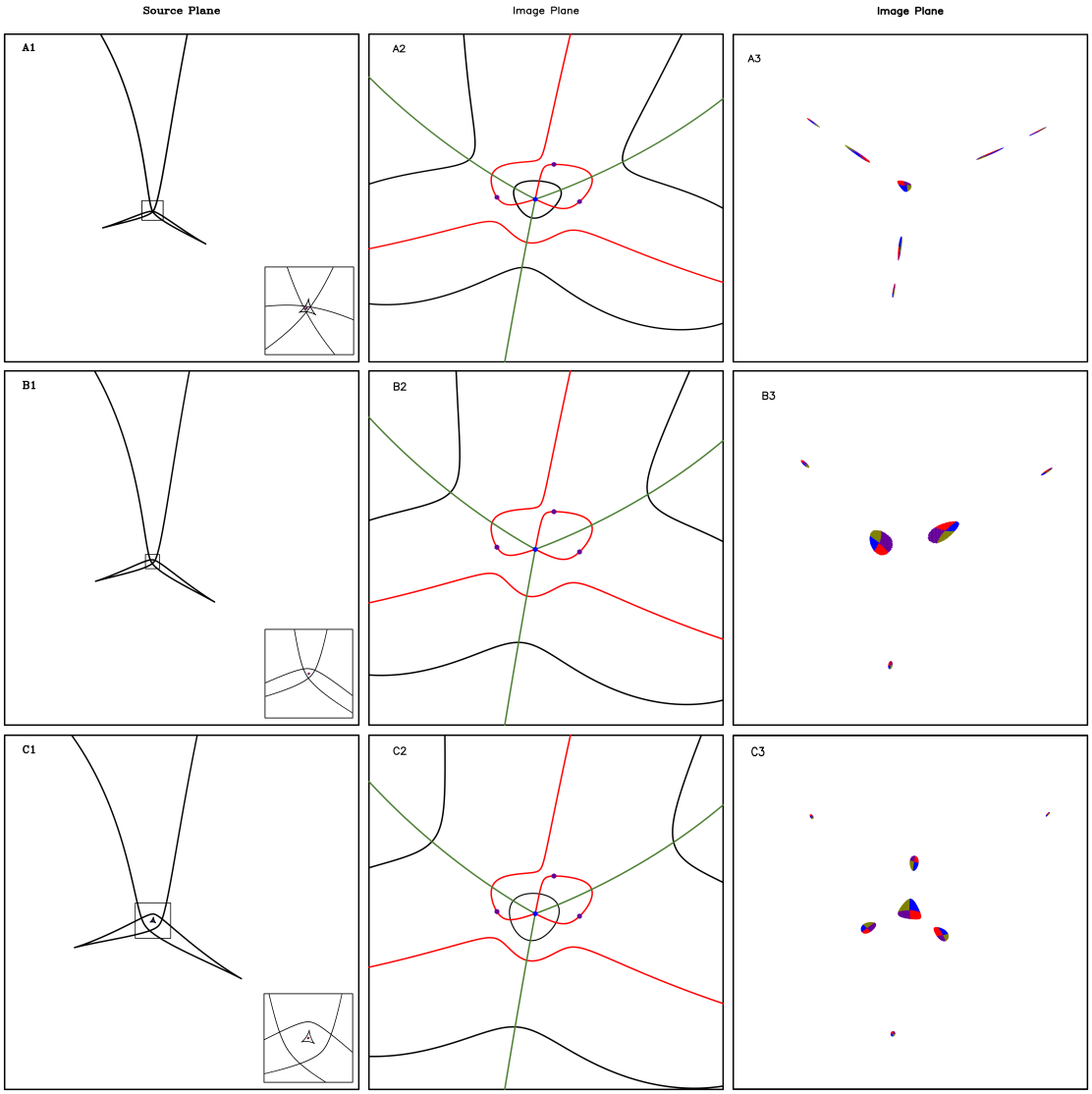

Figure 2.3: Evolution of caustics and critical lines near an elliptic umbilic (denoted by blue point in singularity map). At elliptic umbilic, the triangular shaped caustic corresponding to the tangential caustic (panel A1) goes to a point caustic (panel B1) and emerges as a triangular shaped caustic corresponding to the radial caustic (panel C1). The corresponding image formation shows a Y-shaped seven image configuration.

on both eigenvalues simultaneously separates these singularities from the A_3-lines and swallowtail singularities, which have dependency on one eigenvalue in their definitions. The equality of both eigenvalues implies that at umbilics, eigenvectors of the deformation tensor are degenerate. As a result, any vector at these points can behave as an eigenvector. We can always choose the eigenvector in such a way that A_3-line condition is always satisfied (for a quantitative analysis see Hidding et al. 2014). At these points A_3-lines corresponding to different eigenvalues meet with each other. There are two types of umbilics present in gravitational lens mapping: elliptic and hyperbolic

umbilics. This division of the umbilics depends on the sign of the quantity s_D,

$$s_D \equiv t_{111}^2 t_{222}^2 - 3t_{112}^2 t_{122}^2 - 6t_{111}t_{112}t_{122}t_{222} + 4t_{111}t_{122}^3 + 4t_{222}t_{112}^3 \,, \tag{2.4}$$

where $t_{ijk} = \frac{\Psi_{ij}}{\partial x_k}$. If s_D is positive, the singularity is called hyperbolic umbilic and if it is negative then the singularity is elliptic umbilic. At umbilics, the number of cusps in the source plane remains unchanged but there is an exchange of one or three cusps between tangential and radial caustics depending on the type of the umbilic. In case of a hyperbolic umbilic, one cusp is exchanged between the tangential and the radial caustic: in the image plane an A_3-line corresponding to each of the two eigenvalues meet at this point. Whereas three A_3-lines of each of the two eigenvalues meet at the elliptic umbilic in the image plane, and three cusps are exchanged between the tangential and the radial caustic in the source plane.

In order to discuss the evolution of the caustics and critical curves near a hyperbolic umbilic (because of the simplicity of its singularity map), we use a one-component elliptical lens. The evolution of caustics and critical curves near a hyperbolic umbilic is shown in Figure 2.2. The A_3-lines in the singularity map (middle column) are denoted by red and dark green lines for two different eigenvalues. The positions of hyperbolic umbilic in lens plane are denoted by blue points, at which two A_3-lines (one for α and one for β eigenvalue) meet with each other. For a redshift smaller than the redshift at which hyperbolic umbilic becomes critical, z_u both (radial and tangential) caustics in source plane each have two cusps (A1). As we increase the source redshift to z_u, there is an exchange of cusp from radial caustic to tangential caustic (panel B1) (For the single component elliptical lens model, because of the symmetry of the lens model, both of the hyperbolic umbilics become critical at the same redshift. The symmetry is broken in presence of a second component or shear.). The corresponding image formation (panel B3) shows a single demagnified image with positive parity and a loop formed by four images, two of them with positive parity and two of them with negative parity. As we increase the source redshift further, source plane has a diamond shaped tangential caustic and a smooth radial caustic (panel C1) and in lens plane the highly magnified ring shaped image changes into four individual less magnified images (panel C3). The ring and the cross (for higher redshifts) is not centered at the lens centre but is off centre. We have studied the location of the ring by varying the mass profile of the lens and we find that the ring is located where the projected surface density begins to drop sharply. The magnification factor $|\mu|$ falls as r^{-1} around both umbilics as one moves away from the singular point. Thus magnification factor falls much more rapidly around umbilics than other singularities. So far only one lens system (Abell 1703) with image formation

near a hyperbolic umbilic has been seen (Zitrin et al., 2010).

Unlike the hyperbolic umbilic, at elliptic umbilic, there are six A_3-lines (three each for each of the two eigenvalues of the deformation tensor) meet with each other. For an illustration, formation of an elliptic umbilic in case of a two-component elliptical lens model is shown in the Figure 2.3. We find that often, two of three A_3-lines of one or both eigenvalues form a small closed loop. This can be seen in examples shown in Figure 2.4. In panel (A1), we only see tangential caustics, and the source lies inside the triangular shaped caustic. Panel (A3) shows the characteristic image formation (seven images in a shape of Y) near an elliptic umbilic. The central image has positive parity. The next three images from the central image have negative parity. And the three outer images again have positive parity. As we increase the source redshift, the size of the triangular shaped caustic decrease and at the same time, it moves away from the source position. At a redshift z_p, where elliptic umbilic becomes critical, it becomes a points caustic (panel B1), and the source lies close to this point caustic. The corresponding images still form a Y-shaped structure in lens plane but with only five images. As we further increase the source redshift, the point caustic turns into a triangular shaped radial caustic (panel C3). Which implies that at elliptic umbilic, there is an exchange of three cusps between tangential and radial caustics. In panel (C1), we moved the source inside the triangular caustic to see whether it still gives a Y-shaped image formation. We get a different kind of image formation with central image rotated by π.

Figure 2.3, shows the singularity map close to the elliptic umbilic (shown by blue point). Swallowtail singularities are shown as violet points. The complete singularity map for Figure 2.3 is given in Figure 2.4 (panel A5). The characteristic image form is six images radiating out from the singularity. The singularity need not coincide with the centre of the lens, The images do not have any tangential deformation.

2.3 Algorithm

In this section, we briefly discuss the algorithm used to find out the singularities for a given lens model. We set up a uniform grid in the lens plane for calculations of physical quantities in order to locate the singularities. The grid-size depends on the resolution required for the lens model. In general we require adequate resolution as we are dealing with non-linear combinations of second derivatives of the lensing potential, even the smallest features should be well resolved on the grid. We use finite difference methods to compute derivatives on the grid. To calculate the position of the umbilics in the lens plane, we use the fact that at umbilics, both components of the shear tensor vanish,

identically. Our approach closely follows that of Hidding et al. (2014). The flow of the code is as follows:

- INPUT (Lens Potential)
- CALCULATE first and second derivatives of the potential
- CALCULATE eigenvalue and eigenvectors of the deformation tensor
- CALCULATE gradient of eigenvalue
- CALUCLATE extrema
  - CALCULATE local maxima
  - CALCULATE local minima
- Identify points on A_3-lines
- Identify A_4 -points using the algorithm given subsection 2.2.2
- Identify D_4 -points using the algorithm given subsection 2.2.3

The potential of the given lens model is the input in this algorithm. The potential can be computed from a mass model, or be provided directly. Given the potential, the deformation tensor is computed at each point followed by calculation of its eigenvalues and corresponding eigenvectors. This information along with gradient of eigenvalues is sufficient to identify points on the A_3 -lines. Note that points on the A_3 -lines can be identified on the mesh and need not coincide with the grid points. The points need to be ordered to construct curves: this is required for identifying A_4 points as we need to locate maxima of eigenvalue along the A_3-lines.

We find that it is simpler to identify umbilics by realizing that the diagonal components of the deformation tensor are equal, and the off-diagonal component of the deformation tensor (shear) vanishes. Each of these conditions specifies curves in the image plane, and intersections of these curves give us umbilics. We can classify the type of umbilics by counting the number of A_3-lines that converge at this point.

2.4 Results

We validate our algorithm by applying it to a single component lens where the potential can be expressed in a closed form and the image structure has been studied in detail.

Then, we apply it to multi-component lenses and study a variety of configurations. Lastly, we apply it to one real lens model. As mentioned above, this technique does not work in case of isolated spherically symmetric lenses because of the absence of cusp formation. We study elliptical lenses with one and two components. In the case of one-component elliptical lens, there are two A_3-lines and two hyperbolic umbilics. Whereas for two-component lens, the location of A_3-lines and other singularities in lens plane depend on the lens configuration.

We also discuss the behaviour of swallowtail and umbilics in a lens model under external perturbations in case of one and two component elliptical lenses. This gives us the estimate about the amount of external shear under which a singularity does not vanish from the lens plane and hence gives us an idea about how robust these point singularities really are. In the following subsections, we will discuss the singularity maps for elliptical lenses and Abell 697 in detail. After that, we study the stability of these different singularities in lens mapping.

2.4.1 One-Component Elliptical Lens

We first consider a one-component elliptical lens. This is a good model for an isolated lens that is dynamically relaxed, e.g., an isolated galaxy or a cluster of galaxies. The elliptical isothermal lens with a finite core has a potential of the form:

$$\Psi(x_1,x_2) = \Psi_0 \sqrt{r_0^2 + (1-\varepsilon)\,(x_1 - x_{01})^2 + (1+\varepsilon)\,(x_2 - x_{02})^2}, \tag{2.5}$$

where r_0 is the core radius of the lens, ε is the ellipticity, (x_{01}, x_{02}) are the coordinates of the centre of the lens with respect to the optical axis and ψ_0 describes the strength of the lens.

The characteristics of this lens are described in detail in Blandford & Narayan (1986, see Fig 10). The singularity map in lens plane for this lens model is shown in Figure 2.2 (middle column (A2,B2,C2)). It has two A_3-lines (represented in red and dark green) for two eigenvalues of the deformation tensor, running along the major and the minor axis of the lens potential. This lens model also has two hyperbolic umbilics along the minor axis and their position depends on the lens parameters, primarily on the core radius r_0. Because of the elliptical symmetry in the lens model, both umbilics lie at the same distance from the centre of the lens. As a result, both umbilics become critical at the same source redshift. If we change the core radius, this distance from the centre and the redshift at which these hyperbolic umbilics becomes critical, also change.

2.4.2 Two-Component Elliptical Lens

Most realistic lenses have several components, though one of the components may dominate over the others. In this section, we consider two-component lenses. We consider one primary (dominant) and one secondary component. The presence of secondary lens significantly affects the lensing due to primary lens. In order to include the effects of the secondary lens, one has to modify the lensing potential in Equation (2.2). If the secondary lens is also an elliptical lens (for simplicity), then the lens potential becomes:

$$\psi(x_1,x_2) = \Psi_p + \Psi_s, \tag{2.6}$$

with Ψ_p and Ψ_s are one-component elliptical lenses centered at different points in the image plane with different core radii and ellipticities and the major axes of the two components can be at an angle. r_{01} (r_{02}) are the corresponding core radii for the two potentials, ε_1 (ε_2) is the ellipticity and (x_{11},x_{12}) $((x_{21},x_{22}))$ are the coordinates of the centre of the primary (secondary) lens with respect to the optical axis.

Different sets of lens parameters give different kinds of singularity map and image formation. For example, Figure 2.1 and Figure 2.3 represent singularity map for two-component lens models with two different sets of lens parameters. Figure 2.4 shows some other possible singularity maps for two-component elliptical lens with a fixed primary lens and different (randomly picked) position and orientation of the secondary lens. As before, red and dark green lines represent the A_3-lines with swallowtail and umbilic points denoted by violet and blue points, respectively. One can see the dependency of unstable singularities on lens parameters: as we change the secondary lens, the position and critical redshift for the unstable singularities also change. From Figure 2.4, we also gain some knowledge about the sensitivity of the unstable singularities to the lens parameters. All panels in Figure 2.4 have hyperbolic umbilics and swallowtail (except first panel), whereas only three panels show elliptic umbilic. We infer that elliptic umbilics are more sensitive to the lens parameters than the swallowtail and the hyperbolic umbilic.

2.4.3 Stability

In general, finding an isolated gravitational lens with one or two components is highly unlikely. Real gravitational lenses reside in an environment made of several structures. These external local structure perturb the lensing potential, by introducing (constant) external convergence (κ_{ext}) and shear (γ_{ext}). As a result, the perturbed lensing potential

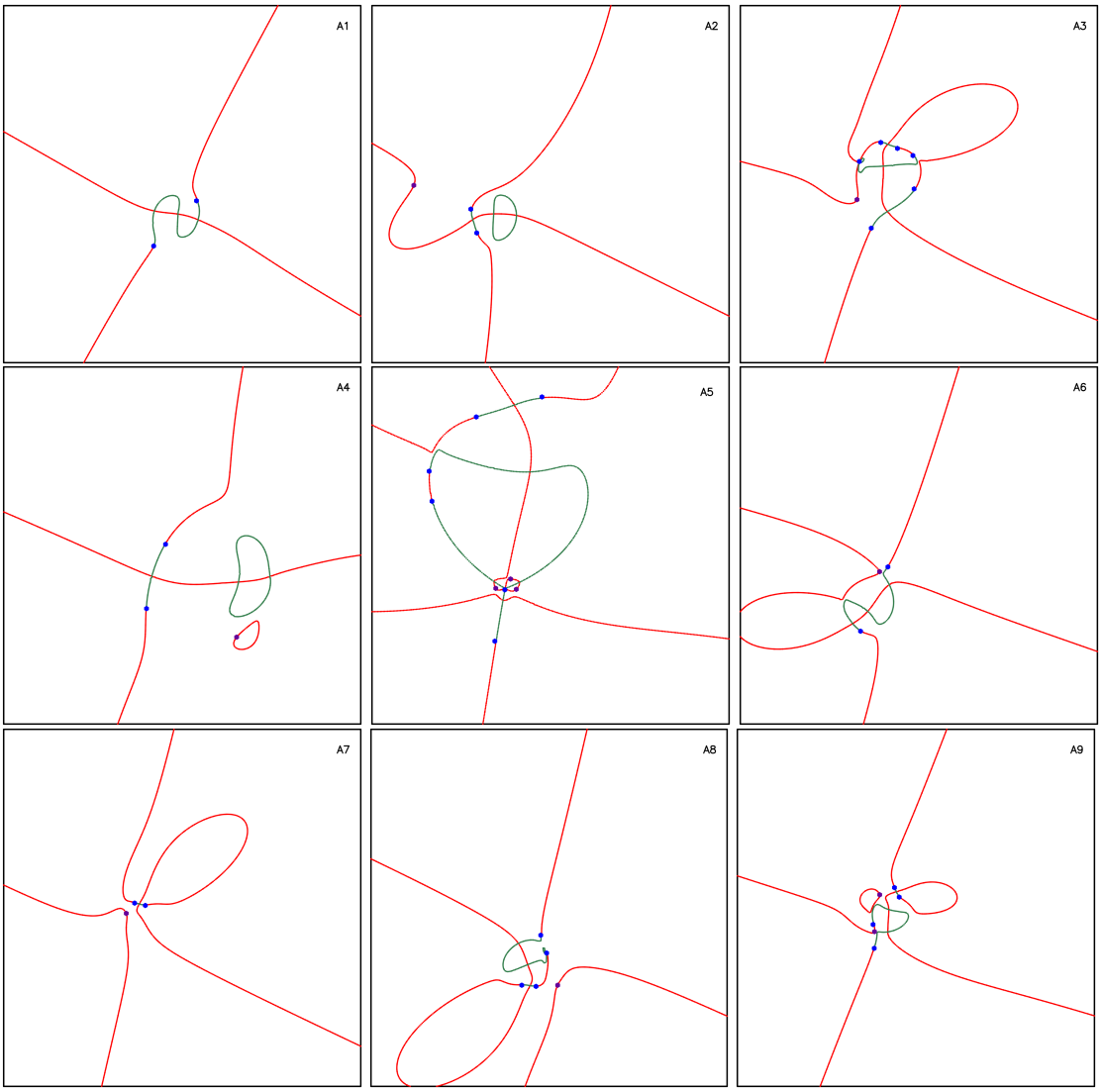

Figure 2.4: Singularity maps for different positions and orientations of the secondary lens in case of two-component elliptical lens with a fixed position and orientation of primary lens. The red and dark green lines are the A_3-lines with swallowtail and umbilics denoted by violet and blue points, respectively. The position and number of unstable singularities change with the change in lens parameters. Which shows the strong dependency of singularity map on the lens parameters.

is given by,

$$\Psi(x_1,x_2) = \Psi_p + \frac{\kappa_{ext}}{2}\left(x_1^2+x_2^2\right) + \frac{\gamma_1'}{2}\left(x_1^2-x_2^2\right) + \gamma_2' x_1 x_2, \tag{2.7}$$

where Ψ_p is the potential of primary lens, given by Equation (2.5) or (2.6) in case of elliptical lenses or given by some other profile and (γ_1', γ_2') denotes the component of external shear (γ_{ext}).

The effect of the external convergence (κ_{ext}) is equivalent to the addition of a constant mass sheet in the lens model, which simply changes the total strength of the pri-

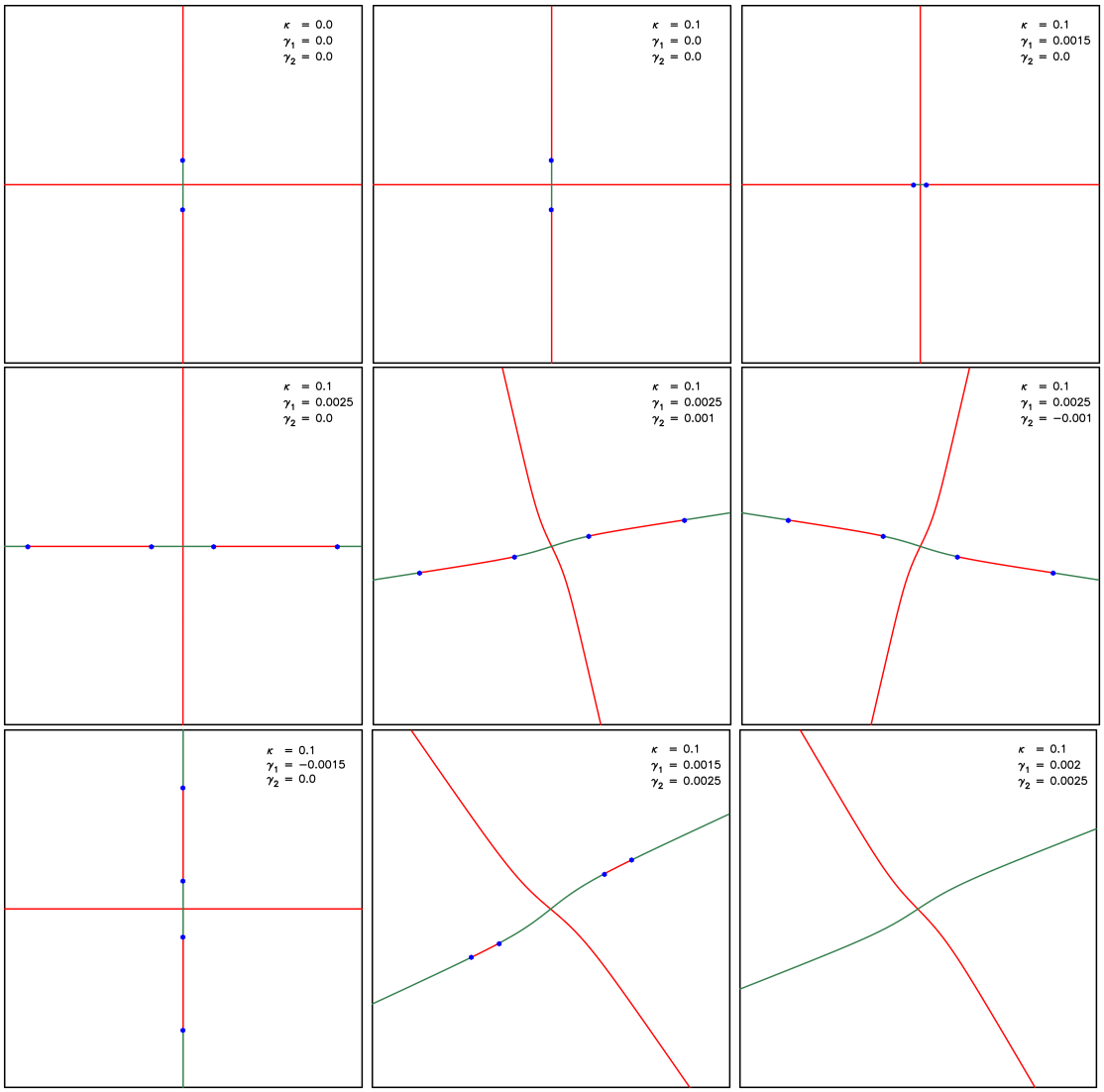

Figure 2.5: Effect of external convergence and shear on singularity map in case of a one-component elliptical lens. One can see the motion of extra pair of umbilics towards the already existing pair of umbilics. After a certain amount of external shear all point singularities disappear from the singularity map (bottom-right panel).

mary lens. As a result, the critical redshift for unstable singularities changes, but neither the unstable singularities vanish nor the location of A_3-lines in lens plane changes due to the presence of external convergence. On the other hand, the presence of external shear (γ_{ext}) shifts the location of A_3-lines significantly and as a result, it changes the singularity map for a given lens model. The presence of external shear can also introduce or remove point singularities. The effect of external shear with a fixed value of external convergence in case of a one-component elliptical lens model, Equation (2.5) is shown in Figure 2.5. One can see that, for non-zero external shear, two extra hyperbolic umbilics occur in the lens plane along the major or minor axis depending on the values of shear components. As we increase the amount of external shear, this extra pair of umbilics move towards already existing umbilics and merge with them. This implies

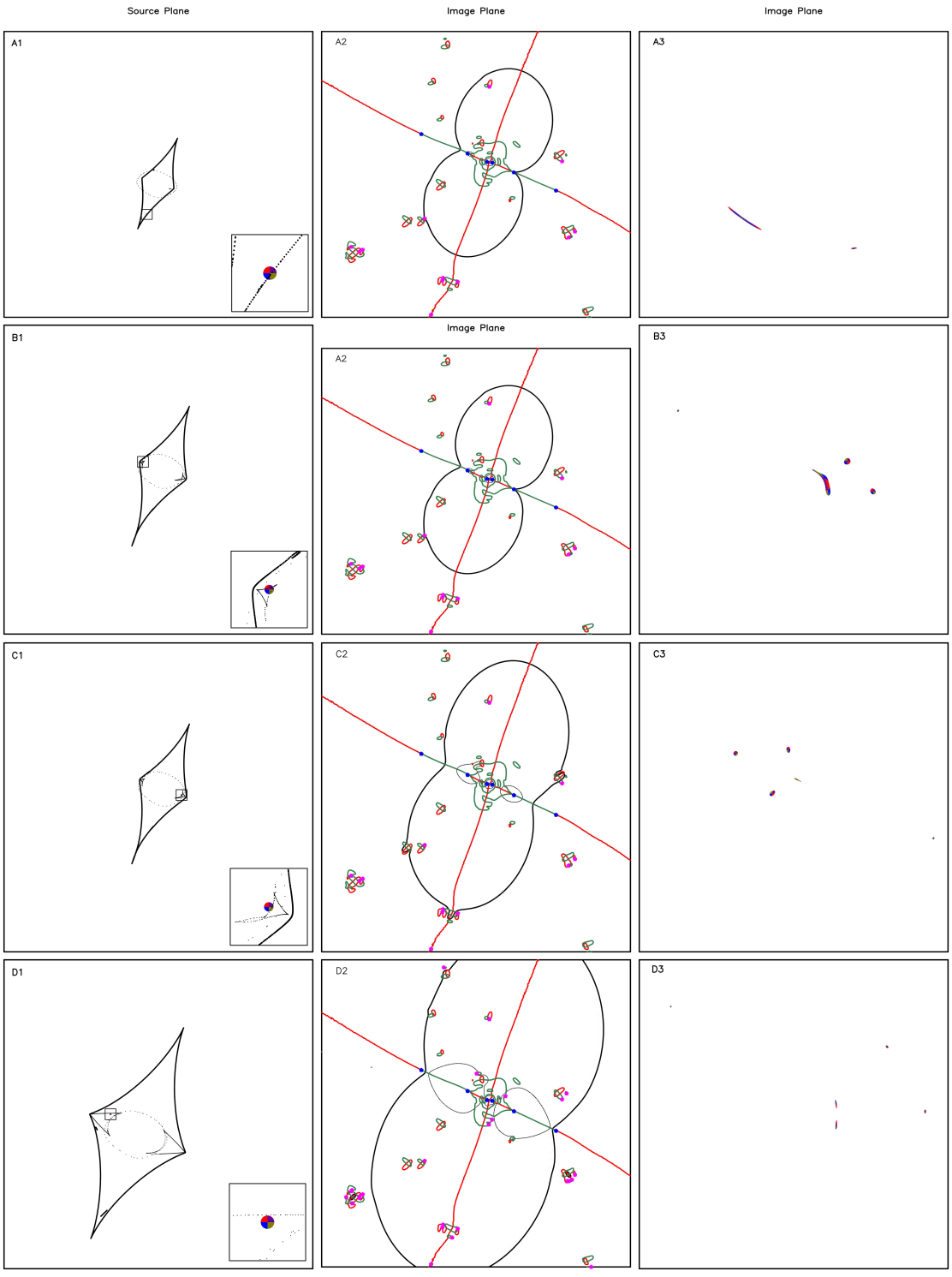

Figure 2.6: Image formation and singularity map for Abell 697: The left panel shows caustics, the middle column shows critical curves in the image plane and the right column shows the lensed images. The top panel represents image formation near a swallowtail singularity at source redshift $z_s = 0.67$. The two middle panels represent image formation for a source at $z_s = 0.82$ and the bottom panel represents image formation for a source at redshift $z_s = 2.0$.

that introducing a finite amount of external shear can also remove the already existing point singularities from the singularity map and it is possible (in highly symmetric case) to have a singularity map without any point singularities. The amount of external shear $\gamma_{ext} = \left(\sqrt{\gamma_1'^2 + \gamma_2'^2}\right)$, under which point singularities shift but remain in the lens plane depends on the type of the singularity. In case of hyperbolic umbilic, it is of the order of 10^{-3}. Similarly, the amount of external shear for which a swallowtail (elliptic umbilic) shifts but survives in the lens plane is of the order of 10^{-4} $\left(10^{-5}\right)$. But for some particular directions of external shear, the swallowtail and elliptic umbilics show extra stability, i.e., the magnitude of external shear under which these singularities remain in the lens plane attain a higher value than the other cases. This reinforces the impression from the qualitative study in the last subsection that the elliptic umbilic is less stable as compared to the hyperbolic umbilic and swallowtail.

2.4.4 Abell 697

After testing our approach with simple model lenses, we apply the algorithm to a real lens to illustrate the utility and efficacy of our approach. We work with the cluster lens Abell 697 ($z = 0.282$). We use the data for the lens from RELICS (Cibirka et al., 2018; Coe et al., 2019). The reason for choosing the Abell 697 for the preliminary analysis is the relative simplicity of the critical lines in the lens plane. The study of more complicated lenses is under consideration, and the results for a large set of clusters will be presented in the forthcoming Chapter along with a statistical analysis of occurrence of point singularities. Figure 2.6 shows the singularity map along with the critical lines and caustics in image and source plane for Abell 697. Here we only considered the central region of Abell 697 with size 440×440pixels (1 pixel =$0.06''$) (Cibirka et al., 2018). We can see that the dominant component here is like an elliptical lens and there is a lot of small-scale structure contributed by other components in the lens. The role of other components is to increase the length of A_3-lines and also to introduce point singularities.

The top panel in Figure 2.6 shows the image formation near a swallowtail singularity for a source at redshift $z_s = 0.67$. The second and third panel shows the image formation for a source at redshift $z_s = 0.82$ for two different source positions. The bottom panel shows the image formation for a source at redshift $z_s = 2.0$. Here the source position is chosen in such a way so that it can reproduce the image formation for system 1 in Cibirka et al. (2018). One can see that we were able to reproduce the four images for system 1 along with the fifth image, which was not observed due to the contamination from BCG, as mentioned in Cibirka et al. (2018). Since we considered a circular source,

the shape of the images can be different from Cibirka et al. (2018). As one can see from the bottom panel, one pair of hyperbolic umbilic is still outside the critical curves. This means that the critical redshift for this pair is higher than the 1.1. Locations of these singularities are optimal sites for searching for faint sources at high redshifts.

2.5 Conclusions

In this work, we have analyzed stable and unstable singularities that can occur in strong gravitational lensing. In order to locate these singularities, we have implemented algorithms which take lens potential as an input. We have applied our algorithm in the case of simple lens models as well as a real lens. Singularity map, which comprises all these singularities provides a compact representation of the given lens model in the lens plane. The presence of these unstable singularities in the singularity map can be used to constrain the lens model if we can find a lensed source in the vicinity. Magnification is very large in the vicinity of these singularities and each of these singularities has a characteristic image formation that can be used to identify the singularities. Multiple images in these characteristic image formations lie in a very compact region (of the order of a few arcsec around the singular point) of the lens plane. Further, the regions with A_3 -lines and point singularities are obvious targets for deep surveys that use gravitational lenses to search for very faint sources at high redshifts.

The singularities can be identified using the characteristic image forms. In the case of A_4 points (swallowtail), we get four images in a straight line: the images form an arc with a radius of curvature much larger than the distance from the cluster centre. Abell 370 has an image system of this type. The hyperbolic umbilic (purse) has an image formation of a ring or a cross centered away from the centre of the lens. Further, in this case the radius of curvature of the ring is much smaller than the characteristic radius of the lens system. Such an image system has been seen in Abell 1703 (Orban de Xivry & Marshall, 2009). The elliptic umbilic (pyramid) has images radiating out from a centre, these do not show any tangential distortion. The centre of the image system need not coincide with the centre of the lens system. To the best of our knowledge such an image system has not been seen so far.

We have studied the dependency of unstable singularities on lens parameters as well as on the external shear. The magnitude of external shear under which these singularities remain in the singularity map is different for different singularities. This is of the order of 10^{-3}, 10^{-4}, and 10^{-5} in case of hyperbolic umbilic, swallowtail, and elliptic umbilic, respectively. Thus the elliptic umbilic is most sensitive to perturbations in

lensing potential and hence is the most unstable.

The somewhat unstable nature of such singularities can be put to good use in two ways: finding characteristic image formations can be used to constrain lens models, and, with multiple constraints on the lens model we can potentially invert the problem and constrain redshifts of sources to better than what can be achieved with photometric redshifts. Multiple images for a single source also open up the exciting possibility of measuring time delays between each pair. Multiple measurements of pairwise time delay can provide very significant constraints on the lens model and the scale of the Universe. Such measurements can potentially be made even if the images are not resolved (Borra, 2008).

We have applied our approach in case the of simple lens models and one real lens: Abell 697. We are studying other lens systems using our approach and an atlas of lens singularities and their statistical analysis will be presented in a forthcoming paper. Such an atlas can be of use for refinement of lens models with further observations and also for targeting specific regions in searches for very faint sources at high redshifts. Along with an atlas of lens models, we also propose to construct an atlas of variations around the characteristic image forms. Such an atlas of image forms can be used for training machine learning programs (e.g., Davies et al., 2019). However, for a complete analysis of the lens system, one requires detailed modeling of the gravitational lens.

Chapter 3

Exotic Image Formation in Cluster Lenses – I: Cross-Section

This chapter is based on:

Meena, A. K., Bagla J. S., "Exotic Image Formation in Strong Gravitational Lensing by Clusters of Galaxies – I: Cross-Section", **MNRAS**, 503, 2097 (2021).

3.1 Introduction

In this work, we locate the highly magnified regions in the lens plane, for all source redshifts, for 10 different cluster lens systems from the Hubble Frontier Fields Survey (HFF) and the Reionization Lensing Cluster Survey (RELICS). The algorithm to do this has been discussed briefly in Bagla (2001) and presented in detail in Meena & Bagla (2020b). As discussed in Chapter 2, a singularity map consisting of A_3-lines and unstable (point) singularities is ideal for our study. These point singularities (swallowtail, hyperbolic umbilic, elliptic umbilic) are formed only for some specific source redshifts and specific source positions in the source plane. Apart from that, every point singularity comes with a characteristic image formation. A_3-lines correspond to cusp in the source plane and these are present over a wide range of source redshifts. As cusps are stable singularities, these are continuous lines instead of points in the singularity map, with points corresponding to different source redshifts. The image formation corresponding to structures (A_3-lines and point singularities) in singularity maps (for the appropriate source redshift) shows three or more highly magnified images lying near each other in a small region of the lens plane in the vicinity of the singularity. The sin-

gularity maps corresponding to cluster lenses not only point out the highly magnified regions in the lens plane but are also sensitive to the lens mass reconstruction techniques. Here, we also compare different mass models corresponding to each cluster lens. These mass models are reconstructed using different (parametric and non-parametric) methods. The comparison has been done to see how sensitive the A_3-line structure and the total number of point singularities is to the cluster mass reconstruction method as different approaches use different sets of underlying assumptions.

Apart from locating the highly magnified regions in the lens plane and looking at the effect of mass reconstruction methods on the singularity map, the other important point that has been discussed (Orban de Xivry & Marshall, 2009) is to estimate the expected number of source galaxies lying near the point singularities. This allows us to estimate the probability of observing these characteristic image formations in the upcoming large-scale surveys. In order to do so, we require the distribution of galaxies as a function of redshift. This can be determined from the galaxy luminosity function (GLF) and the Schechter function (Schechter, 1976) is widely used to parametrize it. Various studies using different surveys have been carried out to determine the rest frame GLF as a function of the redshift in different wavelength bands (UV:Ono et al. (2018); Bowler et al. (2020); Moutard et al. (2020), IR: Cirasuolo et al. (2007, 2010); Mortlock et al. (2017)). Different groups have estimated the number of galaxies that may be observed with JWST considering different models of galaxy formation and evolution (Cowley et al., 2018; Williams et al., 2018a; Yung et al., 2019). Following Cowley et al. (2018), we estimate the number of exotic images that may be observed with JWST in one of the NIRCam bands.

This Chapter is organized as follows. The cluster lenses used in the present analysis are enumerated in Section 3.2. The results are presented in Section 3.3. The construction of singularity maps for different cluster lenses is discussed in Section 3.3.1. Discussion of stability of singularity maps is presented in Section 3.3.2. In Section 3.3.3, we estimate the number of strongly lensed galaxy sources with characteristic image formations near these point singularities that can be observed with the JWST. In Section 3.3.4, we discuss the possibility of constraining the source redshift using point singularities. Summary and conclusions are presented in Section 3.4. We also discuss the future work in this section.

Table 3.1: Cluster lenses used in current analysis: The upper half of the table lists the cluster lenses taken from the *Hubble Frontier fields (HFF)* survey, whereas the lower part of the table has details of the cluster lenses from the *Reionization Lensing Cluster Survey (RELICS)*. For the HFF clusters, four different mass models provided by Keeton, Sharon, Williams, and Zitrin (zitrin_nfw) groups are used. For the RELICS clusters, we only use one mass model for each cluster provided by Zitrin group (zitrin_ltm_gauss). The version and the resolution of these mass models is listed below.

HFF Clusters				
	Keeton	Sharon	Williams	Zitrin
Abell 370 (A370)	v4(0.06″)	v4(0.05″)	v4(0.05″)	v1(0.050″)
Abell 2744 (A2744)	v4(0.06″)	v4(0.05″)	v4(0.05″)	v3(0.060″)
Abell S1063 (AS1063)	v4(0.06″)	v4(0.05″)	v4(0.05″)	v1(0.065″)
MACS J0416.1-2403 (MACS0416)	v4(0.06″)	v4(0.05″)	v4(0.05″)	v3(0.060″)
MACS J1149.5+2223 (MACS1149)	v4(0.06″)	v4(0.05″)	v4(0.05″)	
RELICS Clusters				
	Zitrin			
MACS J0159.8-0849 (MACS0159)	v1(0.06″)			
MACS J0308.9+2645 (MACS0308)	v1(0.06″)			
PLCK G171.9-40.7 (PLCKG171	v1(0.06″)			
PLCK G287.0+32.9 (PLCKG287)	v1(0.06″)			
SPT-CLJ0615-5746 (SPT0615)	v1(0.06″)			

3.2 Cluster lenses

In this section, we briefly discuss the cluster lenses used to construct and study the singularity maps. Preliminary analysis in this direction consisting of ideal lens models and one real cluster lens, Abell 697, has been presented in 2. In the present analysis, we selected ten clusters for a detailed study of their singularity maps. Five out of these ten clusters were chosen from the *Hubble Frontier Fields (HFF) survey* (Lotz et al., 2017) [1] and the other five were chosen from the *Reionization Lensing Cluster Survey (RELICS)* (Coe et al., 2019) [2]. The cluster lenses used in current study are described in Table 3.1. The table provides relevant details, e.g,, the resolution and the version of the mass models corresponding to various groups of modelers.

The HFF program targets a total of six massive merging clusters to study the distant, faint sources and the cluster dynamics (please see Lotz et al. (2017) for further details). Our analysis requires a model for the gravitational lenses. Mass reconstruction of the clusters has been attempted by multiple groups (Diego et al., 2005; Merten et al., 2011; Jauzac et al., 2014; Johnson et al., 2014; McCully et al., 2014; Grillo et al., 2015; Ishigaki et al., 2015; Hoag et al., 2016; Caminha et al., 2017; Kawamata et al., 2018)

[1] https://archive.stsci.edu/prepds/frontier/
[2] https://archive.stsci.edu/prepds/relics/

using different approaches. The data from the observations is finite, one cannot model these cluster lenses with arbitrary precision and resolution. Different groups use different methods to reconstruct the cluster lens mass distribution; for example, some groups use parametric modeling (including the light distribution of cluster galaxies, some preferred profile for the mass of cluster substructures) whereas some other groups use the non-parametric approach which does not rely on any assumption. Some groups also use hybrid methods which take inputs from both parametric and non-parametric approaches (please see Priewe et al. (2017); Meneghetti et al. (2017) for a comparison of different modeling techniques). In our work, for five different HFF clusters, we used best-fit lens mass models provided by four different teams: Keeton, Sharon (Jullo et al., 2007; Johnson et al., 2014), Williams (Liesenborgs et al., 2007) and Zitrin (Zitrin et al., 2009, 2013) (in the case of Zitrin group, we used mass models reconstructed using NFW profile, i.e., zitrin_nfw) to construct the singularity maps for an HFF cluster. We chose the central region of every cluster for our analysis, as these regions are responsible for the strong lensing. The size of the central part which we chose depends on the resolution of the lens model. In our analysis, we decided to use square regions with a side of $40''$. For low-resolution cluster lens models, the choice of a large area introduces noise, and this affects the reliability of that particular singularity map as the noise can introduce spurious singularities. For the HFF cluster lenses, the central (ra, dec) values of the Sharon group are considered as standard values whenever we compare different singularity map for an HFF cluster. This is for ensuring uniformity and the choice does not arise from any preference for one set of models. As can be seen from Table 3.1, one of the HFF clusters, MACSJ0717.5+3745, is not part of our current analysis as the corresponding singularity maps consist of a large number of spurious point singularities (please see section 3.3.1 for a discussion about noise in the singularity maps and its effects).

RELICS consists of a total of 41 cluster lenses (please see Section 2 in Coe et al. 2019). For RELICS cluster lenses, at present, the mass modeling is done by three different groups using the Lenstool (Cerny et al., 2018; Paterno-Mahler et al., 2018; Mahler et al., 2019), the LTM method (Acebron et al., 2018, 2019, 2020; Cibirka et al., 2018), and the Glafic tool (Okabe et al., 2020). The Glafic mass models have a resolution of $0.1''$, whereas most of the Lenstool mass models have a resolution between $0.1''$ to $1.0''$. Therefore, for RELICS clusters, due to the low resolution, we cannot use the Glafic or the Lenstool mass models and cannot perform a comparison between different mass model reconstruction techniques (please see Section 3.3.1 and 3.3.2 for further details about the effect of mass model resolution). The Zitrin group mass models have a resolution of $0.06''$ but consist of a large number of spurious point singularities. The reason for the high number of spurious point singularities can be the inadequate resolution or the fact that the higher-order derivatives of the lens potential are not well constrained.

Hence, in our current study, we only use one mass model for five different RELICS clusters to construct the singularity maps (see Table 3.1). The best-fit lens mass models considered here for RELICS clusters are parametric in nature and constructed by the Zitrin group using the light-traces-mass (LTM) method with Gaussian smoothing (zitrin_ltm_gauss). A more detailed comparison may become possible in future with the availability of deep, high resolution images and construction of corresponding lens models.

3.3 Results

Construction of singularity maps helps us in identifying the high magnification regions in the lens plane of a given cluster lens, which are obvious targets for the deep surveys. The high sensitivity of A_3-lines and point singularities to the lens potential encouraged us to compare the singularity maps corresponding to the different mass models for a cluster lens, which are constructed using different techniques. Such a comparison provides us information about the effects of the reconstruction methods and the presence of substructures in a cluster lens on the singularity map. Future observations of characteristic image formation around point singularities may help distinguish between different models based on present observations. In this section, we present results of our study of the construction of singularity maps for the HFF and RELICS clusters, followed by a comparison of different mass models for a cluster lens (Section 3.3.1). In Section 3.3.2, we study the stability of these singularity maps against the mass model resolution and determined the optimal resolution to construct the singularity map for a given lens. In Section 3.3.3, we estimate the number of source galaxies lying near the point singularities and the possibility of observing the corresponding characteristic image formation in upcoming all-sky surveys followed by the constraints on the source redshift using the point singularities in Section 3.3.4.

3.3.1 Singularity Maps

We use the algorithm discussed in Chapter 2 to construct the singularity maps for different lens models throughout this work. In order to keep it concise, we only present singularity maps corresponding to one cluster lens (A370) in this article. The rest of the singularity maps are available at the end of the chapter in Section 3.5. Figure 3.1, represents the singularity maps for A370 corresponding to four different mass models (please see Table 3.1). In every panel, the red and green lines are the A_3-lines cor-

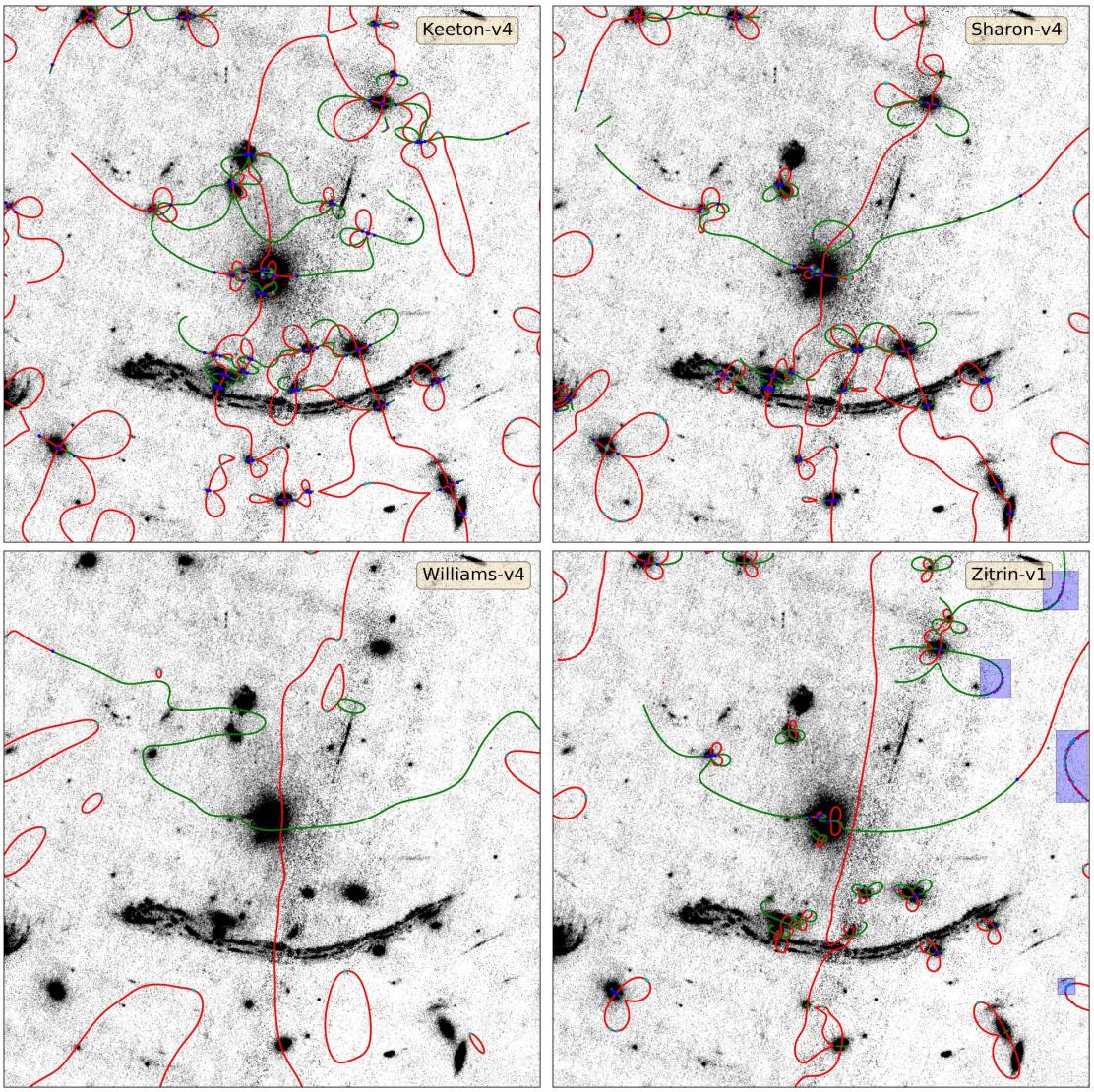

Figure 3.1: Singularity maps for the A370 cluster lens corresponding to mass models provided by four different groups (Keeton, Sharon, Williams, Zitrin): The red and green lines represent the A_3-lines corresponding to the tangential and radial cusps, respectively. The blue points denote the umbilics (hyperbolic and elliptic). At hyperbolic umbilics, one red and one green line meet with each other, whereas at elliptic umbilic, three red and three green lines meet. The cyan and magenta points represent the swallowtail singularities corresponding to the A_3^{α} and A_3^{β}-lines. The shaded regions in the lower right panel mark the noisy region in the singularity map. These regions are not included in further calculations. In each panel, the background is the cluster image in the F435W band.

responding to the α and β eigenvalues of the deformation tensor, respectively. The blue points show the hyperbolic and elliptic umbilics. The cyan and magenta colored points represent the swallowtail singularities corresponding to the α and β eigenvalues, respectively. In each panel, the background is the cluster image in the F435W band. Every map in Figure 3.1 is a $40'' \times 40''$ central square region of the cluster with center coordinates (in degrees) $(39.971355, -1.582223)$. The source redshift (z_s) in the range

between the lens redshift and $z_s \leq 10$ is used here. Singularities in this range are shown in these plots. Hence, the A_3-lines trace the location of cusps for sources up to a redshift of ten.

As one can see from Figure 3.1, different singularity maps show differences in the A_3-line structures and the number of point singularities. However, one can still identify an overall A_3-line structure similar to an elliptical lens in every panel, which represents the entire cluster as an elliptical gravitational lens (please see Chapter 2 for singularity map corresponding to an elliptical lens). These differences arise mainly due to the fact that different groups use different mass reconstruction methods, and the number of substructures used by different teams is also different, which is evident from Figure 3.1. For example, mass models from Keeton, Sharon, and Zitrin groups are reconstructed using the parametric approach, which takes into account different properties of the cluster substructures as input and finds the best-fit parameters. On the other hand, the non-parametric reconstruction by Williams group uses no information regarding the cluster substructures as an input. Hence, the singularity map corresponding to the Williams group shows the simplest A_3-line structure and least number of point singularities as their reconstruction method does not give significant weightage to the presence of cluster substructures. It is possible that substructure in their models is suppressed to some extent due to averaging over a large number of realizations in their approach. This is also evident from the fact that the best-fit mass model corresponding to the Williams group does not give a five-image configuration for a source at the giant arc's redshift ($z_s = 0.7251$) in A370. This can also be seen from the corresponding singularity map as there is no swallowtail from the center to the giant arc, which can give rise to a five-image geometry. On the other hand, all parametric mass models have swallowtails near the giant arc in the lens plane, which gives rise to five-image geometry. Looking at the singularity maps corresponding to parametric mass models, one can see that different small scale structures introduce extra A_3-lines and point singularities in the singularity maps.

As mentioned above, due to the finite amount of observational data, one cannot achieve arbitrary high resolution during cluster lens mass reconstruction. The finite resolution of lens models also introduces a few problems in singularity maps. The first problem is the noise in the singularity map, which can be seen in the bottom right panel of Figure 3.1. The low resolution directly affects the shape of the A_3-lines, and it introduces spurious swallowtails point singularities as our algorithm first identifies the A_3-lines and uses these to locate swallowtail singularities. To eliminate the effect of the noise, we do not include these spurious point singularities in our further calculations. We mark these spurious point singularities utilizing the fact that in the absence

of noise, the A_3-lines are smooth lines, which can be seen in every panel of Figure 3.1 and 3.2. However, as the noise increases, points near the A_3-lines in the lens plane also contribute to the A_3-lines and affect the local shape of the A_3-lines. This, by definition, influences the number of swallowtails in the singularity map. We manually inspect every singularity map and mark such regions. The other problem that has been introduced due to finite resolution are the missing point singularities. Sometimes when the distance between two similar kinds of point singularities is less than the grid size, our method is resolution limited and it does not find these as two different point singularities. Instead, it only assigns one point singularity into that pixel. This mainly happens in the case of hyperbolic umbilics as pair of hyperbolic umbilic forms at the position of substructures in the singularity map. However, this does not affect the overall cross-section of hyperbolic umbilics significantly, as the number of such missed out points is tiny, and most of these points get critical at very low redshifts. Hence, the contribution of these (left out) points in the cross-section is negligible.

The finite resolution of the mass models also affects the size of the singularity map. Hence, we are only able to construct singularity maps for the central region of the lens. As one goes away from the central region, the length of A_3-lines, and the total number of point singularities increases. However, the number of spurious structures introduced by noise also increases. As a result, the number of point singularities that one can see in Figure 3.1, should be considered as the lower limit of the total number of point singularities that one cluster lens has to offer.

3.3.2 Stability of Singularity Maps

One can deal with the above mentioned difficulties (noise and the left out point singularities) by increasing the resolution of the mass models. However, an increment in resolution can be computationally expensive. Apart from being computationally expensive, the other point that one needs to take into account is the stability of the singularity maps. We know that the structures in a singularity map depend on the lens potential and its higher-order derivatives in a non-linear fashion. Hence, the question arises, whether the increase in resolution can introduce new structures in a singularity map? Or do we reach convergence at some stage? Addressing this question also helps us to find out the optimal resolution for the construction of singularity maps. To answer this question, we constructed singularity maps corresponding to mass models provided by the Williams group for the HFF clusters with four different resolution values, $0.2''$, $0.1''$, $0.05''$, and

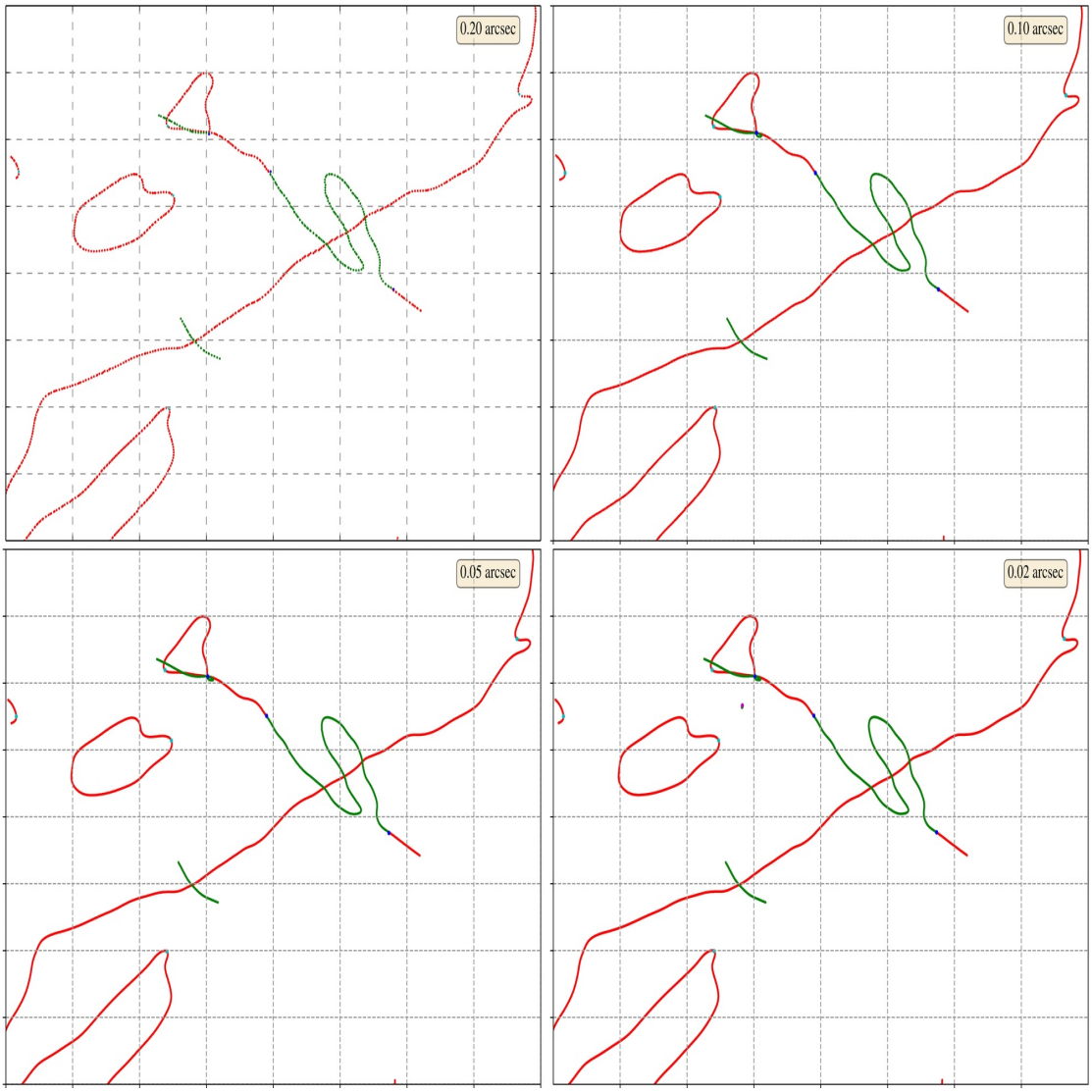

Figure 3.2: Singularity map for the MACS1149 cluster lens corresponding to four different resolution values, 0.20", 0.10", 0.05", 0.02". The color scheme is similar to the Figure 3.1. As expected, increasing the resolution of the mass map helps in resolving the small scale structures in the singularity maps. Increase in resolution does not introduce any significant extra structures in the singularity map.

$0.02''$. [3]

Figure 3.2, shows the singularity map for MACS1149 with four different resolution values, $0.2''$, $0.1''$, $0.05''$, and $0.02''$. It is apparent that increasing the resolution of the mass models helps us to better resolve the structures in the singularity maps. It does not introduce any new significant structures apart from the bottom right panel (resolution $0.02''$), where one extra loop of A_3-line corresponding to β-eigenvalue along with a

[3]The publicly available Williams group data files have a resolution of $\geq 0.2''$. However, using data files provided by Prof. Liliya Williams, we can (in principle) resolve their mass models with an arbitrary resolution, as their mass models are superposition of a large number of projected Plummer density profiles.

swallowtail makes an appearance. This is the case, at least in the case of non-parametric modeling. This is because there is no structure smaller than the resolution $0.10''$ in Figure 3.2. However, in the case of parametric models, some structures are very small even at a resolution of $0.05''$ and one can miss these structures at a resolution of $0.10''$ or $0.20''$. This is also evident from the fact that in parametric models, even at a resolution of $0.05''$, some hyperbolic umbilics are missed. Hence, the optimal resolution to construct singularity maps, in the case of both parametric and non-parametric modeling, should be of the order of $0.02''$. This can be further confirmed in the case of parametric models by making singularity maps with different resolutions (as we have done in Figure 3.2 for non-parametric models). For non-parametric mass models, somewhat low-resolution singularity maps can also do the job. However, in the case of parametric modeling, one should construct mass models with a resolution of at least $0.02''$ for construction of singularity maps. In general, the resolution of mass models should be better than or at least equal to the resolution of observations used to arrive at the map for completeness.

3.3.3 Cross-Section

Singularity maps can be used to study the variety of characteristic image formation near point singularities. This, then becomes a template for searching different image types in observations. We expect the upcoming surveys to yield a number of systems, and a quantitative prediction requires calculation of cross-section for each type of singularity.

Once we draw the singularity maps for different mass models, the next task is to determine the number of characteristic image formations near different kinds of unstable singularities which can be observed in surveys with different upcoming facilities. In order to make the estimate, we identify the range in redshift around the critical redshift z for each point singularity. We wish to choose the range such that the image formation can be identified as characteristic of the given type of singularity. As discussed in the Chapter 2 and mentioned above, image formation for different point singularities evolves differently with redshift. Hence, the redshift interval in which one can observe the characteristic image formation will also be different for different point singularities. Source redshift comes in the equation via distance ratio, $a(=D_s/D_{ds})$. Therefore we determine the corresponding distance ratio interval, $[a-\delta a, a+\delta a]$ and use it to deduce the appropriate redshift interval.

In the case of hyperbolic umbilic, one can observe the characteristic image formation at redshifts significantly smaller and larger than the critical redshift, and we choose

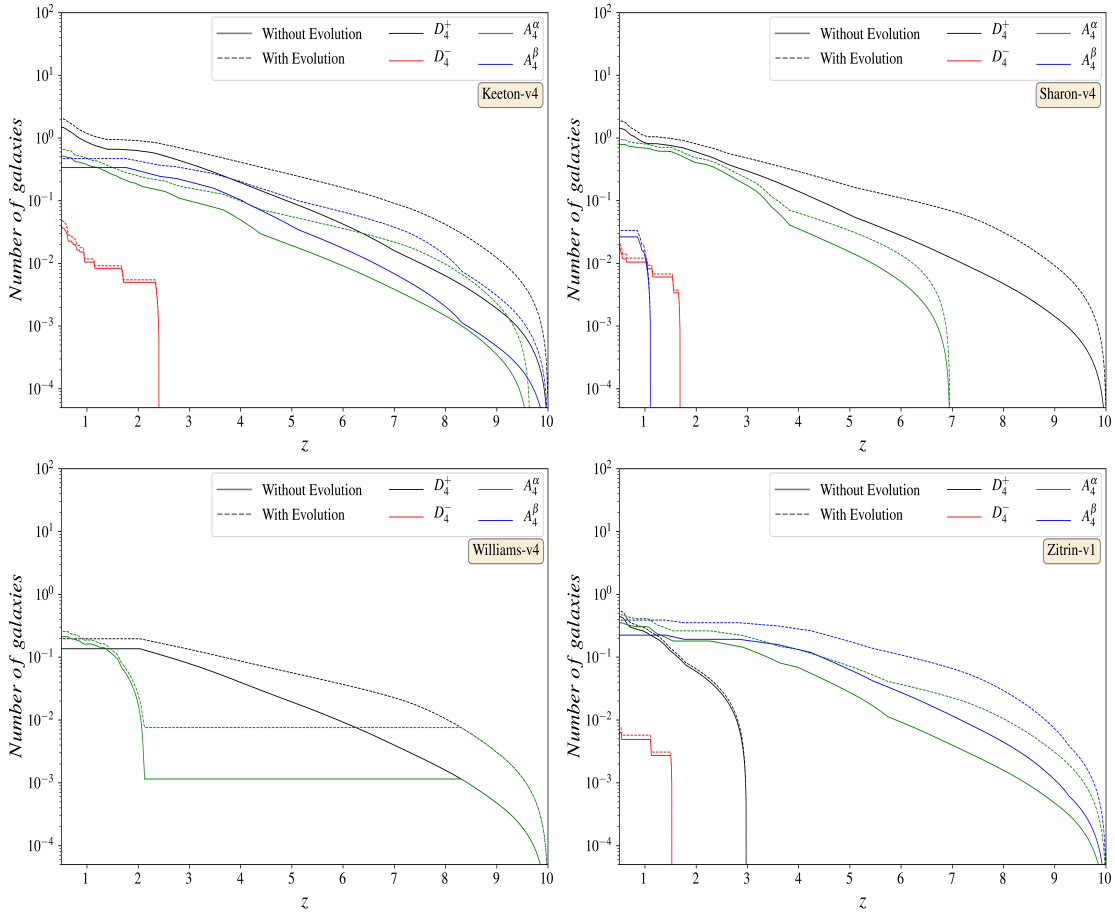

Figure 3.3: The cumulative number of source galaxies near point singularities as a function of redshift for A370 galaxy cluster: the y-axis shows the number at redshifts higher than z. Different panels are corresponding to different singularity maps in Figure 3.1, respectively. The solid lines represent the galaxy numbers calculated using the fiducial model used in C18, whereas the dashed lines indicate the galaxy numbers calculated using the model with evolving feedback (please see C18 for more details). The black and red lines denote the cumulative galaxy numbers corresponding to the hyperbolic and elliptic umbilic point singularities, respectively. Similarly, green and blue lines represent the cumulative galaxy numbers corresponding to the swallowtail singularities for A_3^α and A_3^β-lines, respectively.

$\delta a = 0.1a(z)$, where $a(z)$ is the distance ratio at the critical redshift. The choice of δa in this way also automatically takes into account the fact that at small source redshifts, the caustics in the source plane evolve more rapidly compared to the high redshifts. Hence, the distance ratio interval, $[a-\delta a, a+\delta a]$, for a point singularity is small for smaller source redshifts. As we go towards higher source redshifts, the size of the distance ratio interval increases. For swallowtail, one can only observe the characteristic image formation beyond the critical redshift. So, in the case of swallowtail singularity, the distance ratio interval modifies to $[a, a+\delta a]$, and the δa is taken to be equal to 7% of the distance ratio at the critical redshift. For elliptic umbilic, the seven image Y-shaped image formation can only be observed up to the critical redshift. Hence, for elliptic

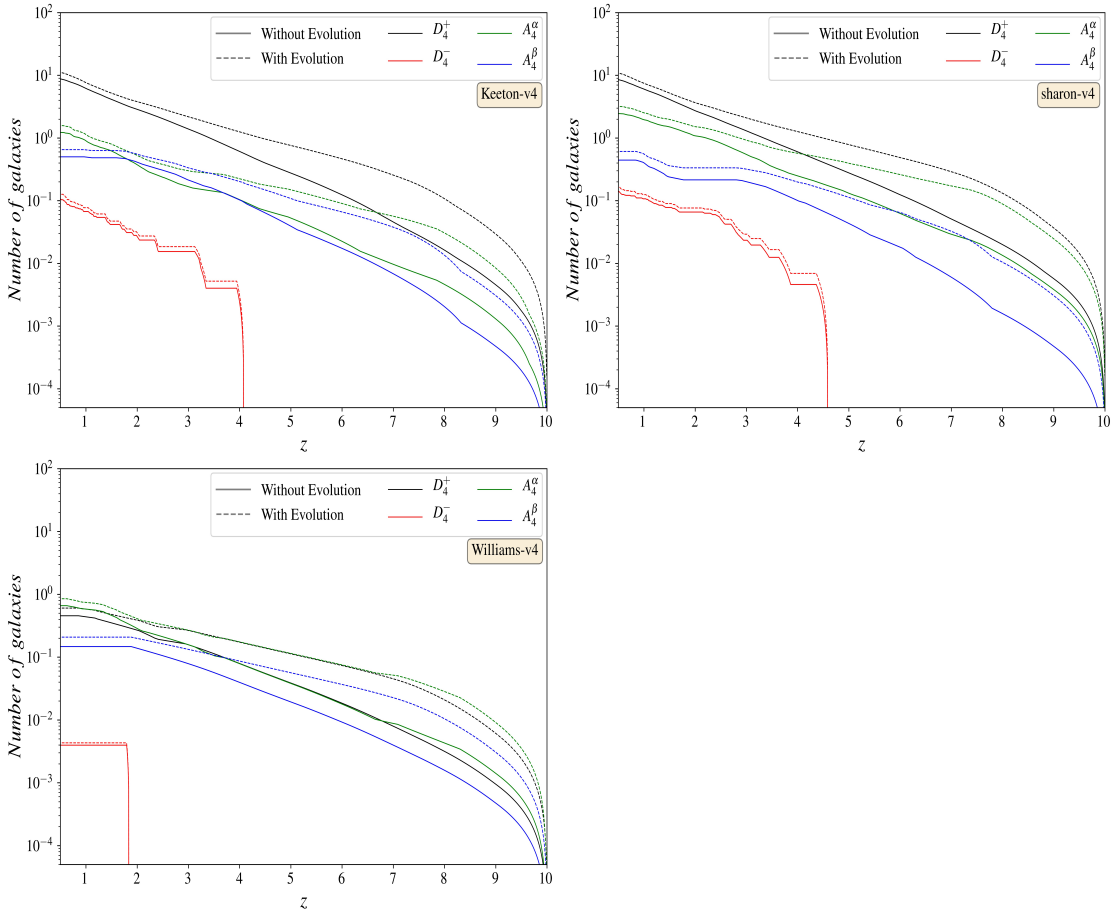

Figure 3.4: The total cumulative number of the source galaxies near point singularities as a function of redshift corresponding to the five of the HFF clusters, namely, A370, A2744, AS1063, MACS0416, and MACS1149: the y-axis shows the number at redshifts higher than z. The left, right, and bottom panels show the total galaxy numbers calculated using the Keeton, Sharon, and Williams group mass models for each cluster, respectively. Similar to Figure 3.3, the solid lines represent the galaxy numbers calculated using the fiducial model used in C18, whereas the dashed lines indicate the galaxy numbers calculated using the model with evolving feedback. The black and red lines denote the cumulative galaxy numbers corresponding to the hyperbolic and elliptic umbilic point singularities, respectively. The green and blue lines represent the cumulative galaxy numbers corresponding to the swallowtail singularities for A_3^α- and A_3^β-lines, respectively.

umbilic, the distance ratio interval modifies to $[a-\delta a, a]$, and the δa is equal to 0.5% of the distance ratio at the critical redshift as elliptic umbilics are highly sensitive to the redshift evolution.

Once we determine the redshift interval corresponding to the different point singularities, we proceed to estimate the area in the source plane around the caustics in which the source must lie to produce characteristic image formation. As we know, the magnification factor for extended sources is smaller than a point source (Diego, 2019). Hence, if a compact source such as a star lies near the caustics in the source plane, then we get

an observation of the characteristic image formation. However, such sources are very rare in cluster lensing (Kelly et al., 2018), and mostly we observe a galaxy as a source. We are mainly considering galaxies as potential sources. We consider a circular area in the source plane near the caustic structure corresponding to the point singularities with a radius of 5 kpc.

The above-chosen values of the distance ratio interval for different point singularities and source plane area near point singularities cannot be calculated mathematically. Hence, we manually estimate these numbers by observing a large number of lens systems (from galaxy to cluster scales) near point singularities and inspecting the corresponding image formations. One should keep in mind that these numbers directly affect the calculated cross-section of point singularities and should be chosen very carefully. Apart from that, as discussed in Section 3.3.1 and 3.3.2, the finite resolution of the mass maps introduces the spurious point singularities, directly affecting the corresponding point singularity cross-section. As one can see in supplementary material (Section 3.5), the number of such spurious point singularities is relatively high for RELICS clusters compared to the HFF clusters. Hence, we do not calculate the point singularity cross-section for the RELICS clusters in our current work and restrict ourselves to the HFF clusters for point singularity cross-section estimation.

The remaining information that we need is the surface density of the observed galaxies as a function of redshift. However, the surface density of observed galaxies is sensitive to the underlying models of galaxy formation and evolution as well as the waveband and limiting magnitude. We consider a recent study by Cowley et al. (2018, heareafter C18) for JWST. In C18, a part of the work was to estimate the number of galaxies observed in different bands of JWST, considering an exposure time 10^4 seconds (please see C18 for a detailed description). The useful quantity for our analysis, the surface density of observed galaxies, is shown in Figures 9 and 10 of C18. Here, for simplicity, we only consider one NIRCam filter, F200W, for our analysis.

Figure 3.3, represents the cumulative distribution of the number of galaxies as a function of redshift which can provide us the characteristic image formation corresponding to different point singularities for A370: we have plotted the numbers expected at higher redshifts. Different panels in Figure 3.3 correspond to the singularity maps in Figure 3.1 for different mass models, respectively. The solid lines represent the galaxy numbers with the fiducial model, and the dashed lines correspond to a model with evolving feedback (please see C18 for further details). The black, red, green, and blue lines are cumulative source galaxy numbers that provide the characteristic image formations corresponding to the hyperbolic umbilic, elliptic umbilic, swallowtail for

A_3^{α}-line, and swallowtail for A_3^{β}-line, respectively.

As one can see from Figure 3.3, the probability of finding a source galaxy at $z \geq 1$ with characteristic image formation near hyperbolic umbilic or swallowtail for A_3^{α}-line is an order of magnitude higher for the Keeton/Sharon group mass models compared to the Williams group mass model. This is due to the fact that the number of point singularities in the Keeton/Sharon group mass models is much higher than the Williams group mass models (please see Figure 3.1). On the other hand, the number of galaxies for the Zitrin group mass model lies somewhat in between the galaxy numbers for Keeton/Sharon and William models.

This difference in the number of observed galaxy sources near point singularities can also be seen in Figure 3.4. Figure 3.4 represents the composite cumulative distribution of the number of galaxies near point singularities for five of the HFF clusters we are using for the present study. The left, right, and bottom panels correspond to the Keeton, Sharon, and Williams group mass models, respectively. Here we did not calculate the galaxy numbers near point singularities for the Zitrin group mass models (zitrin_nfw) as the coresponding singularity maps contain spurious point singularities. However, the singularity maps are available in Section 3.5 (except for MACS1149 since the corresponding zitrin_nfw mass model is not available). One can again see that the parametric mass reconstruction models give an order of magnitude more source galaxies with characteristic image formations at redshifts $z_s \gtrsim 1$ compared to the non-parametric mass reconstruction models. From the Keeton and the Sharon group mass models, one expects to observe at least one image formation near swallowtail in every HFF clusters and (on average) one image formation near hyperbolic umbilic in every HFF cluster. On the other hand, from the Williams group mass models, one expects to observe at least one image formation near swallowtail and one image formation near hyperbolic umbilic in all of the HFF clusters. Given this pattern, singularity maps corresponding to the non-parametric mass models can be used to estimate the minimum number of expected characteristic image formation in the upcoming surveys.

Our current analysis is based only on the best-fit models provided by different groups. Each of these models also has uncertainties associated with them due to the finite number of constraints available (Lotz et al., 2017; Priewe et al., 2017). These uncertainties affect the caustic structure in the source plane, and as a result, will also affect the point singularity cross-section. However, we cannot estimate these uncertainties at present as we will need to construct the singularity map for each ensemble map to do that, and the corresponding potential or deflection maps are not available online (except for the Williams and Zitrin group). A detailed investigation of the effects of these

uncertainties is subjected to our future study and will be presented in the forthcoming Chapter.

3.3.4 Redshift Measurements

We have mentioned above that point singularities are critical only for certain source redshifts, and the corresponding characteristic image formation is only observable within a finite range for source redshift. This encourages us to ask the question: can these point singularities be used to constrain the source redshift as the corresponding characteristic image formation is only visible within a specific redshift range? In order to address this question, we consider the distance ratio intervals, for characteristic image formation near different kinds of point singularities. We find that point singularities constrain the source redshift more strongly at smaller source redshifts than higher source redshifts. For example, if a hyperbolic umbilic is critical at source redshift one for a lens at redshift 0.35, then the characteristic image formation is observable in the redshift range $\approx [0.85, 1.25]$. If the hyperbolic umbilic is critical at redshift below one, then the redshift interval for the characteristic image formation further narrows down considerably. On the other hand, if the hyperbolic umbilic is critical at redshift five, then the image formation can be observed in the redshift range $\approx [2.2, 10]$. The same argument can also be used for other point singularities. However, for other point singularities the redshift range is smaller than the redshift range for hyperbolic umbilic (please see subsection 3.3.3) and these can provide stronger constraints on source redshift than the hyperbolic umbilics, if observed. Hence, point singularities are more useful in constraining the source redshift at smaller redshifts. One can also understand such behavior from the fact that the caustic structure evolves more rapidly at smaller redshifts compared to higher redshifts. The elliptic umbilic can be useful at higher redshifts; however, the observational cross-section for the corresponding image formation is negligible (please see Figure 3.3 and 3.4). It is also important to keep the context of a known lens map for this discussion, if there are uncertainties in the lens map then it may be better to find out the source redshift to constrain the lens map.

3.4 Conclusion

We have constructed singularity maps corresponding to ten different galaxy clusters selected from the HFF and the RELICS survey. To construct singularity maps, we followed the algorithm developed and discussed in the Chapter 2. Such a singularity map

traces all the optimal sites for the upcoming deep surveys in the cluster lens plane as well as mark the locations of all the point singularities. Point singularities are very sensitive to the lens potential as these have a non-linear dependence on higher-order derivatives of the lens potential. Hence, these are also sensitive to the mass reconstruction methods as different methods use a different set of assumptions to construct mass models. We have constructed singularity maps corresponding to five of the HFF clusters (Table 3.1), considering mass models reconstructed using both parametric (Keeton, Sharon, and Zitrin groups) and non-parametric (Williams group) techniques. On the other hand, for five of the RELICS clusters, we only considered one mass model (provided by the Zitrin group) for each cluster lens. We find that the number of point singularities corresponding to parametric and non-parametric mass models is very different. The parametric models give a large number of point singularities compared to non-parametric models where only a handful of point singularities are present (Figure 3.1). This also affects the estimated number of galaxy sources with characteristic image formation as the parametric models yield an order of magnitude large number of such sources compared to non-parametric models (Figure 3.3 and 3.3). We suspect that the assumption of mass associated with each of the galaxies in the lensing cluster is the reason for this (Jullo et al., 2007). As the number of point singularities corresponding to the non-parametric mass models is the least, one can use these models to compute the lower limit on the observation of characteristic image formation in the upcoming all-sky surveys. We find that the number of point singularities is significantly higher than estimates in earlier studies (Orban de Xivry & Marshall, 2009). Recently Meneghetti et al. (2020) pointed out an order of magnitude discrepancy in substructure lenses in the observed galaxy clusters (which are modeled using the parametric approach) and simulated galaxy clusters. While the discrepancy with LCDM is disputed (Bahé, 2021; Robertson, 2021), one can expect a significant difference in the number of point singularities that may arise as lens models are better constrained with more images.

The key takeaway from our analysis is that the predicted number of instances of point singularities in cluster lenses is likely to be much higher than estimated earlier (Orban de Xivry & Marshall, 2009). We expect to get at least one hyperbolic umbilic and one swallowtail image formation for a source at $z > 1$ for every five clusters with JWST. This estimation is based on the non-parametric mass models corresponding to the Williams group, and it can be considered as a lower limit since the number of point singularities is much higher in parametric models than non-parametric models.

We have not considered galaxy lenses in our analysis. Each galaxy scale lens has at least one pair of hyperbolic umbilics (as these are modeled as elliptical mass distributions with more details thrown in) and sometimes a few swallowtails (if a substructure

also exists). Including the galaxy lenses will further increase the possibility of observing the image formations near point singularities.

Addition of substructure always adds more singular points, hence the numbers and distribution of singular points can be connected with the amount of substructure in clusters. Image formation near a point singularity consists of multiple images lying very close to each other in the lens plane: the characteristic image formation being different for each type of singularity. This opens up the possibility of measuring the relative time delay between these images. Such measurements are possible even if the multiple images are not well resolved (Borra, 2008). Along with the time delay analysis, one can also construct an atlas of realistic image configurations near point singularities for training and identification using machine learning programs in the upcoming surveys (Davies et al., 2019). These possibilities are the subject of our future studies and the results will be presented in forthcoming publications.

3.5 Supplementary Material

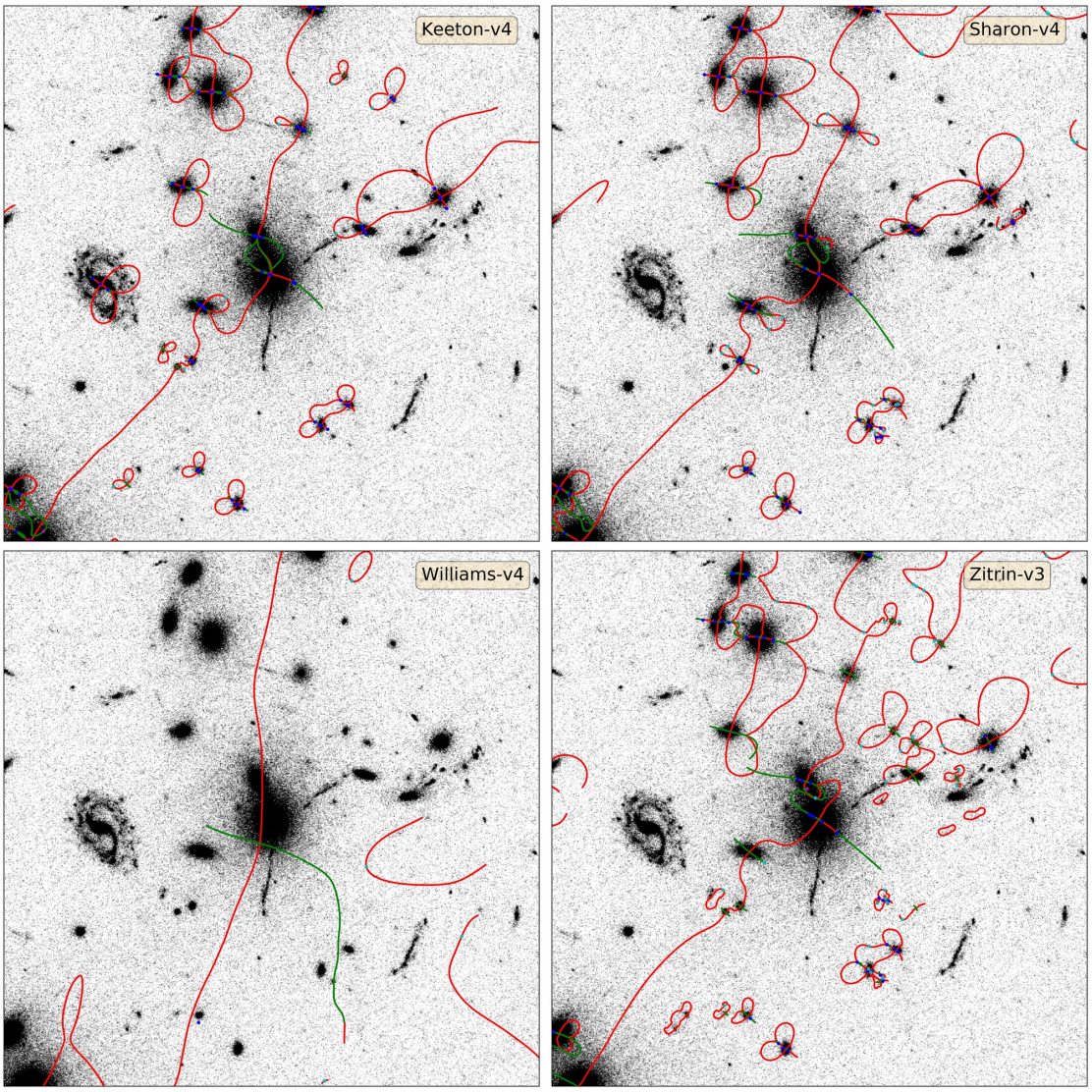

Figure 3.5: Singularity maps for the A2744 cluster lens corresponding to mass models provided by four different groups (Keeton, Sharon, Williams, Zitrin): The red and green lines represent the A_3-lines corresponding to the tangential and radial cusps, respectively. The blue points denote the umbilics (hyperbolic and elliptic). At hyperbolic umbilics, one red and one green line meet with each other, whereas at elliptic umbilic, three red and three green lines meet. The cyan and magenta points represent the swallowtail singularities corresponding to the A_3^{α} and A_3^{β}-lines. The shaded regions in the lower right panel mark the noisy region in the singularity map. These regions are not included in further calculations. In each panel, the background is the cluster image in the F435W band.

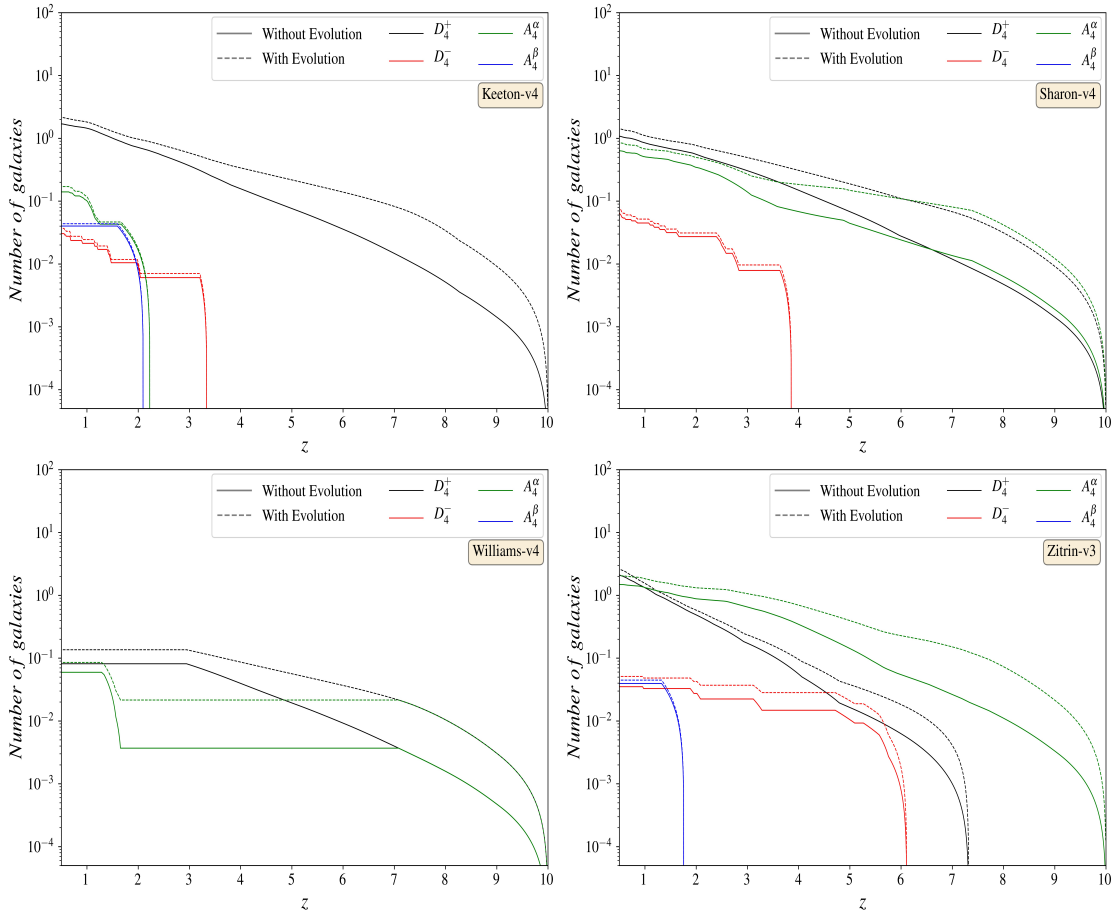

Figure 3.6: The cumulative number of source galaxies near point singularities as a function of redshift for A2744 galaxy cluster: the y-axis shows the number at redshifts higher than z. Different panels are corresponding to different singularity maps in Figure 3.5, respectively. The solid lines represent the galaxy numbers calculated using the fiducial model used in C18, whereas the dashed lines indicate the galaxy numbers calculated using the model with evolving feedback (please see C18 for more details). The black and red lines denote the cumulative galaxy numbers corresponding to the hyperbolic and elliptic umbilic point singularities, respectively. Similarly, green and blue lines represent the cumulative galaxy numbers corresponding to the swallowtail singularities for A_3^α and A_3^β-lines, respectively.

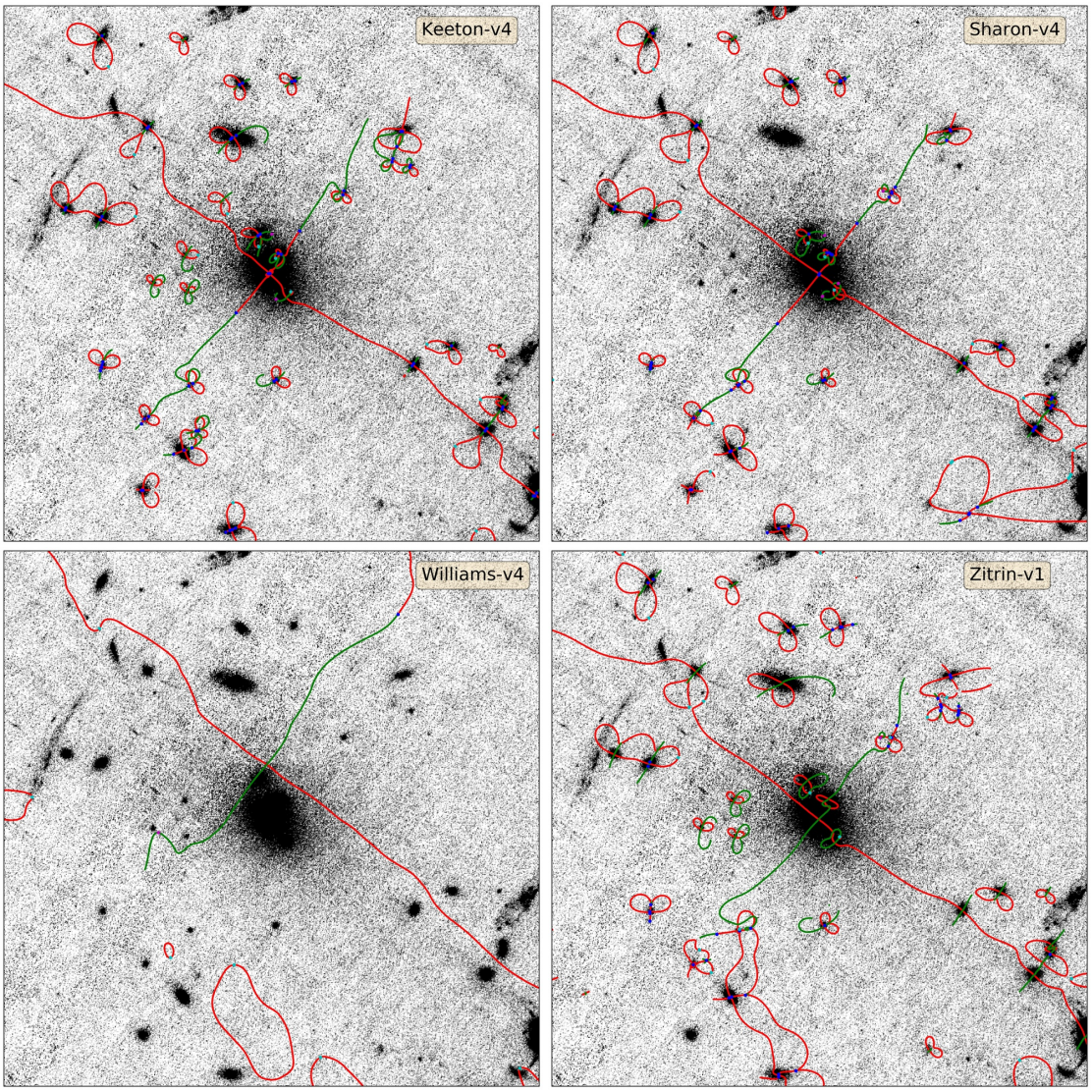

Figure 3.7: Singularity maps for the AS1063 cluster lens corresponding to mass models provided by four different groups (Keeton, Sharon, Williams, Zitrin): The red and green lines represent the A_3-lines corresponding to the tangential and radial cusps, respectively. The blue points denote the umbilics (hyperbolic and elliptic). At hyperbolic umbilics, one red and one green line meet with each other, whereas at elliptic umbilic, three red and three green lines meet. The cyan and magenta points represent the swallowtail singularities corresponding to the A_3^{α} and A_3^{β}-lines. The shaded regions in the lower right panel mark the noisy region in the singularity map. These regions are not included in further calculations. In each panel, the background is the cluster image in the F435W band.

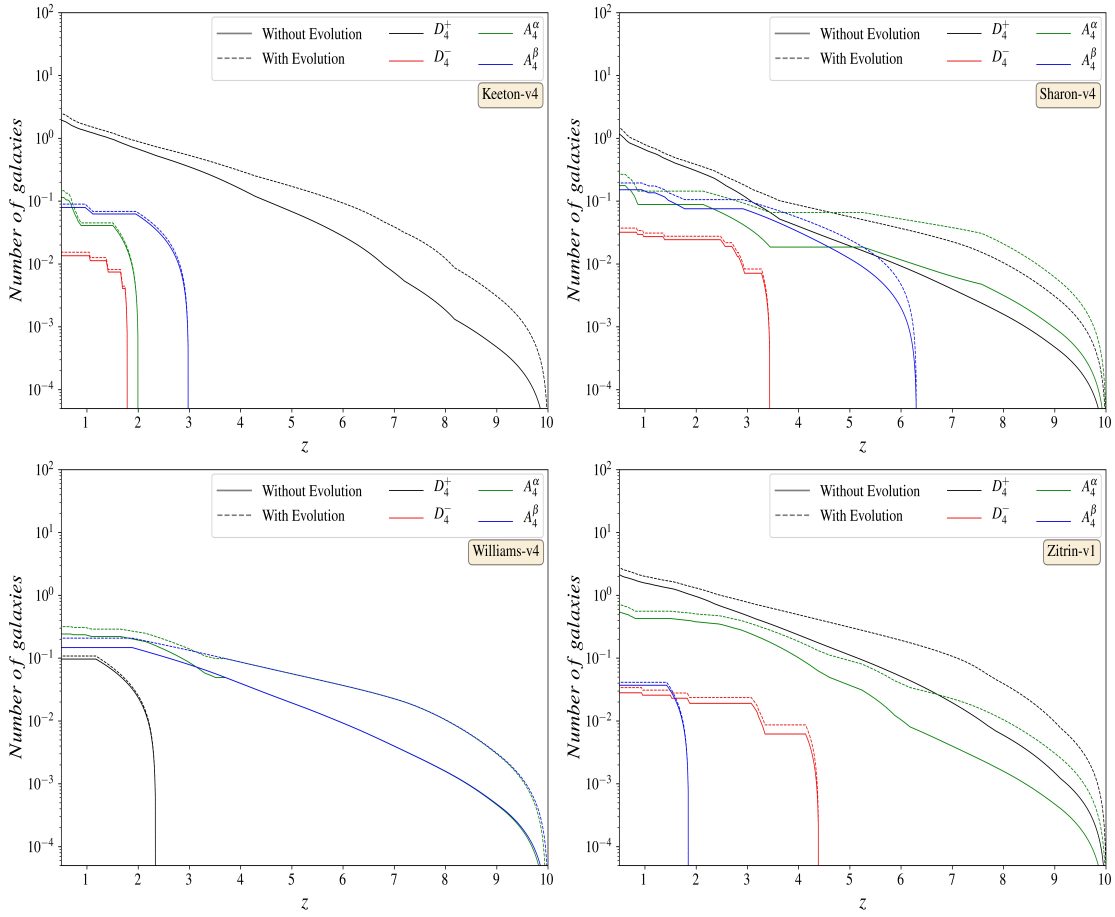

Figure 3.8: The cumulative number of source galaxies near point singularities as a function of redshift for AS1063 galaxy cluster: the y-axis shows the number at redshifts higher than z. Different panels are corresponding to different singularity maps in Figure 3.7, respectively. The solid lines represent the galaxy numbers calculated using the fiducial model used in C18, whereas the dashed lines indicate the galaxy numbers calculated using the model with evolving feedback (please see C18 for more details). The black and red lines denote the cumulative galaxy numbers corresponding to the hyperbolic and elliptic umbilic point singularities, respectively. Similarly, green and blue lines represent the cumulative galaxy numbers corresponding to the swallowtail singularities for A_3^α and A_3^β-lines, respectively.

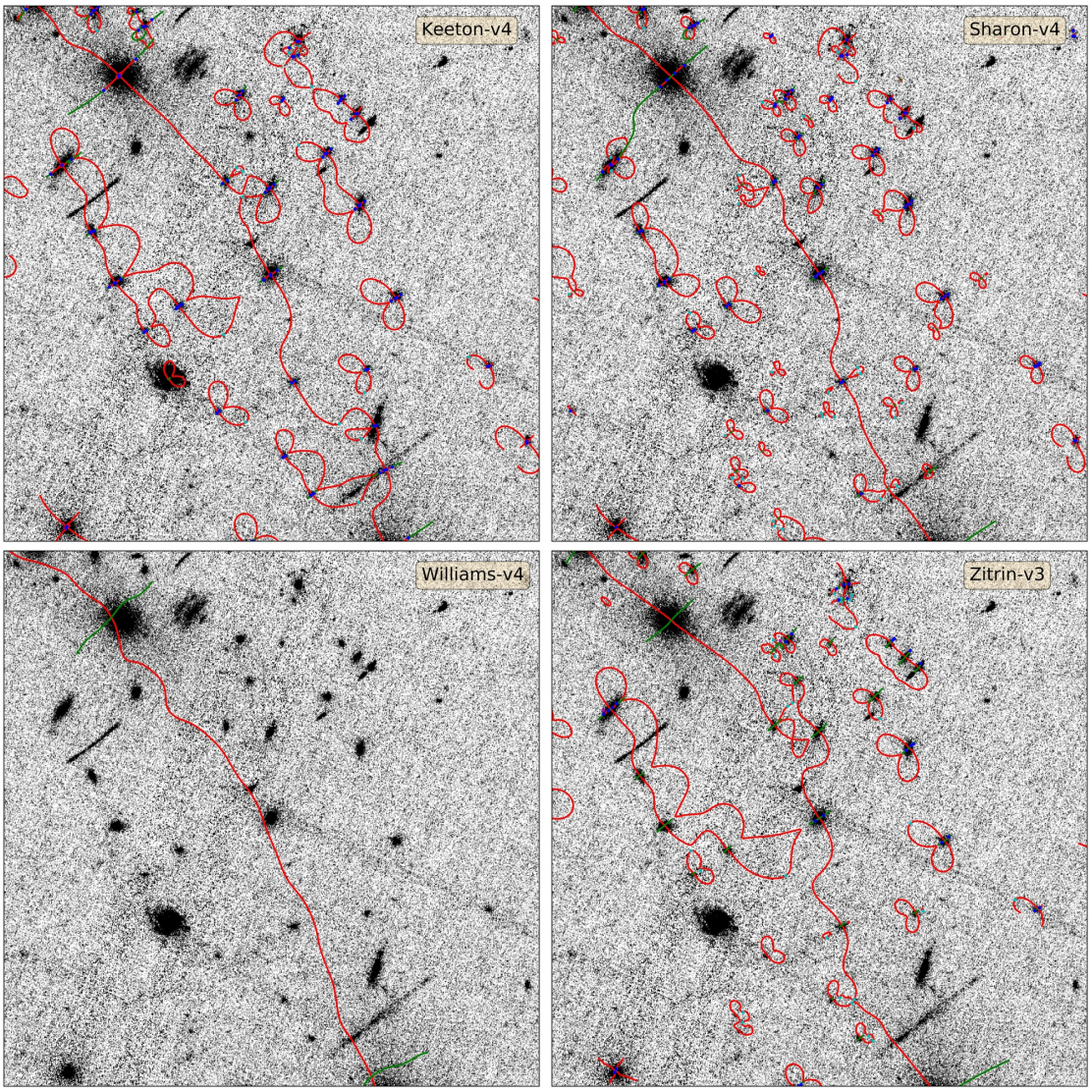

Figure 3.9: Singularity maps for the MACS0416 cluster lens corresponding to mass models provided by four different groups (Keeton, Sharon, Williams, Zitrin): The red and green lines represent the A_3-lines corresponding to the tangential and radial cusps, respectively. The blue points denote the umbilics (hyperbolic and elliptic). At hyperbolic umbilics, one red and one green line meet with each other, whereas at elliptic umbilic, three red and three green lines meet. The cyan and magenta points represent the swallowtail singularities corresponding to the A_3^{α} and A_3^{β}-lines. The shaded regions in the lower right panel mark the noisy region in the singularity map. These regions are not included in further calculations. In each panel, the background is the cluster image in the F435W band.

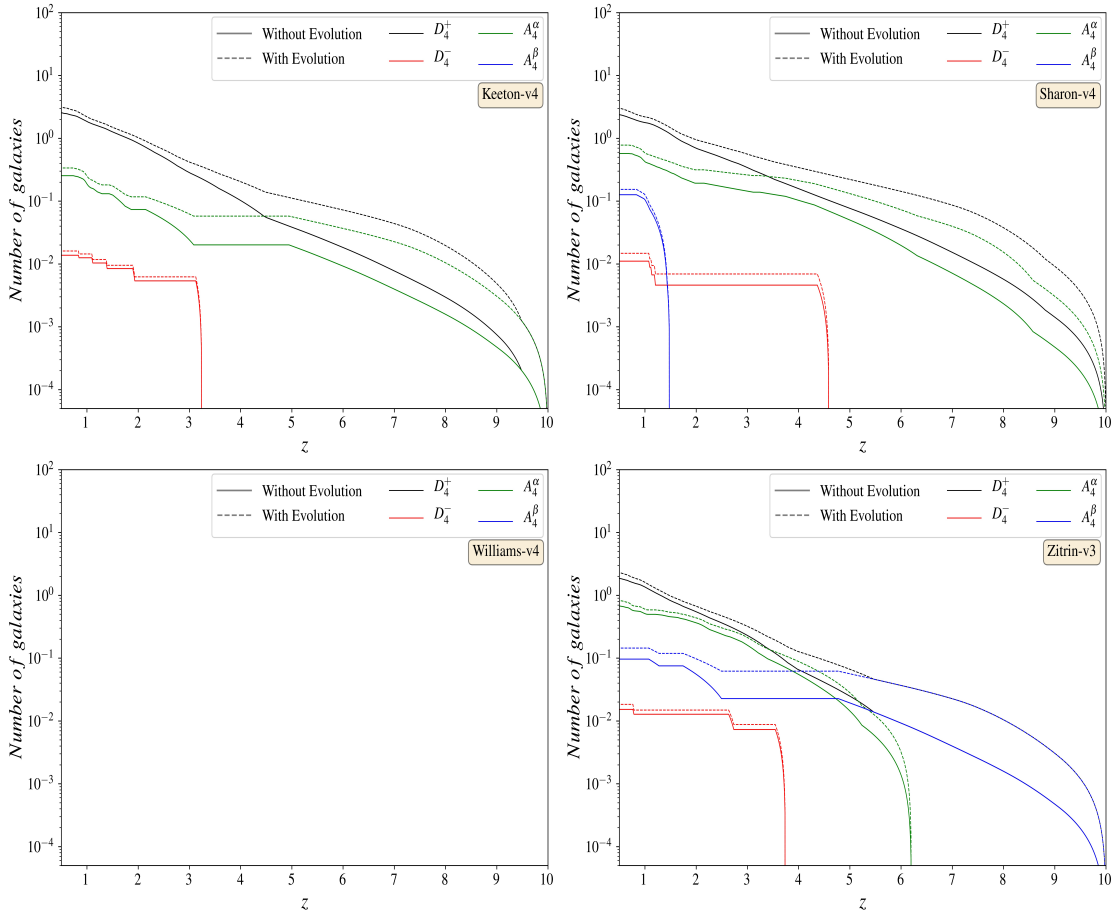

Figure 3.10: The cumulative number of source galaxies near point singularities as a function of redshift for A370 galaxy cluster: the y-axis shows the number at redshifts higher than z. Different panels are corresponding to different singularity maps in Figure 3.9, respectively. The solid lines represent the galaxy numbers calculated using the fiducial model used in C18, whereas the dashed lines indicate the galaxy numbers calculated using the model with evolving feedback (please see C18 for more details). The black and red lines denote the cumulative galaxy numbers corresponding to the hyperbolic and elliptic umbilic point singularities, respectively. Similarly, green and blue lines represent the cumulative galaxy numbers corresponding to the swallowtail singularities for A_3^α and A_3^β-lines, respectively.

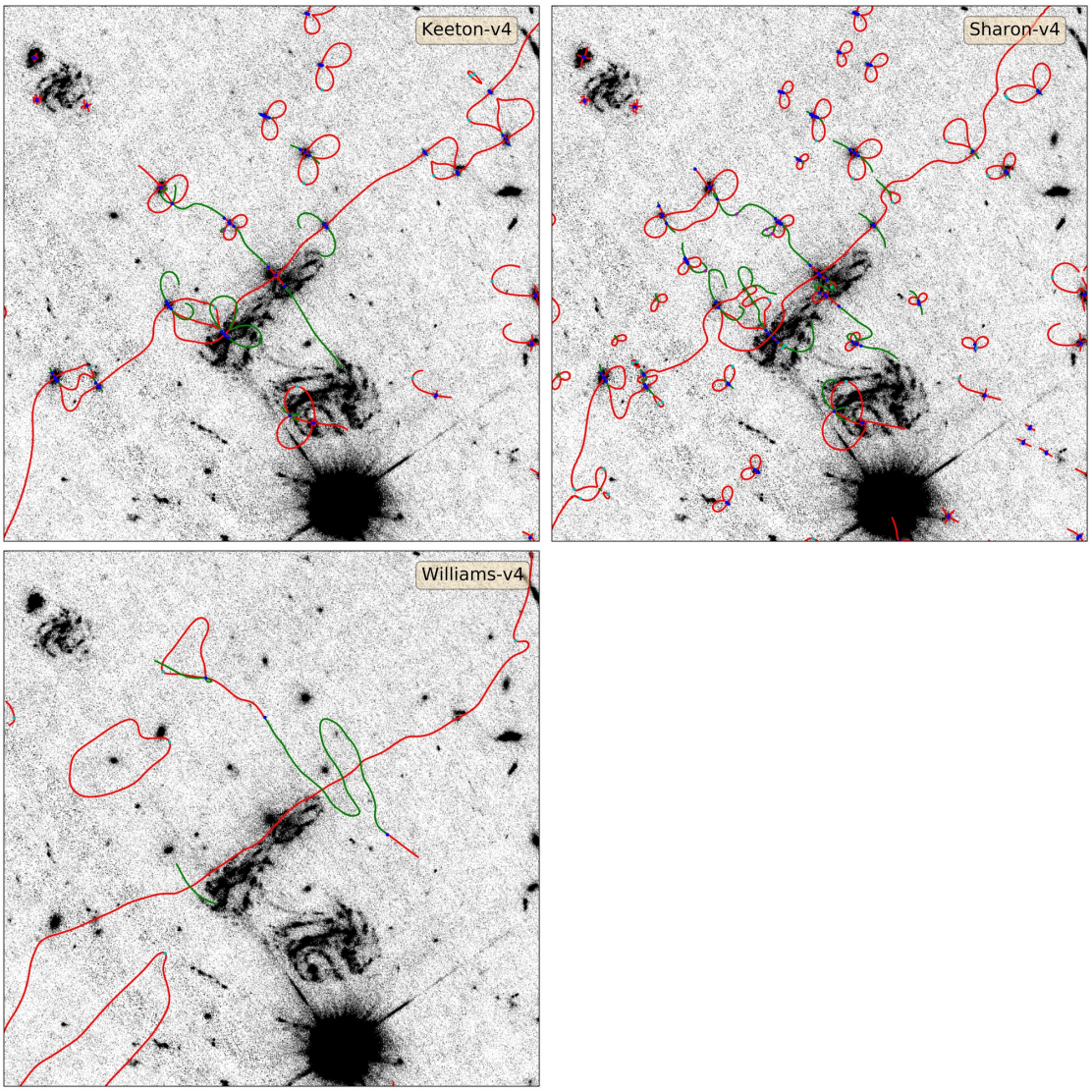

Figure 3.11: Singularity maps for the MACS1149 cluster lens corresponding to mass models provided by four different groups (Keeton, Sharon, Williams, Zitrin): The red and green lines represent the A_3-lines corresponding to the tangential and radial cusps, respectively. The blue points denote the umbilics (hyperbolic and elliptic). At hyperbolic umbilics, one red and one green line meet with each other, whereas at elliptic umbilic, three red and three green lines meet. The cyan and magenta points represent the swallowtail singularities corresponding to the A_3^{α} and A_3^{β}-lines. The shaded regions in the lower right panel mark the noisy region in the singularity map. These regions are not included in further calculations. In each panel, the background is the cluster image in the F435W band.

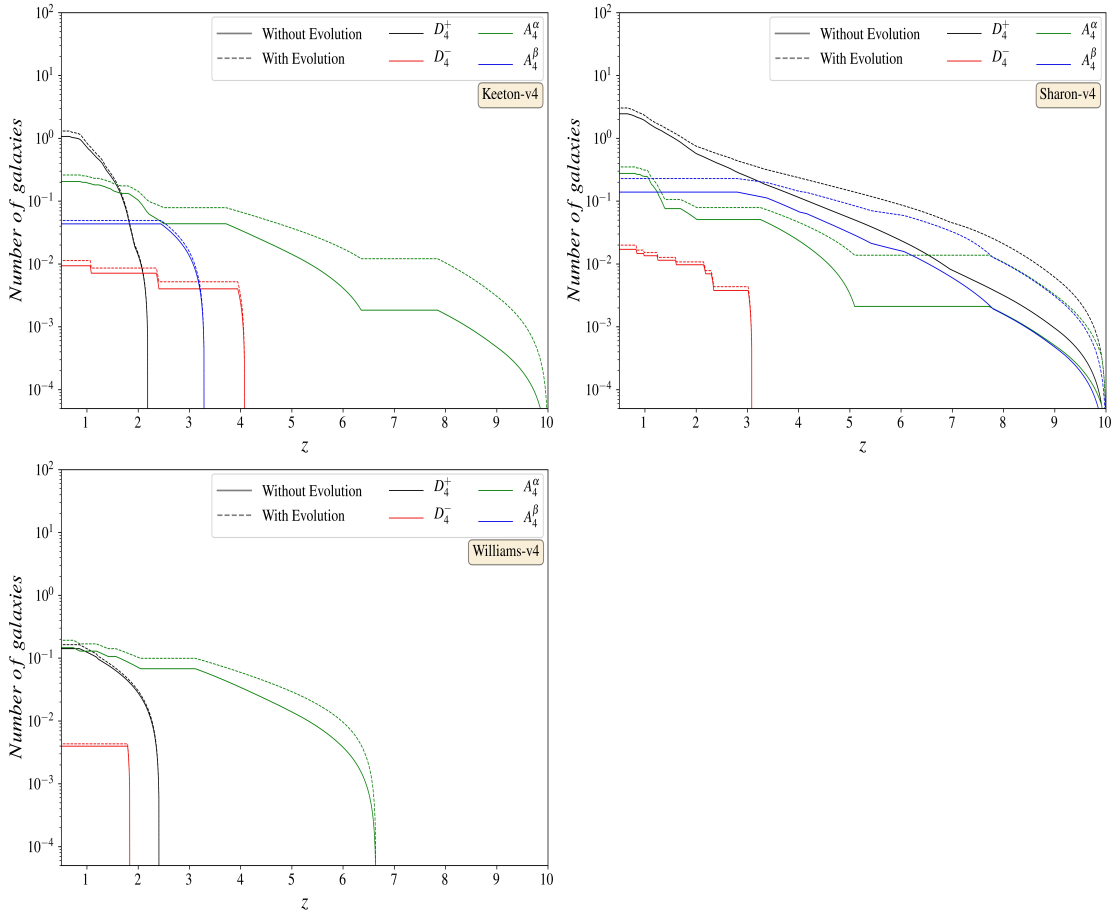

Figure 3.12: The cumulative number of source galaxies near point singularities as a function of redshift for A370 galaxy cluster: the y-axis shows the number at redshifts higher than z. Different panels are corresponding to different singularity maps in Figure 3.11, respectively. The solid lines represent the galaxy numbers calculated using the fiducial model used in C18, whereas the dashed lines indicate the galaxy numbers calculated using the model with evolving feedback (please see C18 for more details). The black and red lines denote the cumulative galaxy numbers corresponding to the hyperbolic and elliptic umbilic point singularities, respectively. Similarly, green and blue lines represent the cumulative galaxy numbers corresponding to the swallowtail singularities for A_3^α and A_3^β-lines, respectively.

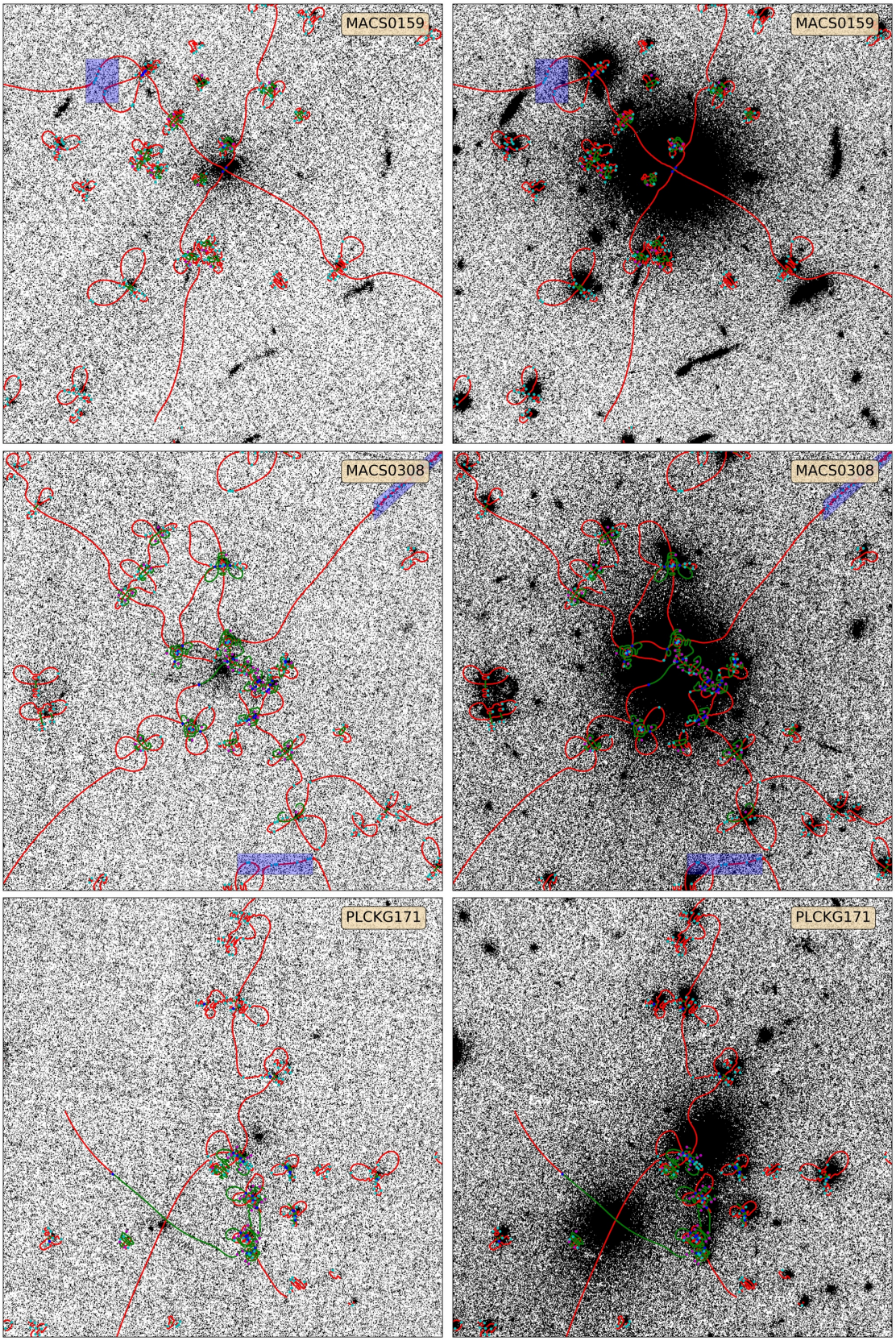

Figure 3.13: Singularity maps of RELICS clusters for mass models provided by the Zitrin group (zitrin ltm gauss). The name of the cluster is written in every panel. In each panel of left (right) column, the background is the cluster image in the F435W (F606W) band.

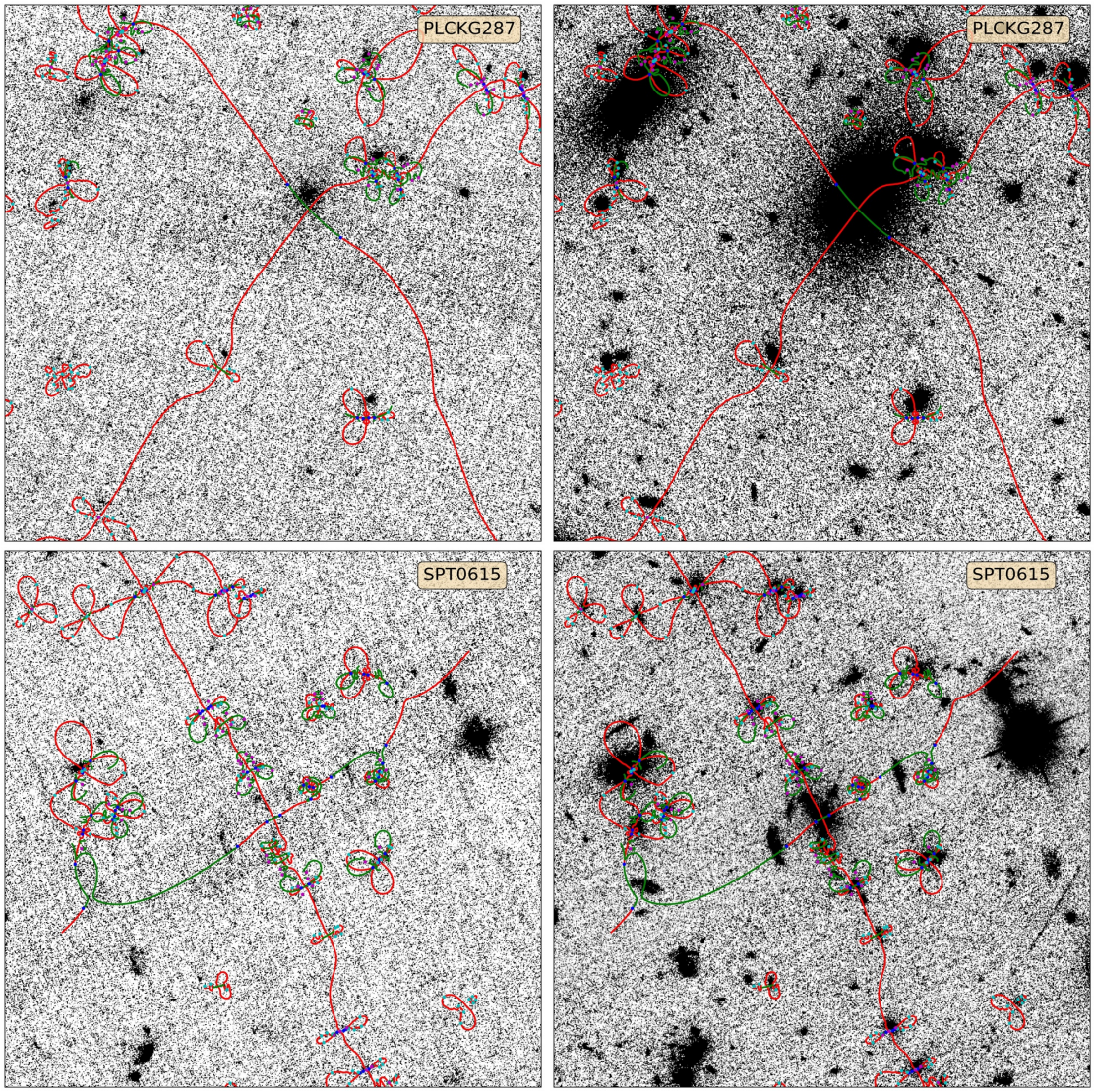

Figure 3.13: Cont.

Chapter 4

Exotic Image Formation in Cluster Lenses – II: Uncertainties

This chapter is based on:

Meena, A. K., Ghosh, A., Bagla J. S., Williams, L. L. R., "Exotic Image Formation in Strong Gravitational Lensing by Clusters of Galaxies – II: Uncertainties", **2103.13617**, Submitted to MNRAS.

4.1 Introduction

In order to use galaxy clusters as a probe, we need to model their mass distributions. However, as the data from the observation is limited, one cannot model the mass distribution of these clusters with arbitrary precision and resolution. As a result, to reconstruct the lens mass distribution, different groups start with different sets of prior. For examples, light trace mass (LTM, Broadhurst et al., 2005; Zitrin et al., 2009) parametric mass reconstruction assumes that the mass distribution in the cluster lenses follows the light distribution. On the other hand, the non-parametric (free-form, Liesenborgs et al., 2007) mass reconstruction methods do not rely on any preliminary information related to the mass model and only take into account the strong and weak (Liesenborgs et al., 2020) lensing data. Hybrid mass reconstruction methods take input from both parametric and non-parametric approaches (Sendra et al., 2014). Due to the finite amount of data and different set of priors, it is possible that these different methods give different results when applied on the same cluster lens (e.g., Smith et al., 2009; Zitrin & Broadhurst, 2009). Hence, it is very important to compare these different techniques in

case of simulated as well as real lenses to improve these methods and for more robust predictions (e.g., Meneghetti et al., 2017; Priewe et al., 2017; Rodney et al., 2015; Remolina González et al., 2018; Raney et al., 2020). Each of these methods results into the best-fit mass model parameters and uncertainties associated with them. One avenue to observe the effect of these uncertainties is the cluster lens magnification maps. For the best-fit lens mass model, one will have a certain area in the lens plane that gives higher magnification than a threshold value. However, once we account for the statistical uncertainties, the area with a magnification greater than the threshold area is not a unique number; instead, it will be denoted by a range. As a result, various observational estimates (like the number of highly magnified galaxies) are also subjected to these uncertainties.

In our previous work, we have described the method to locate these unstable singularities for a given lens model (Meena & Bagla, 2020b, hereafter paper I) and applied this method in the case of actual cluster lenses (Meena & Bagla, 2021, hereafter paper II). The final output of this method is a singularity map containing all the point singularities and A_3-lines. Since these A_3-lines correspond to cusps in the source plane, they mark the high-magnification regions in the lens where image formation near cusps will occur (three or more lensed images lying near each other). The point singularities depend on the second and higher-order derivatives of the lens potential. Hence, they are very sensitive to the presence of small/intermediate-scale structures and the variations in the lens parameters. As a result, the singularity maps corresponding to the parametric and non-parametric mass models can be very different for the same cluster lens As pointed out in paper II, parametric mass models give significantly larger number of point singularities due to the small scale structures compared to non-parametric mass models.

In our current work, we study the effect of the statistical uncertainties associated with the reconstructed lens mass model parameters on the singularity maps and the higher-order singularity cross-section. In order to study the effect of mass model uncertainties on the singularity maps, we have considered two simulated galaxy cluster lenses, Irtysh I and II from Ghosh et al. (2020, hereafter GWL20) and all of the six galaxy cluster lenses from the *Hubble Frontier Fields (HFF) survey*. The lens mass reconstruction of all of these cluster lenses has been done using Grale[1] (Liesenborgs et al., 2007). We choose the Grale mass models as the corresponding singularity maps are simplest and provide a lower limit on the point singularity cross-section (paper II). Further, as the Grale mass model does not make any assumption about density profiles of substructure, the reconstruction is independent of the nature of dark matter. Due to

[1] https://research.edm.uhasselt.be/jori/grale2/

the simple nature, we can construct singularity maps for a larger region of the lens plane without introducing spurious point singularities. Apart from that, different Grale runs for a cluster lens give independent mass maps. Hence, there is no correlation between different mass maps reconstructed for a lens using Grale that may not be true for the parametric mass models. For simulated clusters, Irtysh I and II, we construct the singularity maps for the original mass models, for the individual runs (with 150, 500, 1000 lensed images) and for the final best-fit mass model. For HFF clusters, we construct the singularity maps for the individual runs and for the best-fit mass model obtained by the averaging of the individual runs.

As we know that the A_3-lines in the singularity maps correspond to the cusps in the source plane. Hence, a singularity map also gives the information about the number of cusps formed in the source plane at a given source redshift. By drawing the critical lines for a given source redshift overlaid on the singularity map, one can calculate the number of cusps in the source plane by counting the points where a critical line and corresponding A_3-line cut each other. Following that, we also estimate the (tangential and radial) arc cross-section in case of both simulated and HFF cluster lenses. The source galaxy luminosity function has been taken from Cowley et al. (2018, hereafter C18). In C18, authors estimate the number of galaxies expected in the deep galaxy surveys with the JWST in different the filters. In our present study, we only considered the expected galaxy population in one JWST filter, F200W (please see C18 for more details).

This Chapter is organized as follows. In Section 4.2, we present our results for simulated Irtysh clusters. The corresponding singularity maps are discussed in Section 4.2.1, followed by the discussion of the redshift distribution of singularities in Section 4.2.2. The results for the HFF clusters are presented in Section 4.3. The corresponding singularity maps, redshift distribution of singularities, and the arc cross-section are discussed in Section 4.3.1, Section 4.3.2, and Section 4.3.3, respectively. Summary and conclusions are presented in Section 4.4.

4.2 Simulated Clusters

In paper II, it has been shown that the parametric and non-parametric mass models for a given HFF cluster show a significant difference in both cusp and point singularity cross-section. However, each mass model has uncertainties associated with it due to the finite amount of observational data. As a result, these uncertainties also affect the results derived from the reconstructed mass models. In this section, we study the effect of these

uncertainties on the singularity maps corresponding to reconstructed mass models for simulated galaxy clusters. We have considered two simulated clusters, Irtysh I and II from GWL20. GWL20 reconstructed free-form mass models using Grale for both Irtysh I and II with three different sets of multiple images, 150, 500, 1000. The lens mass reconstruction with 150 images corresponds to the current observational scenario, whereas the 500 and 1000 multiple image cases correspond to future observations with the *Hubble Space Telescope* (HST) and *James Webb Space Telescope* (JWST). For each case, the final output is forty individual mass models and the final best-fit mass model that is the average of these forty individual mass models. We refer the reader to look into GWL20 for more details. Hereafter, for simplicity, the average mass models for 1000, 500, 150 image cases for Irtysh I/II will be referred as Irtysh IA/IIA, IB/IIB, IC/IIC.

4.2.1 Simulated Clusters: Singularity Maps

Once we have all the reconstructed mass models, we construct the singularity maps for all individual mass models and also for the final averaged one and the original mass models. To construct the singularity maps, we chose a resolution of $0.06''$ in the lens plane to calculate relevant quantities. As discussed in paper II, for mass models reconstructed using Grale, such a resolution of mass maps is adequate for constructing singularity maps. The singularity maps cover sources upto a redshift of ten. The singularity maps for the original and final averaged mass models for Irtysh I and II are shown in Figure 4.1 and 4.2. In each panel, the red and green lines represent the A_3-lines corresponding to the α and β eigenvalues of the deformation tensor. The (hyperbolic and elliptic) umbilics are shown by the blue points, whereas the swallowtail singularities corresponding to α and β eigenvalues are denoted by cyan and magenta points, respectively. One example of singularity maps corresponding to individual runs for Irtysh IA/IB/IC, IIA/IIB/IIC is shown in Figure 4.8. For both Irtysh I and II, we see that final averaged mass maps are not able to recover the contribution of the marginally critical structures in the singularity maps. In a singularity map, such structures can be located by looking for the isolated A_3-lines. Even if some of the individual runs are able to recover contribution from such marginal structures, it may be possible that these structures are not present in the final best-fit mass models due to the averaging over forty individual mass reconstruction. On the other hand, it is also possible to have some additional contribution from the spurious structures which are not present in the original mass distribution, as can be seen in Irtysh IIA in Figure 4.2.

Apart from that, one can also notice differences between the A_3-line structures in the

singularity maps near the core region of Irtysh clusters in the original and reconstructed mass models. These differences may be a result of the fact that in the reconstruction of Irtysh I and II, there are no sources below redshift one. This difference is more significant between the original and individual runs (Figure 4.8), but the averaging in the final best-fit mass model decreases this difference and brings the reconstructed mass distributions closer to the original ones.

4.2.2 Simulated Clusters: Redshift Distribution of Singularities

In this subsection, we study the redshift distribution of the point singularities for Irtysh I and II. In Figure 4.3, we represent the point singularities for different mass models as a function of redshift. Here we compare the number of singularities in the original Irtysh I and II mass models with the corresponding individual reconstructed mass models and with the corresponding final averaged mass model. For example, the top-left panel of Figure 4.3 shows the number of singularities in the original Irtysh I (thin lines), the number of singularities in the final averaged Irtysh IA mass model (thick dotted lines), and the average number of singularities in the corresponding individual runs (thick dashed lines). The error bars represent the one-sigma scatter within these forty individual runs. The red lines represent the (hyperbolic + elliptic) umbilics. Here, we are not discriminating between hyperbolic and elliptic umbilics as the number of elliptic umbilics is very small compared to the hyperbolic umbilics. The green and blue lines represent the number of swallowtail singularities corresponding to α and β eigenvalues of the deformation tensor, respectively.

In each panel of Figure 4.3, for source redshift < 2, we notice that the number of singularities in individual runs is significantly large compared to the number of singularities in the original Irtysh mass models, which is also evident from the individual runs in Figure 4.8. This is due to the fact that Grale introduces a significant number of structure (which decrease as the number of lensed images increase) at different positions in each individual reconstruction, and as GWL20 do not have any sources at redshift < 1, this effect is more significant in the central regions. As we move towards the higher source redshifts, the difference between original and individual run starts to narrow down. Although, the individual runs still predict slight excess of point singularities compared to the actual mass models.

Although the individual runs give a significant excess of point singularities below source redshift 2, such excess does not occur in the final averaged mass models. This behavior is expected from the fact that the averaging over multiple individual runs

smooths out spurious structures and brings the final reconstructed mass model closer to the original mass model, although most of the time with slight underestimation of the point singularities. The averaging over multiple realizations sometimes also introduces a small number of spurious point singularities at high redshifts, for example, as seen in the Irtysh IA, Irtysh IIB, and Irtysh IIC panels in Figure 4.3. However, the number of these spurious singularities is not significant ($\lesssim 2$ from Figure 4.3).

4.3 HFF Clusters

Under the *Hubble Frontier Fields (HFF) Survey*[2] program, *Hubble Space Telescope* observed a total of six massive merging clusters (see Lotz et al. 2017 for more details). For every HFF cluster, different groups have reconstructed mass models using parametric, non-parametric, and hybrid (a combination of parametric and non-parametric) methods (e.g., Diego et al., 2007; Bradač et al., 2005; Jauzac et al., 2015; Johnson et al., 2014; Lam et al., 2014; Merten et al., 2011; Mohammed et al., 2016; Oguri, 2010; Sendra et al., 2014; Williams et al., 2018b; Zitrin et al., 2013). To study the statistical uncertainties on the singularity maps, we consider the non-parametric HFF cluster mass models. These mass models for HFF clusters are reconstructed using the free-form method Grale. There are two reasons for choosing these mass models for the HFF clusters:
(1) The best-fit Grale mass models for HFF clusters give the simplest singularity maps compared to other techniques as shown in paper II and put the lower limit on the point singularity cross-section. Hence, it is worthwhile to check how statistical uncertainties affect the lower limit.
(2) In paper II, we only considered the central $40'' \times 40''$ region for the analysis. This choice was made due to the increasing number of spurious singularities in the parametric mass models as we go away from the center of the cluster. Hence, it will not be useful to analyze the effect of uncertainties on the singularity map in the presence of artifacts. However, such a problem does not exist for these non-parametric mass models as the singularity map is very simple and a resolution of $< 0.1''$ is sufficient enough as shown in paper II.

Similar to the Irtysh clusters, for every HFF cluster, Grale provides forty individual mass maps and one best-fit mass map that is the average of these forty mass maps. Depending on the number of images used in the reconstruction, there are different versions of the reconstructed mass models available. Here, we are using the v4 mass models for

[2] https://archive.stsci.edu/prepds/frontier/

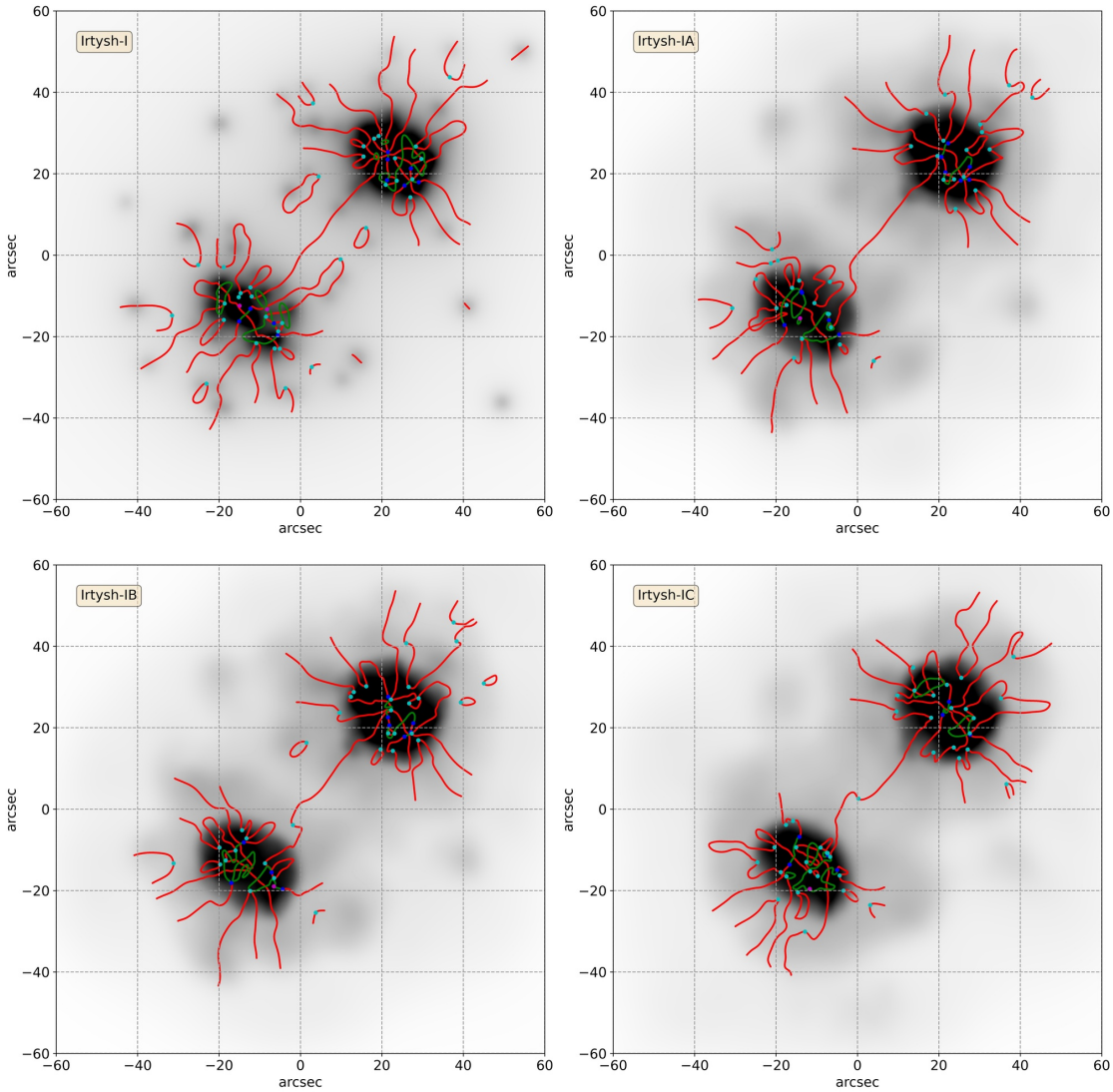

Figure 4.1: Singularity maps for original and reconstructed Irtysh I mass models: The top-left panel represents the singularity map corresponding to the original Irtysh I mass models. The top-right, bottom-left, bottom-right panels represent the singularity maps for Irtysh IA, IB, IC, respectively. In each panel, the red and green lines represent the A_3-lines corresponding to the α and β eigenvalues of the deformation tensor. The blue points represent the location of (hyperbolic and elliptic) umbilics. The cyan and magenta points represent the swallowtail singularities corresponding to the α and β eigenvalues of the deformation tensor. In each panel, the background is the corresponding normalized mass distribution in the lens plane.

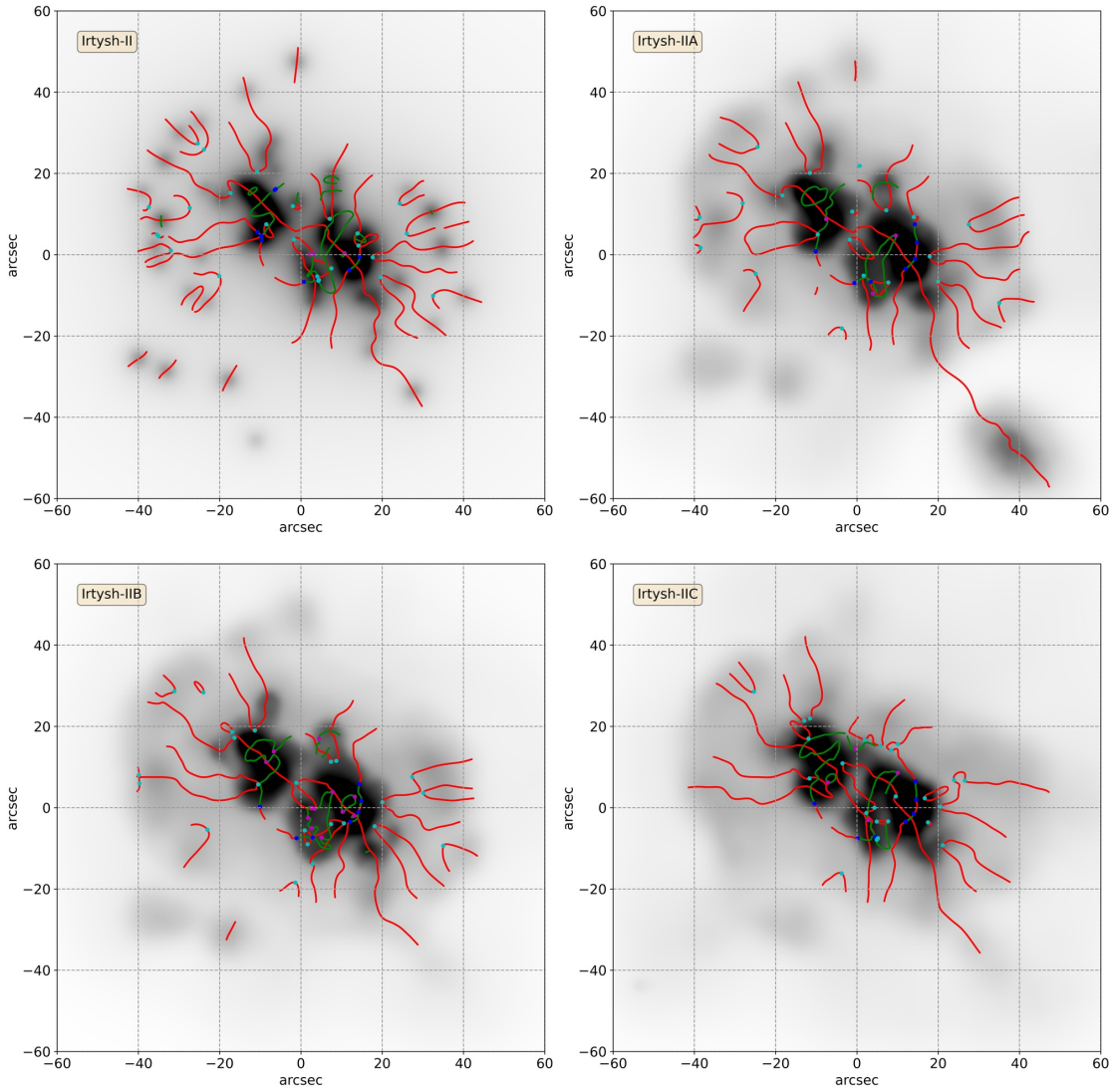

Figure 4.2: Singularity maps for original and reconstructed Irtysh II mass models: The top-left panel represents the singularity map corresponding to the original Irtysh II mass models. The top-right, bottom-left, bottom-right panels represent the singularity maps for Irtysh IIA, IIB, IIC, respectively. In each panel, the red and green lines represent the A_3-lines corresponding to the α and β eigenvalues of the deformation tensor. The blue points represent the location of (hyperbolic and elliptic) umbilics. The cyan and magenta points represent the swallowtail singularities corresponding to the α and β eigenvalues of the deformation tensor. In each panel, the background is the corresponding normalized mass distribution in the lens plane.

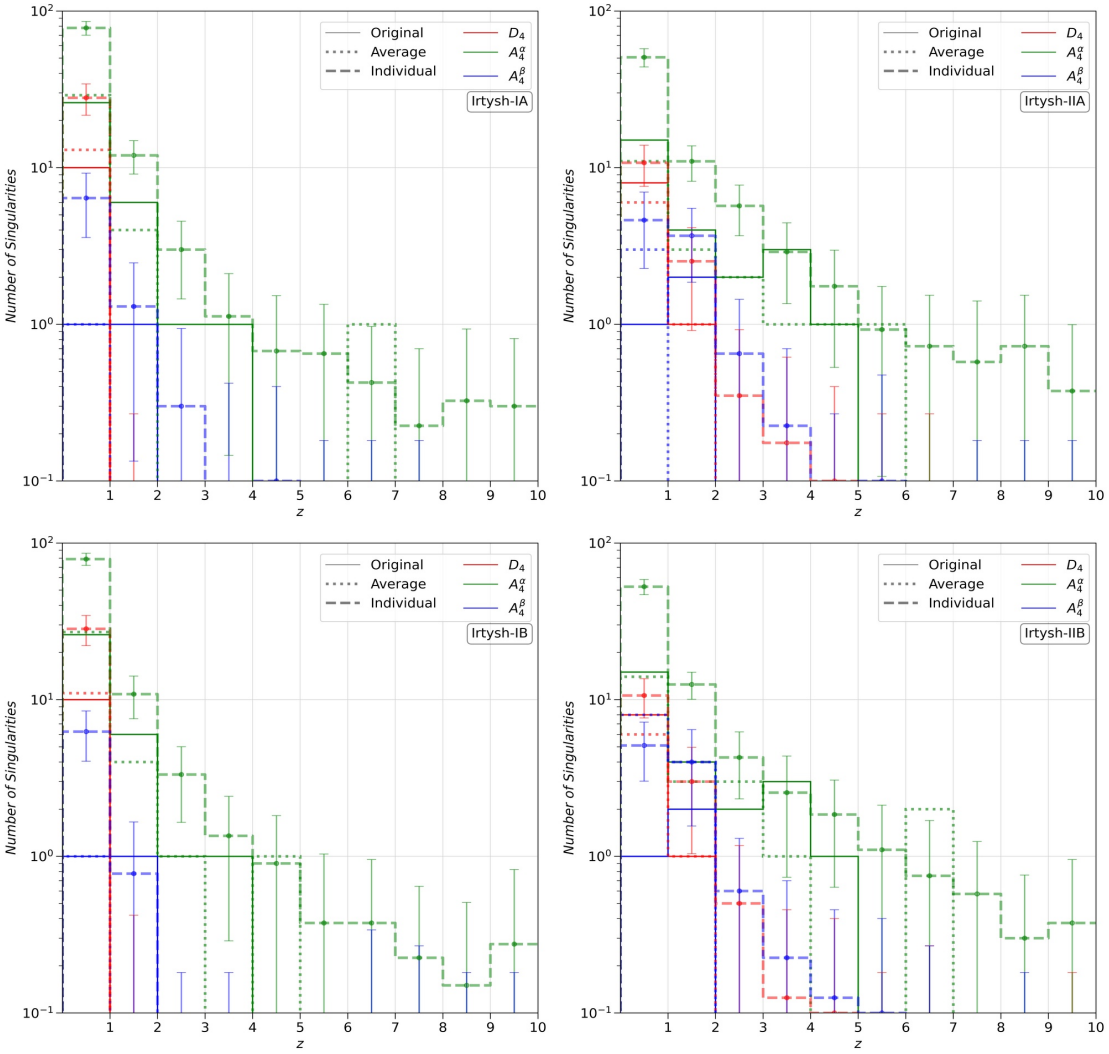

Figure 4.3: Number of singularities as a function of redshift in Irtysh I and II: In each panel, of left (right) column, the thin lines represent the number of singularities corresponding to the original Irtysh I (II). The thick dotted lines represent the number of singularities corresponding to the final averaged mass models of Irtysh I and II (the corresponding cluster name is written in each panel). The thick dashed lines show the average number of singularity in individual mass models for Irtysh I and II. The error bars represent the corresponding one sigma scatter. The red lines represent the distribution of (hyperbolic+elliptic) umbilics. The green and blue lines represent the distribution of swallowtail singularities corresponding to α and β eigenvalues of the deformation tensor.

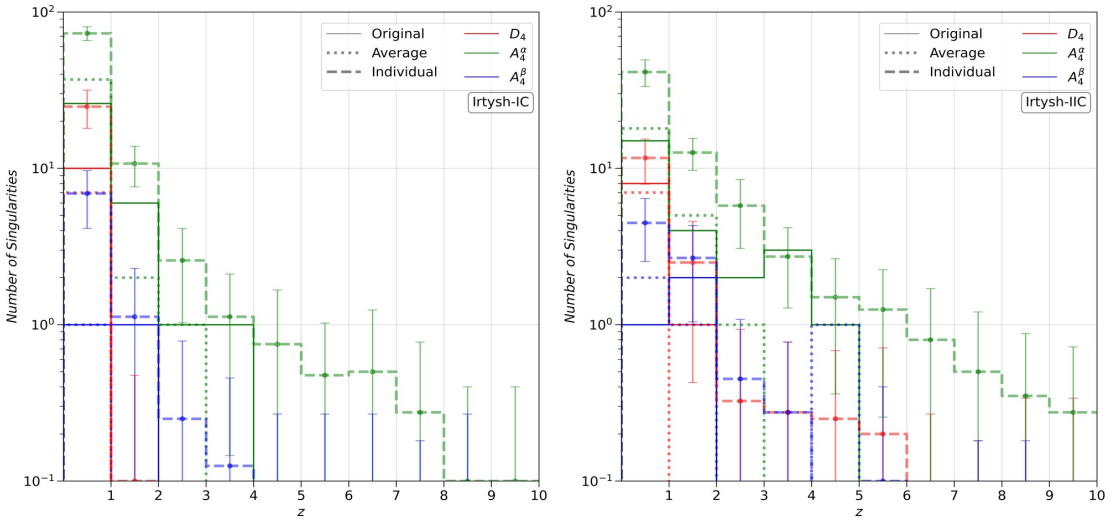

Figure 4.3: Cont.

all of the HFF clusters, and, for simplicity, we will be using the abbreviated names for the HFF cluster lenses.

4.3.1 HFF Clusters: Singularity Maps

Following the procedure used for simulated clusters, we reconstruct the singularity maps for individual and the best-fit mass models of the HFF clusters. The best-fit mass model singularity maps for the HFF clusters are shown in Figure 4.4. Here again, the singularity maps are drawn for sources upto redshift ten. The red and green lines show the A_3-lines corresponding to the α and β eigenvalues of the deformation tensor. The blue, cyan, and magenta points represent the (hyperbolic and elliptic) umbilics, swallowtail for α, and swallowtail for β eigenvalue, respectively. The online available v4 mass models have a resolution of $\geq 0.2''$. However, in our current work, we use a resolution of $0.06''$ for all of the HFF clusters. Although, as mentioned above, a resolution of $\sim 0.1''$ is sufficient for Grale mass models but, in order to be more certain that we did not miss any point singularities, we chose a resolution of $0.06''$ (please see discussion about stability of point singularities in paper II).

We can see in Figure 4.4 that the A370 yields a very complex singularity map compared to other HFF clusters. Hence, the cross-section for image formation near a cusp or a point singularity is maximum for the A370 in the HFF clusters. One can also see that the point singularity cross-section calculation done in paper II was based on the central region of $40'' \times 40''$; however, the full singularity map extends upto a much bigger region in the lens plane for a source redshift of ten. Hence, the estimations done in

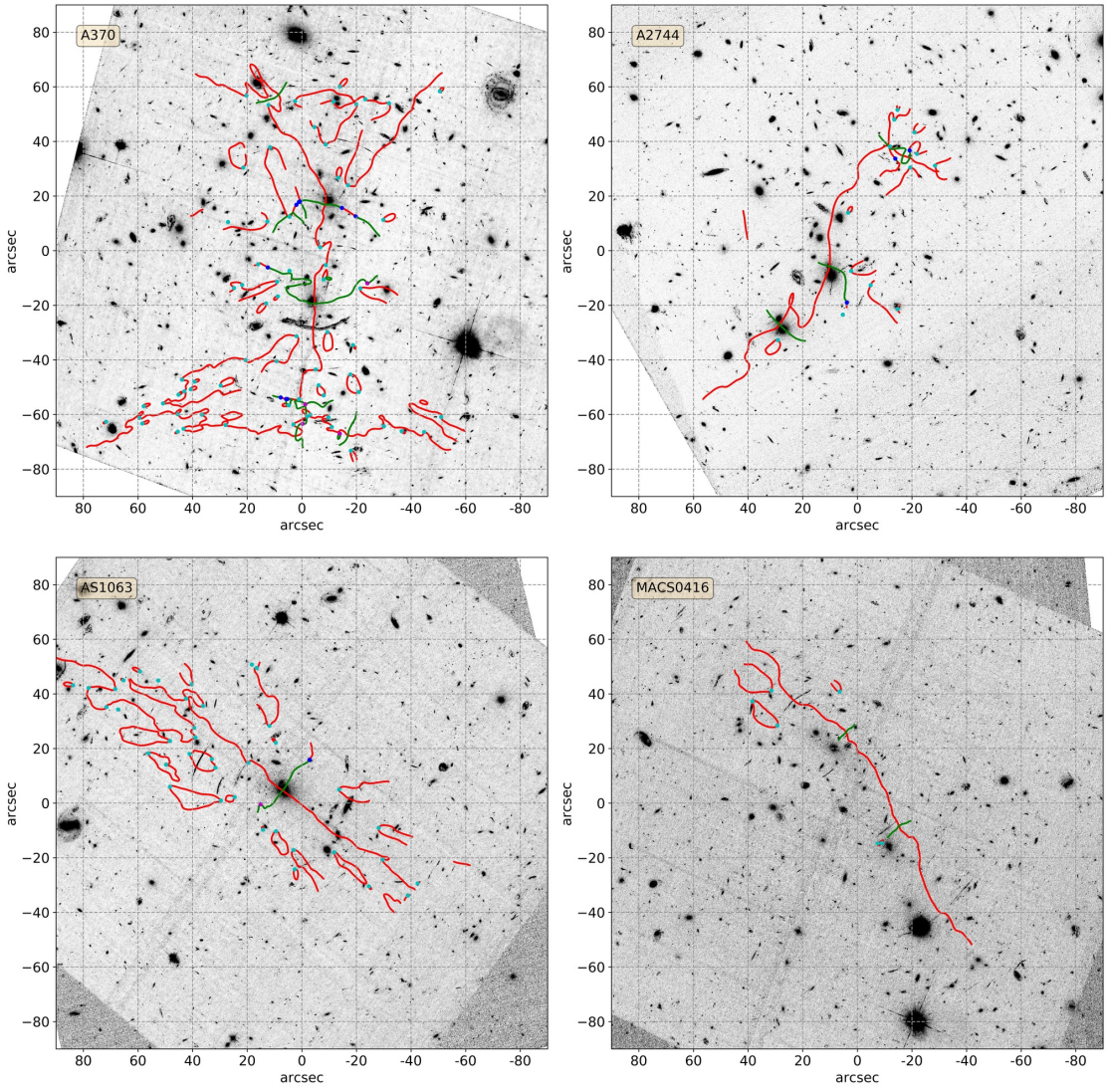

Figure 4.4: Singularity maps for HFF clusters: Every panel represents the singularity map for one of the HFF clusters. The name of the corresponding cluster is written in the upper left corner. In each panel, the red and green lines represent the A_3-lines corresponding to the α and β eigenvalues of the deformation tensor. The blue points represent the location of (hyperbolic and elliptic) umbilics. The cyan and magenta points represent the swallowtail singularities corresponding to the α and β eigenvalues of the deformation tensor. In each panel, the background is the cluster image in F435W band.

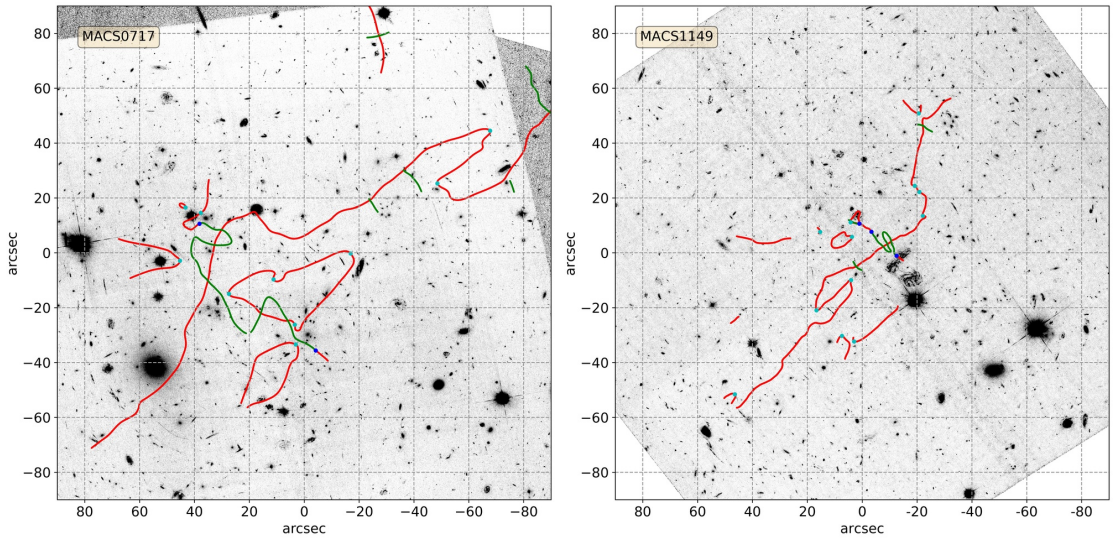

Figure 4.4: Cont.

paper II are actually underestimations. Due to consideration of the central region, the cross-section of the hyperbolic umbilics was more than the swallowtails corresponding to the α eigenvalues. However, looking at the complete singularity maps in Figure 4.4, one can see that the cross-section for the image formation near swallowtails corresponding to α eigenvalue is higher compared to the hyperbolic umbilics as the outer regions of the singularity maps show more swallowtails than umbilics. This also explains why we observed a larger number of images near swallowtails (corresponding to α eigenvalue) than hyperbolic umbilics. Here, we do not repeat that calculation and consider the earlier estimates as a lower limit.

Comparing the singularity maps of HFF clusters with each other, one can also see that not all cluster lenses contribute equally in the point singularity or arc cross-section. For example, we can see that A370 is roughly five times more efficient in producing image formation near a swallowtail or a cusp compared to MACS0416. The efficiency of other HFF clusters lies between MACS0416 and A370. Such a difference is also observed in the corresponding magnification maps (e.g., Johnson et al., 2014; Vega-Ferrero et al., 2019). However, one should keep in mind that the area in the source plane magnified by a factor $\mu \geq \mu_{th}$ has a significant contribution from the fold caustic. Hence, having a larger source plane area magnified by $\mu \geq \mu_{th}$ does not directly imply that the corresponding point singularity cross-section will also be higher. One can still use the magnification maps to get a qualitative idea about the arc and point singularity cross-section since large critical lines in the lens plane mean having more probability of a substructure introducing distortions in it and introducing extra cusps in the source plane. We would like to remind the reader that these inferences are based on specific models of HFF clusters, and these numbers can vary based on the reconstruction method

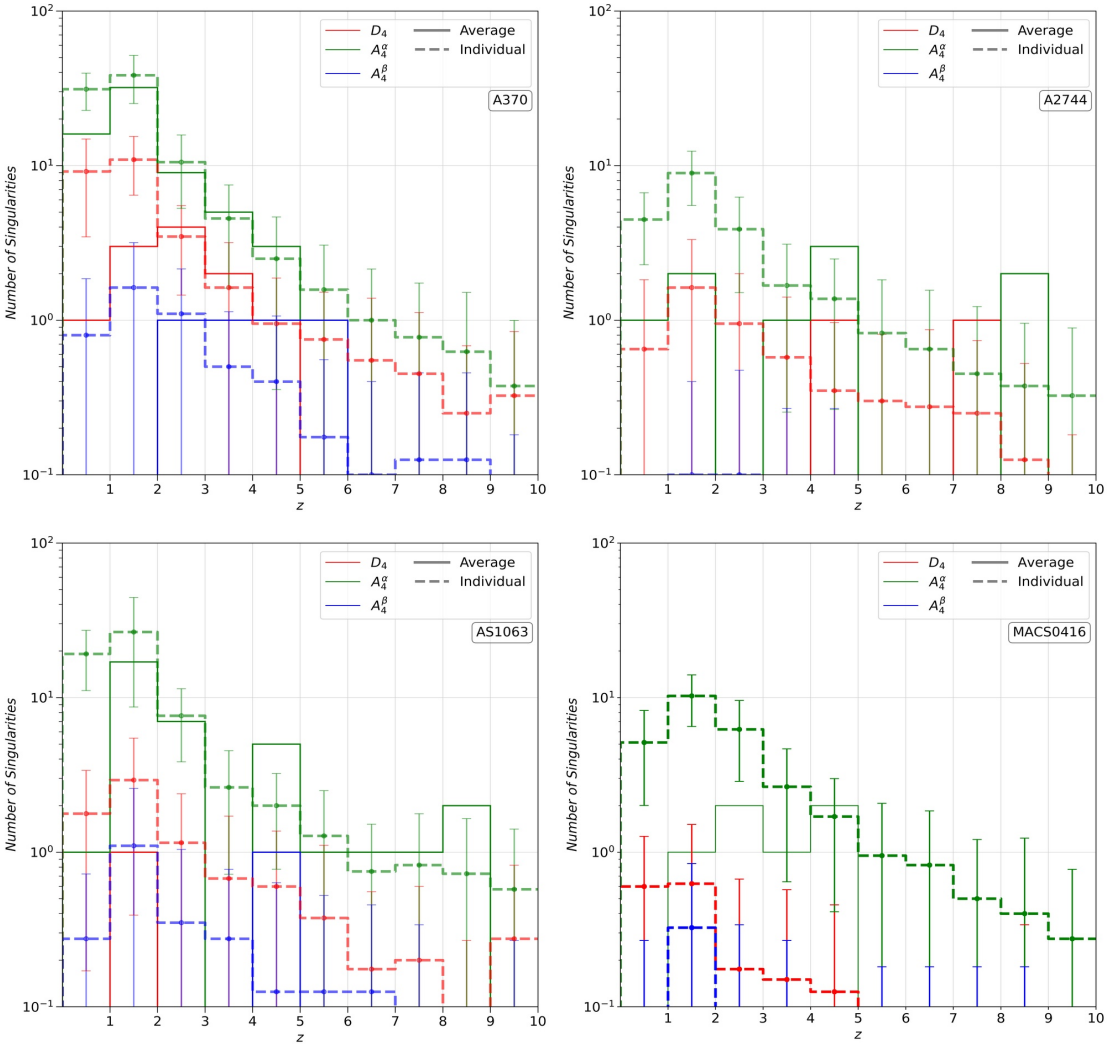

Figure 4.5: Number of singularities as a function of redshift in the HFF clusters: In each panel, the thin lines represent the number of singularities corresponding to the best-fit average mass model for the HFF clusters. The thick dashed lines show the average number of singularity in individual mass models for the HFF clusters. The error bars represent the corresponding one sigma scatter. The red lines represent the distribution of (hyperbolic+elliptic) umbilics. The green and blue lines represent the distribution of swallowtail singularities corresponding to α and β eigenvalues of the deformation tensor.

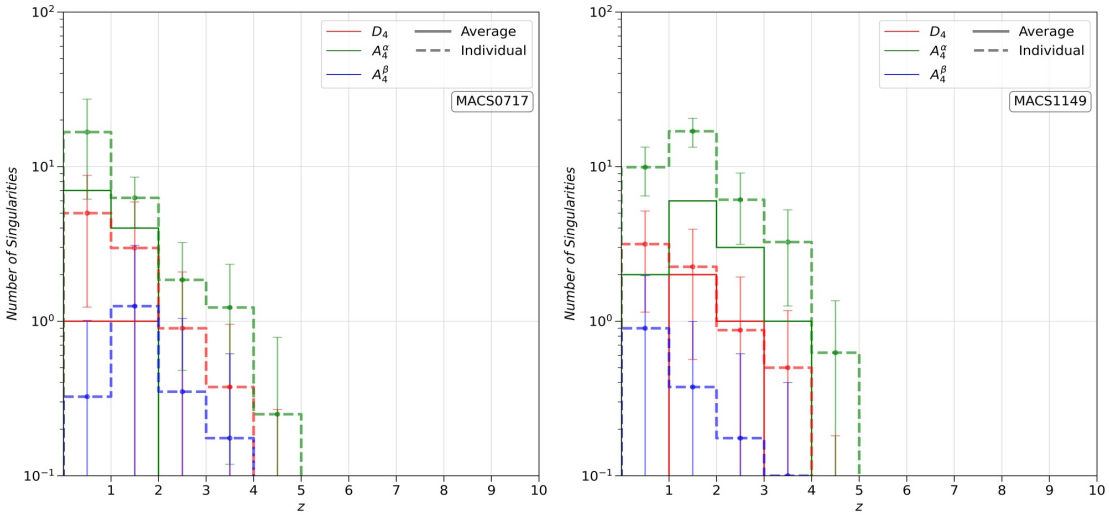

Figure 4.5: Cont.

used.

4.3.2 HFF Clusters: Redshift Distribution of Singularities

Unlike simulated clusters, we do not have the actual mass distribution of a real galaxy cluster. Hence, for HFF clusters, we compare the point singularities in the individual runs with the point singularities in the corresponding final best-fit mass models. The redshift distribution of point singularities in the HFF clusters is shown in Figure 4.5. In each panel, the red, green, and blue lines represent the number of (hyperbolic + elliptic) umbilics, the number of swallowtail singularity for α, and the number of swallowtail singularity for β eigenvalues, respectively. Here, we do not differentiate between hyperbolic and elliptic umbilics as the number of elliptic umbilics is negligible as compared to the hyperbolic umbilics. In each panel, the thin solid lines represent the number of point singularities corresponding to the averaged best-fit mass models, and the thick dotted lines represent the average number of point singularities in the individual runs. The errorbars associated with thick dotted lines represent the one-sigma scatter in the number of point singularities in the 40 realizations.

As with the simulated Irtysh clusters, the average number of point singularities in the individual runs is higher (more than one sigma difference in some clusters) compared to the best-fit mass models at redshifts $z < 2$. In Irtysh clusters, we expected to observe such discrepancy in the central regions of the clusters as there were no sources below redshift one that can provide lensed images near the central region in order to constrain it better. For A370 and AS1063, there are lensed images below redshift one, but we

still observe an excess of point singularities in the individual runs. Hence, we can say that introducing additional images below redshift one may help in decreasing the discrepancy in the central images. But we cannot be sure that it will always bring the numbers within one sigma error bars.

As we go towards higher source redshifts, the number of point singularities decreases in individual runs. However, the same cannot be said for the best-fit mass models. For example, in the case of A2744, there are some umbilics and swallowtails that are present even at very high source redshifts. Following the simulated Irtysh cluster, we may infer that these point singularities at very high redshift are spurious features. However, just by considering the Grale mass models, we cannot be sure about that as there are no reference mass models for the real cluster lenses. As the point singularities depend on the higher-order derivatives of the deformation tensor, taking inputs from the parametric reconstruction for validations of these features may not be very useful.

4.3.3 HFF Clusters: Arc Cross-Section

The A_3-lines constitute the backbone of a singularity map. These lines trace the points in the lens plane that correspond to cusps in the source plane. Hence, if we draw the critical curves for a given redshift on the top of the A_3-lines in the lens plane, then these critical curves cut the A_3-lines at the points that correspond to cusps in the source plane for that source redshift. As a result, without looking into the source plane, one can count (in a very simple way) the number of cusps on tangential and radial caustics in the source plane. Hence, using the A_3-lines and the critical curves, we easily calculate the (tangential and radial) arc cross-section for a given lens model with a given population of sources.

To calculate the arc cross-section, we divided the source redshift range [0.6, 10] in equal intervals of $\triangle z = 0.01$. After that, we draw the critical curves in the lens plane for each interval and calculate the number of points in the lens plane where a (tangential or radial) critical curve cuts the corresponding A_3-line. We assume that the number of such points is constant in the respective redshift interval of $\triangle z = 0.01$. Similar to point singularities in paper II, we consider an area of 5 kpc in the source plane and calculate the number of source galaxies with the image formation near the cusp points. This method will underestimate the number of cusp points if two A_3-lines are very near to each other. Such a scenario occurs when a swallowtail singularity gets critical, and two cusps emerge in the source plane. However, the underestimation is not significant as the singularity maps for non-parametric models are not very complex.

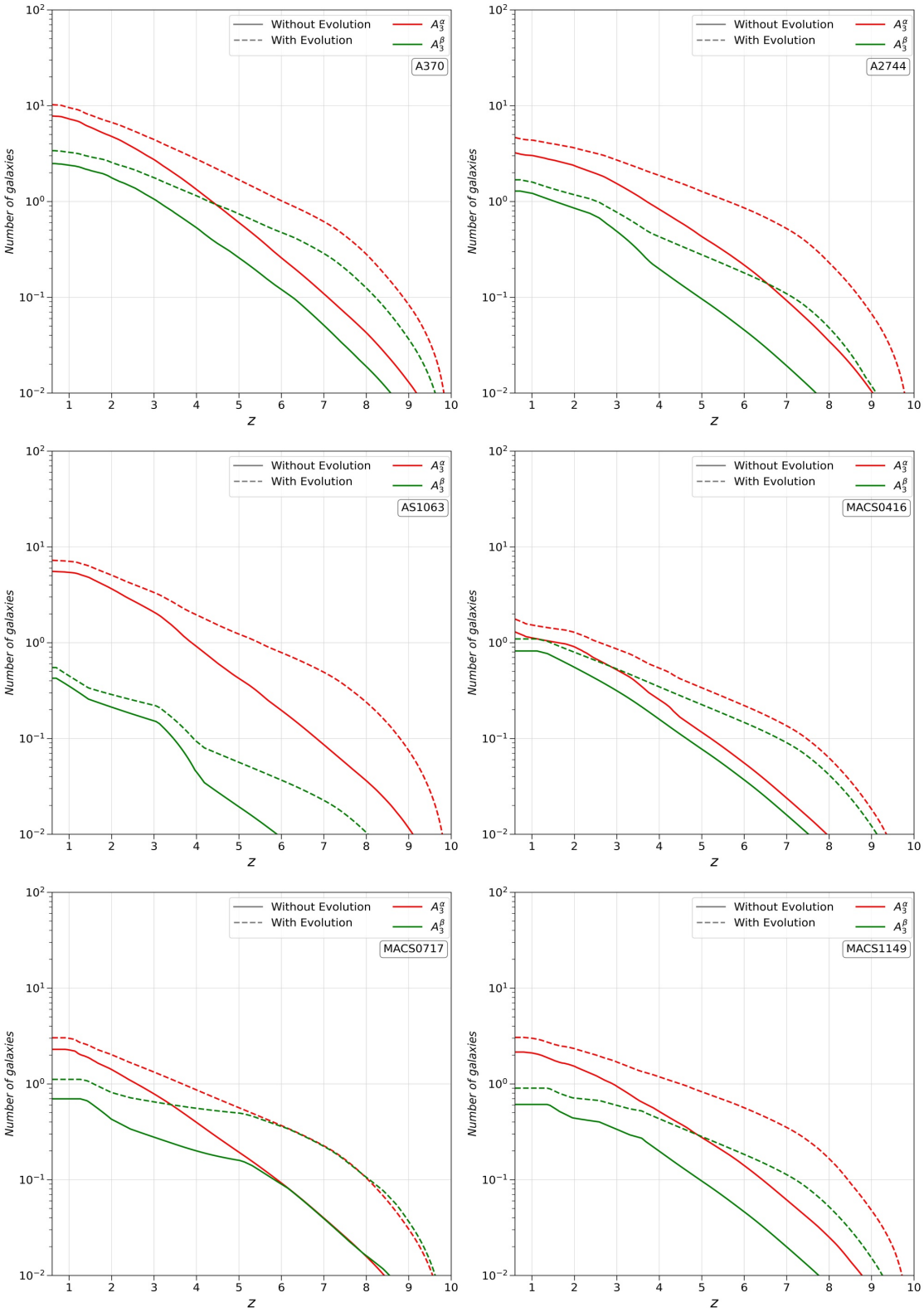

Figure 4.6: The cumulative number of source galaxies near the (tangential and radial) cusps as a function of redshift for HFF cluster lenses: the y-axis shows the number at redshifts higher than z. The solid (dashed) lines represent the galaxy numbers calculated using the fiducial (evolving feedback) model used in C18. The red and green lines denote the cumulative galaxy numbers corresponding to the tangential and radial cusps (corresponding to α and β eigenvalues of the deformation tensor).

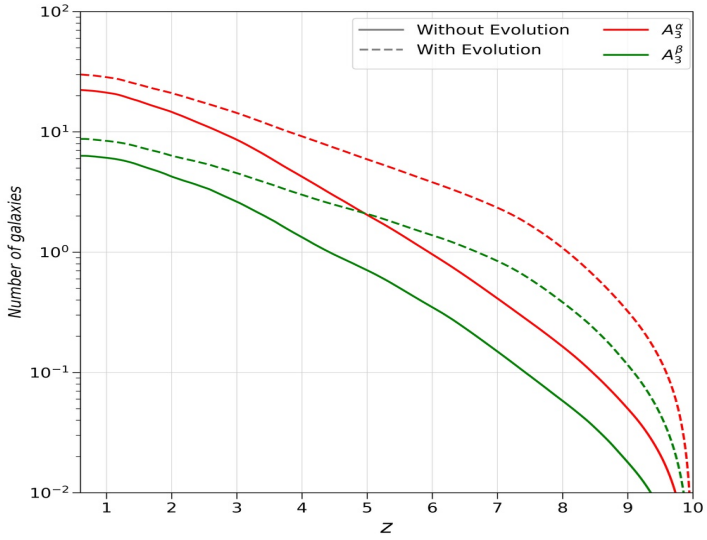

Figure 4.7: The total cumulative number of the source galaxies near tangential and radial cusps as a function of redshift for the HFF clusters: The y-axis shows the number at redshifts higher than z. Similar to Figure 4.6, the solid lines represent the galaxy numbers calculated using the fiducial model used in C18, whereas the dashed lines indicate the galaxy numbers calculated using the model with evolving feedback. The red and green lines denote the cumulative galaxy numbers corresponding to the tangential and radial cusps (corresponding to α and β eigenvalues of the deformation tensor).

Following this method, we calculated the cusp cross-section for HFF clusters. The galaxy source population is taken from C18 for one filter (F200W) of the JWST. The results are shown in Figure 4.6. The x-axis represents the source redshift, and the y-axis shows the number of source galaxies that are expected to give the image formation near cusps in the source plane higher than redshift z. The red and green lines represent the number of source galaxies near the tangential and radial arcs in the source plane. In each panel, the cross-section is plotted considering sources in the redshift range [0.6, 10]. These cross-section plots again validate our inference from the singularity maps (in Section 4.3.1) that A370 is most efficient in producing the tangential and radial arcs among the HFF clusters. The cumulative arc cross-section for all clusters is shown in Figure 4.7. From our analysis, we expect to observe at least 10-20 tangential and 5-10 radial three image arcs with the JWST. Again, as the Grale mass models have a very small contribution from galaxy scale substructures in the cluster lenses, these values should be considered as a lower limit.

4.4 Conclusions

In this work, we have studied the effect of statistical uncertainties associated with cluster lens mass reconstruction with Grale on point singularities. We considered two simulated clusters, Irtysh I and II from GWL20 and six galaxy clusters from the HFF survey. For both simulated and real galaxy clusters, the mass models were reconstructed using Grale. For each simulated galaxy cluster, we had three different mass models reconstructed with different sets of multiple images (please see GWL20 for more details). For each cluster lens, 40 reconstructions were done, and the best-fit mass models were the average of them. As a first step, we have constructed singularity maps for the original mass models (in the case of Irtysh I and II) for all of the individual mass models and the best-fit mass models. In the next step, we have compared the singularity maps corresponding to the individual realizations with the original and average best-fit mass models. These comparisons for simulated and HFF clusters are shown in Figure 4.3 and 4.5, respectively.

We find that the singularity maps corresponding to the best-fit mass models have a relatively small number of point singularities compared to the individual runs. As a result, the best-fit mass models provide a lower bound on the number of singularities that a lens has to offer. For mass models reconstructed by Grale, such a result is expected due to the fact that individual realizations contain spurious features, and the averaging to get the best-fit mass models is done in order to remove the contribution from these spurious features. Hence, the final best-fit mass model contains a low number of small scale structure and a low number of point singularities. The differences in the number of point singularities between individual runs and the best-fit are maximum at source redshift $z < 2$ for both simulated and real clusters. One can expect such discrepancy to arise at these redshifts as the mass models in the central regions of the clusters, at present, is not very well constrained. However, in order to be sure about this explanation, one will need to construct the mass models for simulated clusters with multiple images near the cluster center.

Such an averaging (over 40 realizations) to get the final best-fit mass model also simplifies the over A_3-line structures in the singularity maps. As A_3-lines in the singularity maps correspond to the number of cusps in the source plane at every source redshift, the final best-fit mass model also has a smaller number of cusps compared to individual realizations. Hence, the final best-fit mass models also provide a lower limit on the number of image formations near cusps. In our current work, we have also calculated the cusp cross-section for the HFF clusters using the best-fit mass models. We find that A370 is most efficient in producing three image arcs and the image formation

near point singularities among the HFF clusters based on Grale modeling. In the HFF clusters, one would expect to observe at least 10-20 tangential and 5-10 radial three image arcs with JWST.

The key takeaway from our current work is that the best-fit mass models constructed using the Grale provide the lower limit on the number of cusps and point singularities for a given cluster lens. Folding in the statistical uncertainties does not decrease the numbers obtained from the best-fit mass models. As shown in paper II, one would expect to observe at least one hyperbolic umbilic and one swallowtail for every five clusters with JWST even when we include the corresponding statistical uncertainties. Apart from that, one also expects at least 10-20 tangential and 5-10 radial three image arcs with JWST in the HFF clusters.

The above results are based on the non-parametric modeling by Grale, which underestimates the contribution from the galaxy scale substructures in the cluster lenses. Hence, if one considers parametric modeling, the above quoted numbers are expected to increase. Apart from that, in the HFF survey, there are only six cluster lenses. As shown above, these singularity maps also provide a very nice way to compare the efficiency of different cluster lenses. This feature can also be used to compare the simulated and real clusters on qualitative (visual comparison of singularity maps) and quantitative basis (arc and point singularity cross-sections).

Apart from that, image formation corresponding to arcs or point singularities shows three or more images lie in a very small region of the lens plane. Hence, the time delay between these images is expected to be small compared to other (typical) multiple image formation scenarios. The other important feature of point singularities is their characteristic image formation, which can be very helpful in locating them. These possibilities are the subject of our ongoing work.

4.5 Supplementary Material

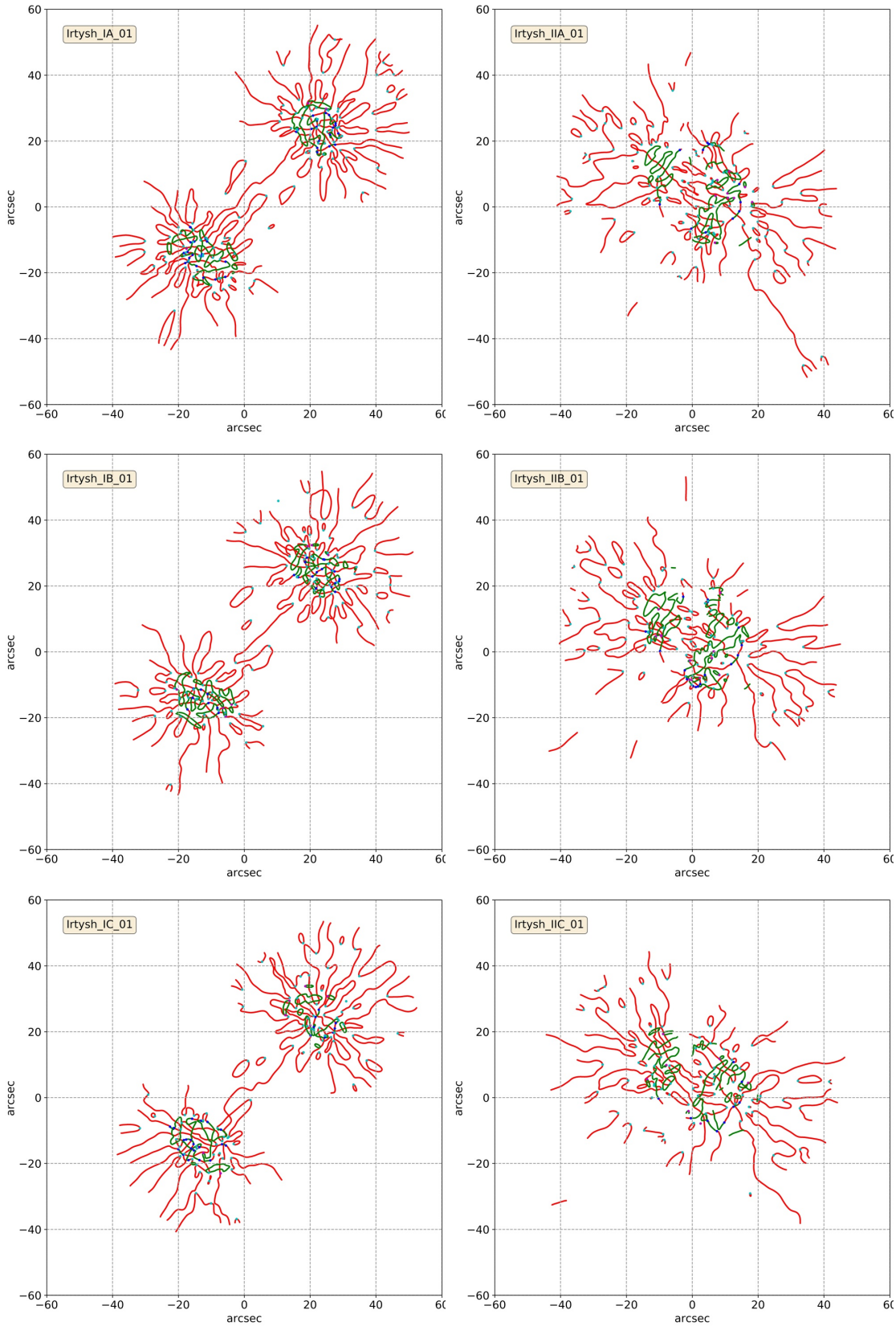

Figure 4.8: Every panel represents one singularity map for one realization for different Irtysh mass models. The name of the realization is written in the upper left corner. The red and green lines represent the A_3-lines corresponding to the α and β eigenvalues of the deformation tensor. The blue points represent the (hyperbolic and elliptic) umbilics. The cyan (magenta) points represent the swallowtail points corresponding to the α (β) eigenvalues of the deformation tensor.

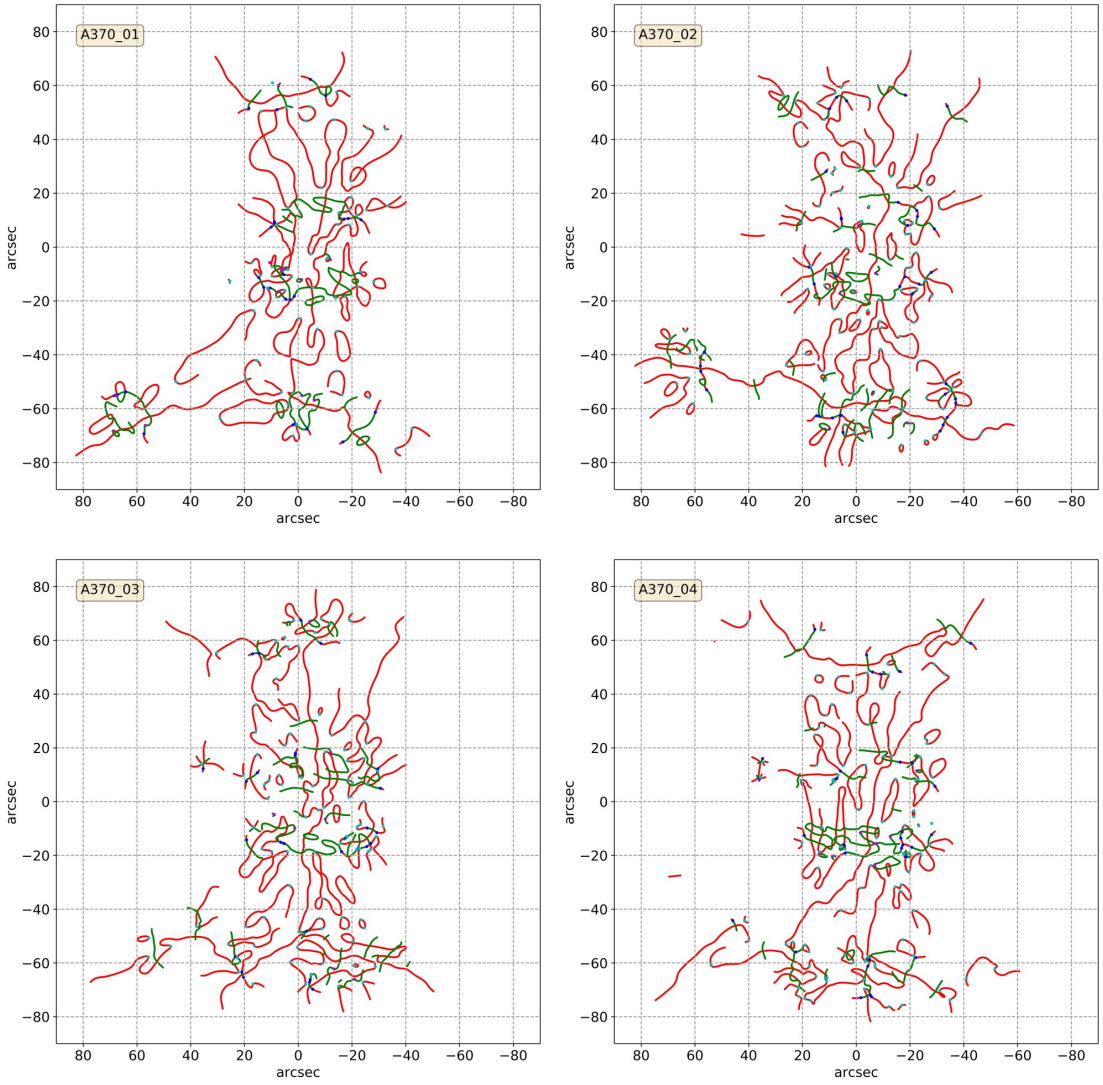

Figure 4.9: Singularity maps for individual runs of A370: Every panel represents one singularity map for one realization of A370. The name of the realization is written with the cluster name in the upper left corner. The red and green lines represent the A_3-lines corresponding to the α and β eigenvalues of the deformation tensor. The blue points represent the (hyperbolic and elliptic) umbilics. The cyan and magenta points represent the swallowtail singularities corresponding to the α and β eigenvalues of the deformation tensor.

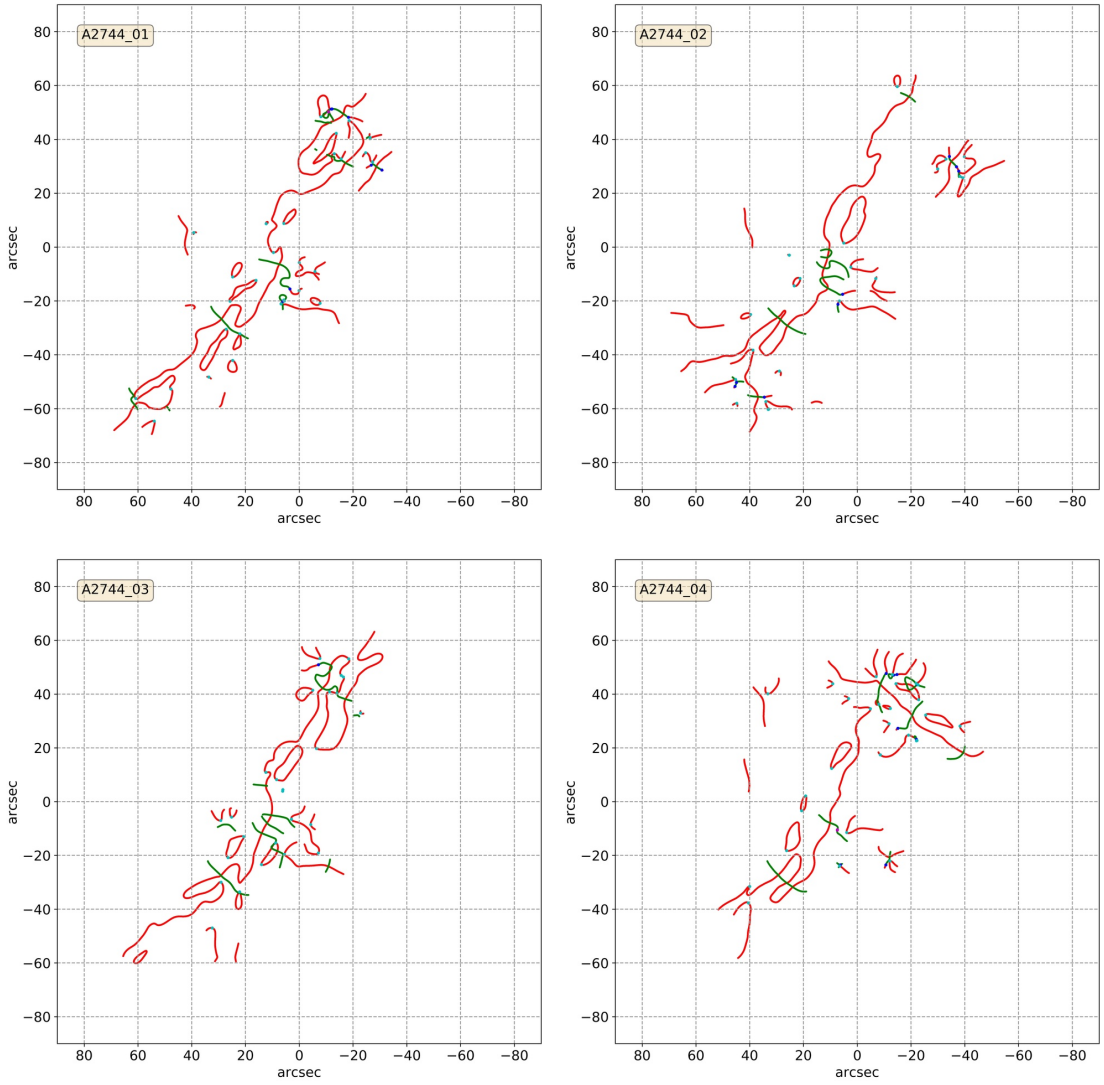

Figure 4.10: Singularity maps for individual runs of A2744: Every panel represents one singularity map for one realization of A2744. The name of the realization is written with the cluster name in the upper left corner. The red and green lines represent the A_3-lines corresponding to the α and β eigenvalues of the deformation tensor. The blue points represent the (hyperbolic and elliptic) umbilics. The cyan and magenta points represent the swallowtail singularities corresponding to the α and β eigenvalues of the deformation tensor.

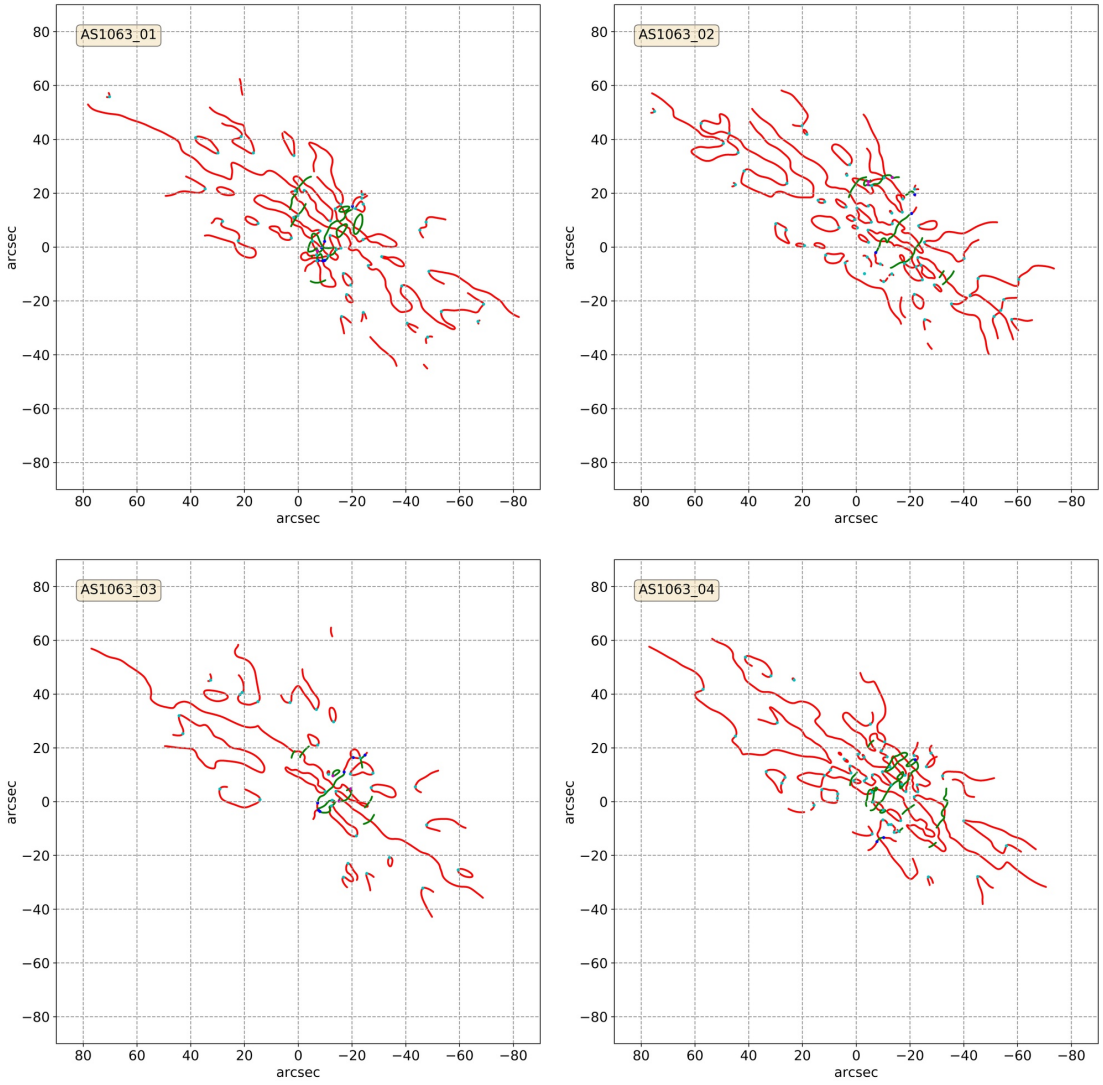

Figure 4.11: Singularity maps for individual runs of AS1063: Every panel represents one singularity map for one realization of AS1063. The name of the realization is written with the cluster name in the upper left corner. The red and green lines represent the A_3-lines corresponding to the α and β eigenvalues of the deformation tensor. The blue points represent the (hyperbolic and elliptic) umbilics. The cyan and magenta points represent the swallowtail singularities corresponding to the α and β eigenvalues of the deformation tensor.

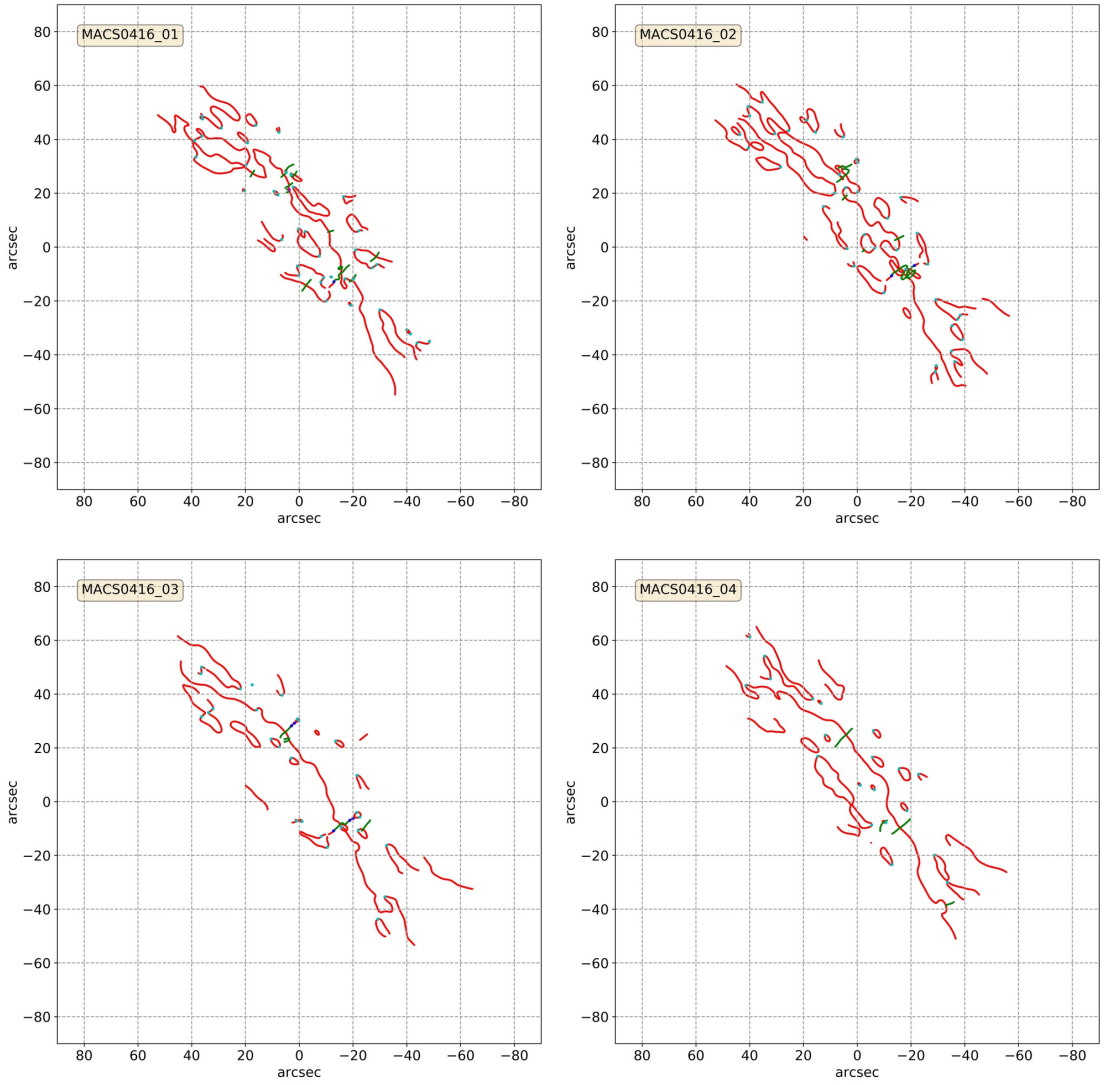

Figure 4.12: Singularity maps for individual runs of MACS0416: Every panel represents one singularity map for one realization of MACS0416. The name of the realization is written with the cluster name in the upper left corner. The red and green lines represent the A_3-lines corresponding to the α and β eigenvalues of the deformation tensor. The blue points represent the (hyperbolic and elliptic) umbilics. The cyan and magenta points represent the swallowtail singularities corresponding to the α and β eigenvalues of the deformation tensor.

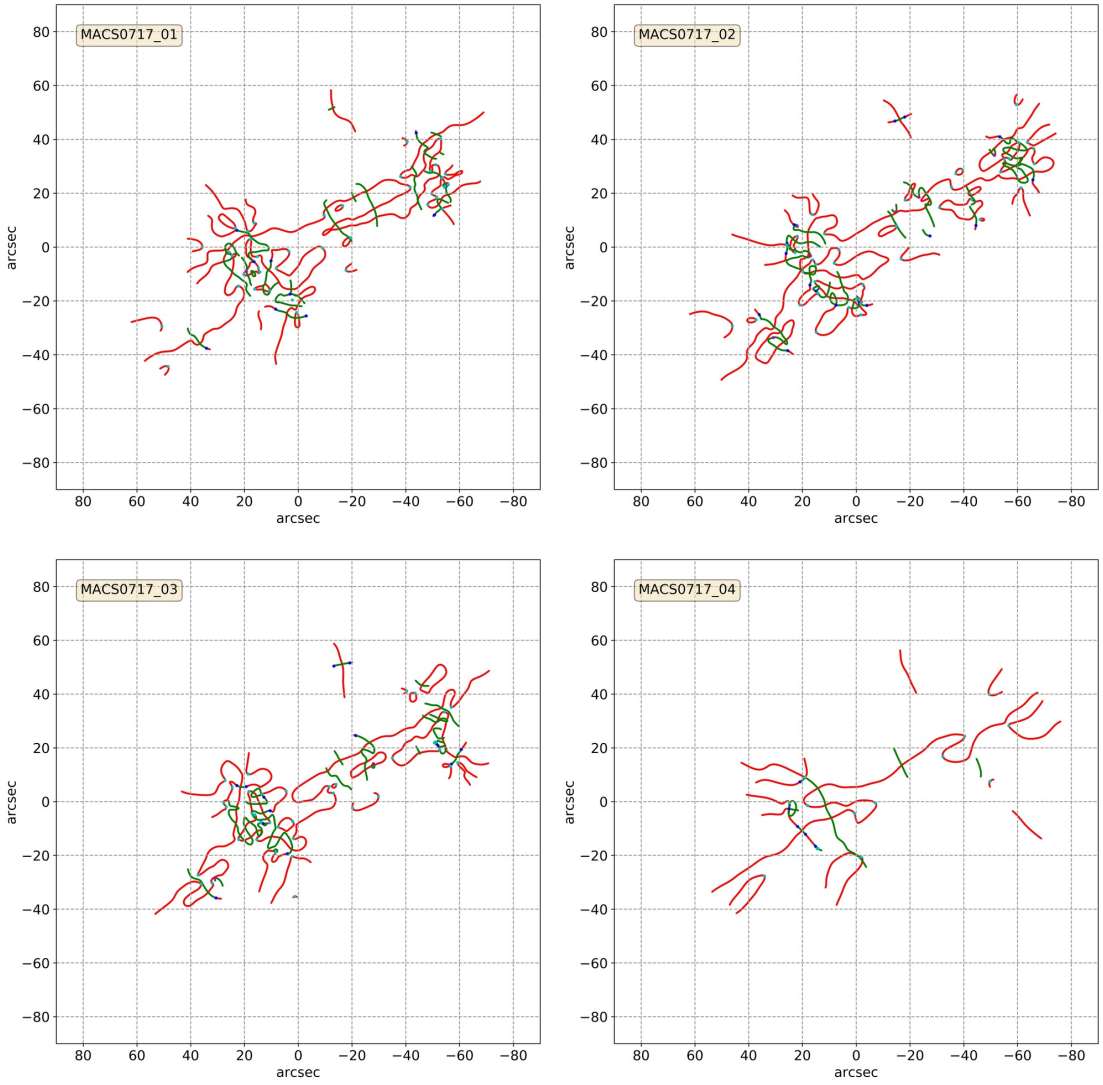

Figure 4.13: Singularity maps for individual runs of MACS0717: Every panel represents one singularity map for one realization of MACS0717. The name of the realization is written with the cluster name in the upper left corner. The red and green lines represent the A_3-lines corresponding to the α and β eigenvalues of the deformation tensor. The blue points represent the (hyperbolic and elliptic) umbilics. The cyan and magenta points represent the swallowtail singularities corresponding to the α and β eigenvalues of the deformation tensor.

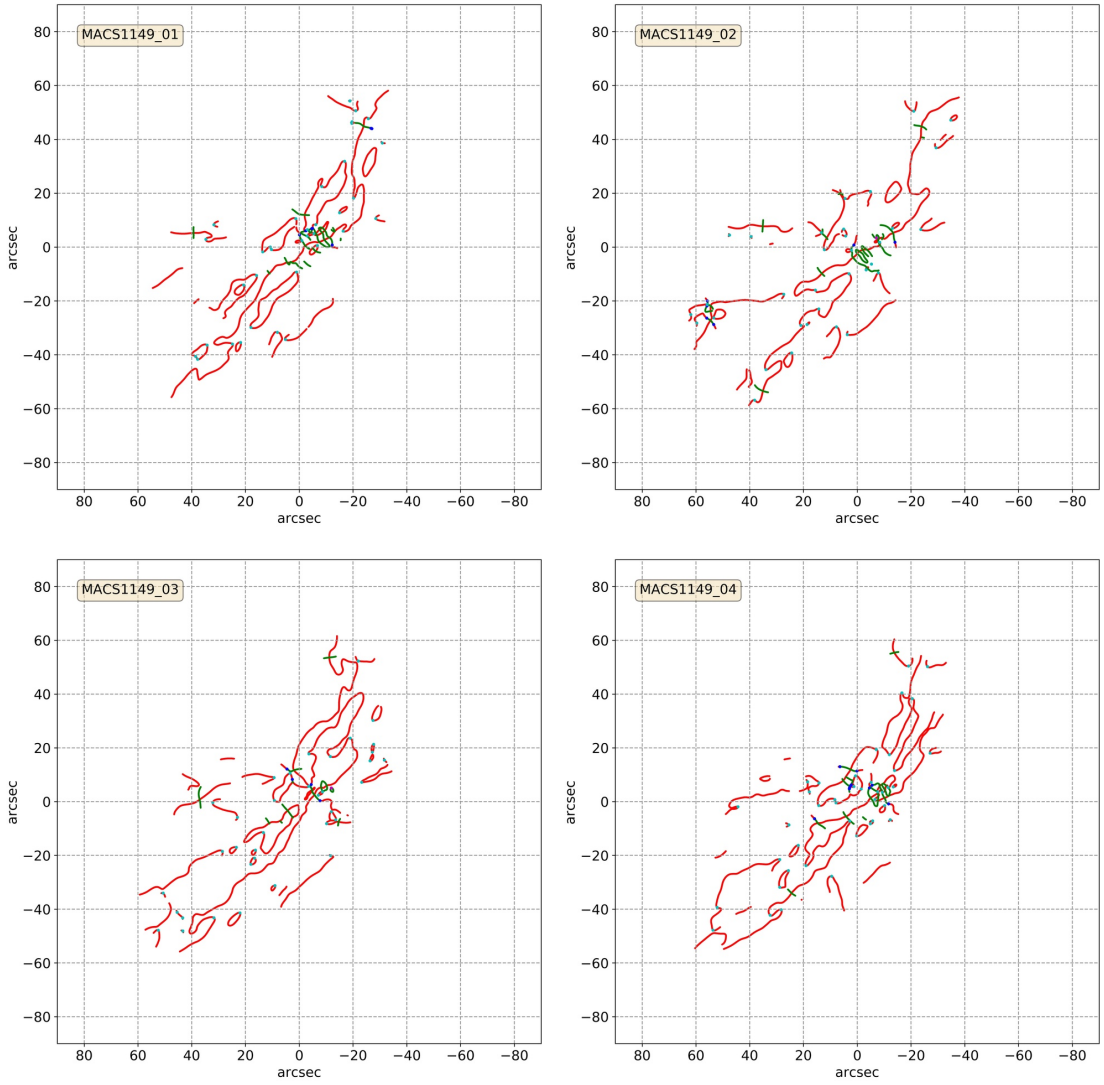

Figure 4.14: Singularity maps for individual runs of MACS1149: Every panel represents one singularity map for one realization of MACS1149. The name of the realization is written with the cluster name in the upper left corner. The red and green lines represent the A_3-lines corresponding to the α and β eigenvalues of the deformation tensor. The blue points represent the (hyperbolic and elliptic) umbilics. The cyan and magenta points represent the swallowtail singularities corresponding to the α and β eigenvalues of the deformation tensor.

Chapter 5

Gravitational Lensing of Gravitational Waves

This chapter is based on:

Meena, A. K., Bagla J. S., "Gravitational lensing of gravitational waves: wave nature and prospects for detection", **MNRAS**, 492, 1127 (2020).

5.1 Introduction

The recent detection of gravitational wave (GW) signal (Abbott et al., 2019) from coalescing binaries opens up a new window to observe the Universe (Rosswog, 2015; Wei & Wu, 2017). The upcoming runs of LIGO and Virgo with increased sensitivity and new detector facilities (Akutsu et al., 2018) will increase the number of observed GW signals significantly. As a result, the possibility of detecting a gravitationally lensed GW will also increase.

Propagation of gravitational waves is influenced by gravitational fields and results in a deflection in a manner similar to electromagnetic waves (Lawrence, 1971; Ohanian, 1974). In the typical cases of gravitational lensing of electromagnetic radiation, geometric optics is sufficient to study the effects of gravitational lensing as the sources have a finite size and the wavelength of the radiation is much smaller than all other scales of interest (Deguchi & Watson, 1986a; Schneider et al., 1992; Matsunaga & Yamamoto, 2006). Sources of gravitational waves are fairly compact and the wavelength of radiation that can be detected by existing and future detectors is larger than the region of emission. The wavelength of gravitational waves is comparable with the Schwarzschild

radius of many astronomical objects. Thus in the case of gravitational waves, the geometric optics is not always valid (Bontz & Haugan, 1981; Deguchi & Watson, 1986b; Nakamura, 1998; Baraldo et al., 1999; Christian et al., 2018). In LIGO frequency band (10Hz − 10kHz) for galaxy mass lenses geometric optics is sufficient (Varvella et al., 2004) as the wavelengths are much smaller than the size of a galaxy. Under geometric optics approximation, for galaxy mass lenses, the GW signal gets multiply imaged, and each signal is amplified by a constant factor $\sqrt{\mu}$, where μ is the corresponding strong lensing magnification. Although extra amplification can help us in observing events that are beyond LIGO range, the amplification factor is degenerate with the luminosity distance to the source and the chirp mass of the source which can introduce errors in the analysis (Broadhurst et al., 2018, 2019). If we can identify the multiple *images* in a lensed system then the time delay between these different signals can constrain the cosmological parameters (Sereno et al., 2011). The presence of small compact objects (micro-lenses) in the lens can further affect the signal. In this case, the wave nature can become important and hence, the effect of lensing is a combination of a wavelength dependent amplification factor as well as the phase of the signal (Diego et al., 2019).

In this work, we discuss the effects of micro-lensing in strongly lensed GW signal considering ideal microlens scenario. The effects of micro-lensing are non-negligible in the LIGO frequency band (Christian et al., 2018; Diego et al., 2019). As we shall see, these effects introduce frequency dependence in amplification as well as the phase of the lensed GW signal.

In section §5.2, we review the relevant basics of wave optics in gravitational lensing. Results are given in §5.3. Summary and conclusions are given in §5.4. We also discuss possibilities for future work in this section.

5.2 Basics of Gravitational Lensing

In this section, we review some aspects of wave effects in gravitational lensing, which is relevant for our analysis (Schneider et al., 1992; Nakamura & Deguchi, 1999; Takahashi & Nakamura, 2003). To describe the effect of the gravitational lens, one can consider a perturbed FRW as background metric, given by

$$ds^2 = -(1+2U)\,dt^2 + a^2(1-2U)\,d\mathbf{r}^2 = g^{(B)}_{\mu\nu}dx^\mu dx^\nu, \tag{5.1}$$

where U is the gravitational potential of the lens. The gravitational waves in this background are described as a tensor perturbation, $h_{\mu\nu}$. The linear perturbation can be

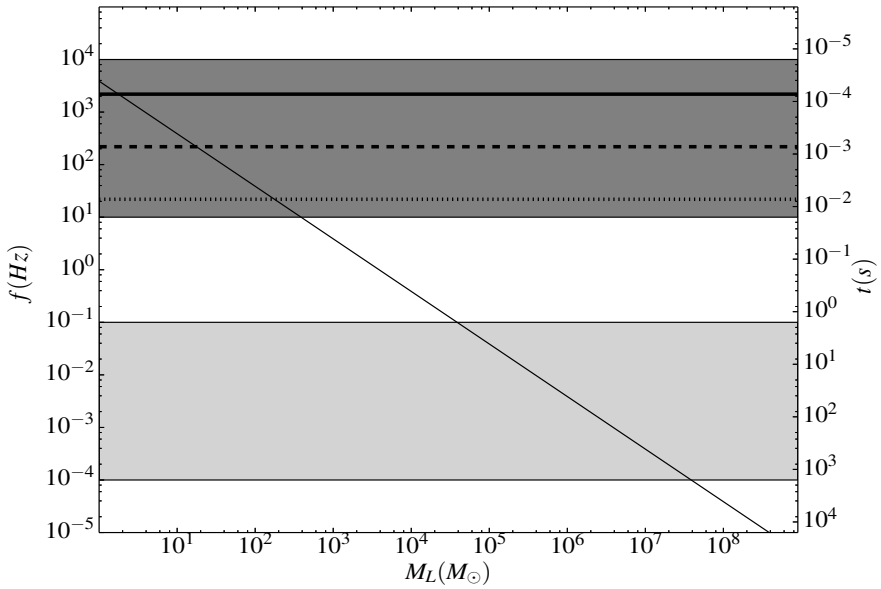

Figure 5.1: Lens mass versus gravitational wave frequency: The diagonal thin line from top left to bottom right represents the critical frequency below which wave effects are essential to calculate the lensing effects for a given point mass. The light and dark shaded regions represent the relevant frequencies for LISA and LIGO, respectively. The horizontal lines (dotted, dashed, thick solid line) represent the GW frequency at the innermost stable circular orbit (ISCO) emitted by the source binaries of masses, $100M_\odot + 100M_\odot$, $10M_\odot + 10M_\odot$, $1M_\odot + 1M_\odot$, respectively.

written as $\phi e_{\mu\nu}$; where ϕ represents the amplitude, and $e_{\mu\nu}$ is the polarization tensor of the gravitational wave. During propagation, the change in polarization tensor due to the presence of the lens is negligible (Takahashi & Nakamura, 2003; Misner et al., 1973). As a result, one can assume the polarization vector to be a constant. The propagation equation (to the leading order) for the scalar amplitude ϕ, in frequency domain is,

$$\left(\nabla^2 + \widetilde{\omega}^2\right)\widetilde{\phi} = 4\widetilde{\omega}^2 U\widetilde{\phi}, \tag{5.2}$$

where $\widetilde{\omega} = 2\pi f$, and f is the frequency of the gravitational wave. One can solve the equation (5.2) using Kirchhoff diffraction integral (Baraldo et al., 1999; Takahashi & Nakamura, 2003) for waves coming from a source at a distance D_S to the observer. Following Takahashi & Nakamura (2003), the amplification factor, $F(f)$ is defined as the ratio of lensed and unlensed $(U = 0)$ gravitational wave amplitudes $\widetilde{\phi}$. This implies that in no-lens limit $(U = 0)$, the amplification factor is unity $(|F| = 1)$.

In order to calculate the amplification factor, we need to solve the equation (5.2) for a given lens system. Under the thin lens approximation, for a gravitational wave source at a distance D_S and a lens at D_L, the amplification factor at the observer is given

by (Takahashi & Nakamura, 2003),

$$F(f,\mathbf{y}) = \frac{D_S \xi_0^2 (1+z_L)}{c D_L D_{LS}} \frac{f}{i} \int d^2\mathbf{x} \exp\left[2\pi i f t_d(\mathbf{x},\mathbf{y})\right], \tag{5.3}$$

where $\mathbf{x} = \xi/\xi_0$, $\mathbf{y} = \eta D_L/\xi_0 D_S$ are the dimensionless lens and source positions in the lens and source planes, respectively, ξ_0 is an arbitrary length scale, z_L is the lens redshift and t_d is the arrival time, given by

$$t_d(\mathbf{x},\mathbf{y}) = \frac{D_S \xi_0^2 (1+z_L)}{c D_{LS} D_S} \left[\frac{1}{2}|\mathbf{x}-\mathbf{y}|^2 - \psi(\mathbf{x}) + \phi_m(\mathbf{y})\right]. \tag{5.4}$$

The constant $\phi_m(\mathbf{y})$ does not depend on the lens properties and one can choose a form to simplify calculations. Here we choose $\phi_m(\mathbf{y})$ such that the value of time delay for minima image (image for which time delay is a global minimum) is zero: time delays for other points are measured with respect to this image. The phase of the amplification factor can be defined as, $\triangle\phi = -i \ln[F/|F|]$.

In the limit of geometric optics approximation ($f \gg t_d^{-1}$), the integral in equation (5.3) is a highly oscillatory function, and the amplification factor gets a significant contribution only from stationary points of the integrand. The form of amplification factor in geometric optics limit is

$$F(f,\mathbf{y}) = \sum_i \sqrt{|\mu_j|} \exp\left(2\pi i f t_{d,j} - i\pi n_j\right), \tag{5.5}$$

where $t_{d,j}$ is the value of time delay for j-th image, μ_j is the magnification of the j-th image and n_j is the Morse index with values 0, 1/2, 1 for images corresponding to minima, saddle and maxima of the time delay function, respectively (Takahashi & Nakamura, 2003). One can see that the lensed gravitational waveform corresponding to maxima (saddle) of the time delay has a phase difference of $e^{-i\pi}(e^{\frac{-i\pi}{2}})$ compared to the waveform corresponding to the minima of time delay (Dai & Venumadhav, 2017).

In order to find out the amplification factor for different lens models, we solve equation (5.3) numerically. However, for a point mass lens, the solution of equation (5.3) can be obtained analytically and is given in terms of the hyper-geometric function,

$$\begin{aligned} F(\omega,y) &= \exp\left[\frac{\pi\omega}{4} + \frac{i\omega}{2}\left\{\ln\left(\frac{\omega}{2}\right) - 2\phi_m(x_m)\right\}\right] \\ &\quad \Gamma\left(1-\frac{i\omega}{2}\right) {}_1F_1\left(\frac{i\omega}{2}, 1; \frac{i\omega}{2} y^2\right), \end{aligned} \tag{5.6}$$

where $\omega = 8\pi G(1+z_L) M_L f/c^3$, $\phi_m(\mathbf{y}) = (x_m - y)^2/2 - \ln x_m$ with $x_m = \left(y + \sqrt{y^2+4}\right)/2$.

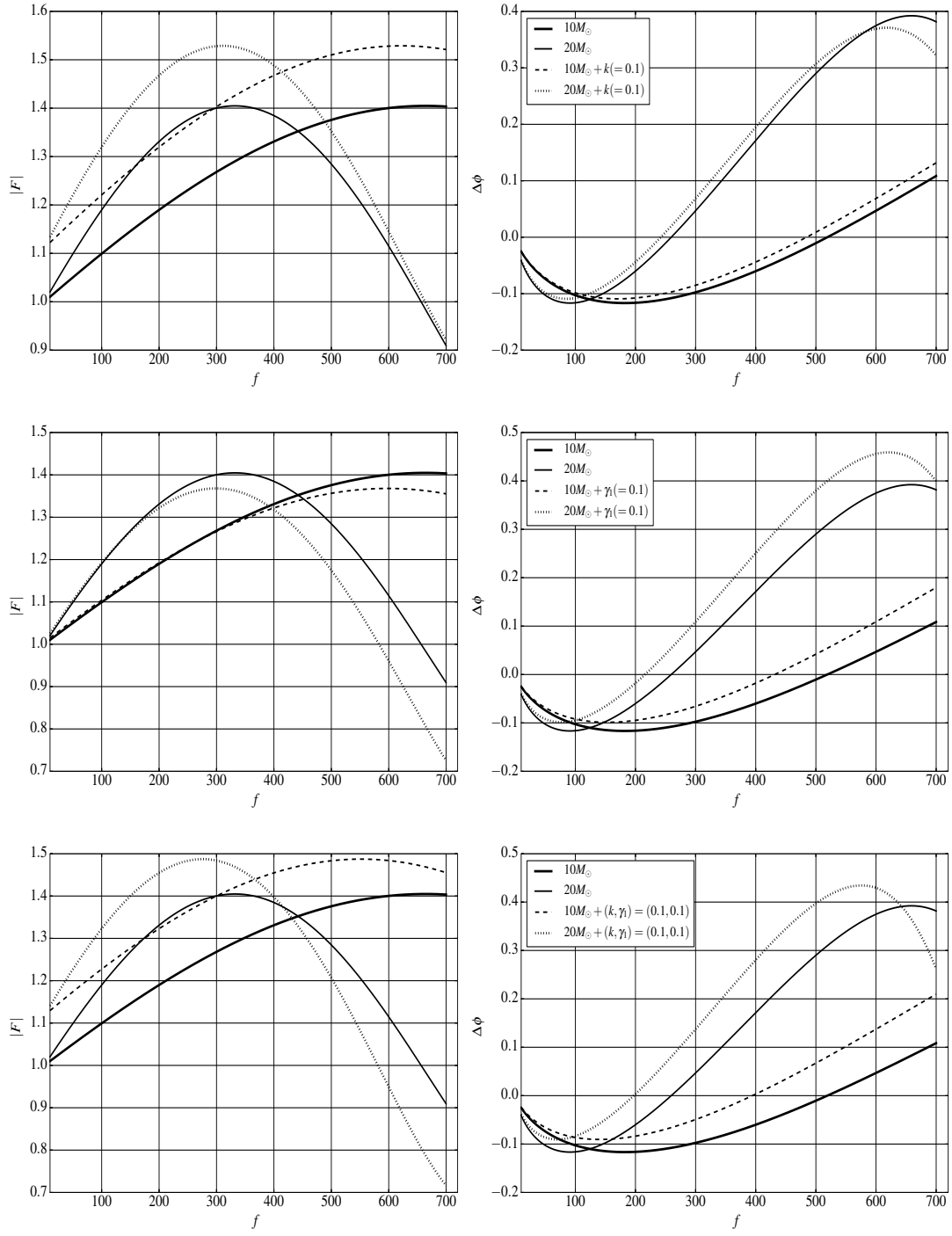

Figure 5.2: Micro-lensing within a strongly lensed image: The left column represents the amplification factor for two different micro-lenses within a strong lens represented by external shear and convergence. The right column shows the corresponding phase. For each row, the mass of the micro-lens and the values for external convergence and shear are mentioned in the right side of the respective row. The x-axis represents the frequency of gravitational waves in Hertz. The y-axis represents the amplification factor ($|F|$) and phase ($\triangle\phi$) in left and right panel, respectively.

Here we used Einstein radius corresponding to a point mass lens as the scale length $\xi_0 = \left(4GM_L D_L D_{LS}/c^2 D_S\right)^{1/2}$. Using geometric optics approximation ($\omega \gg 1$), the above equation reduces to,

$$F(\omega, y) = \sqrt{|\mu_+|} - i\sqrt{|\mu_-|}\exp\left[2\pi i f \triangle t_d\right], \tag{5.7}$$

where $\mu_\pm$, are the magnification factors for primary and secondary images for a point mass lens in geometric optics limit and $\triangle t_d$ is the time delay between these two images. One can see the oscillatory behavior of the amplification factor at higher frequencies. To get the conventional expression for amplification factor, we need to take a square followed by an average of equation (5.7). In our approach, we have assumed a point source for gravitational waves. A further refinement where we take the finite size of the emitting region can be made (Matsunaga & Yamamoto, 2006).

5.3 Results

In this section, we present the results of our study of gravitational lensing of gravitational waves emitted from a coalescing binary. For illustration, we neglect the role of eccentricity of the orbit. This section is further divided into subsections, considering different circumstances in which a gravitational wave can be affected by a gravitational lens.

5.3.1 Applicability of geometrical optics

In case of lensing of electromagnetic radiation, due to the small wavelength, use of geometric optics is adequate as corrections from the wave optics are negligible (Schneider et al., 1992). However, the wavelength of gravitational waves that can be detected with existing and future detectors is much larger and is comparable to the relevant scales of some gravitational lenses. Therefore, in order to discuss the lensing of gravitational waves, we need to ascertain whether wave effects are significant or not? We find that for wavelengths equal to or larger than the path difference between the multiple images of the source, one should use wave optics instead of geometric optics. Taking equation (5.3) into account, one can write the above condition in mathematical form as (Takahashi, 2017),

$$2\pi f t_d \lesssim 1, \tag{5.8}$$

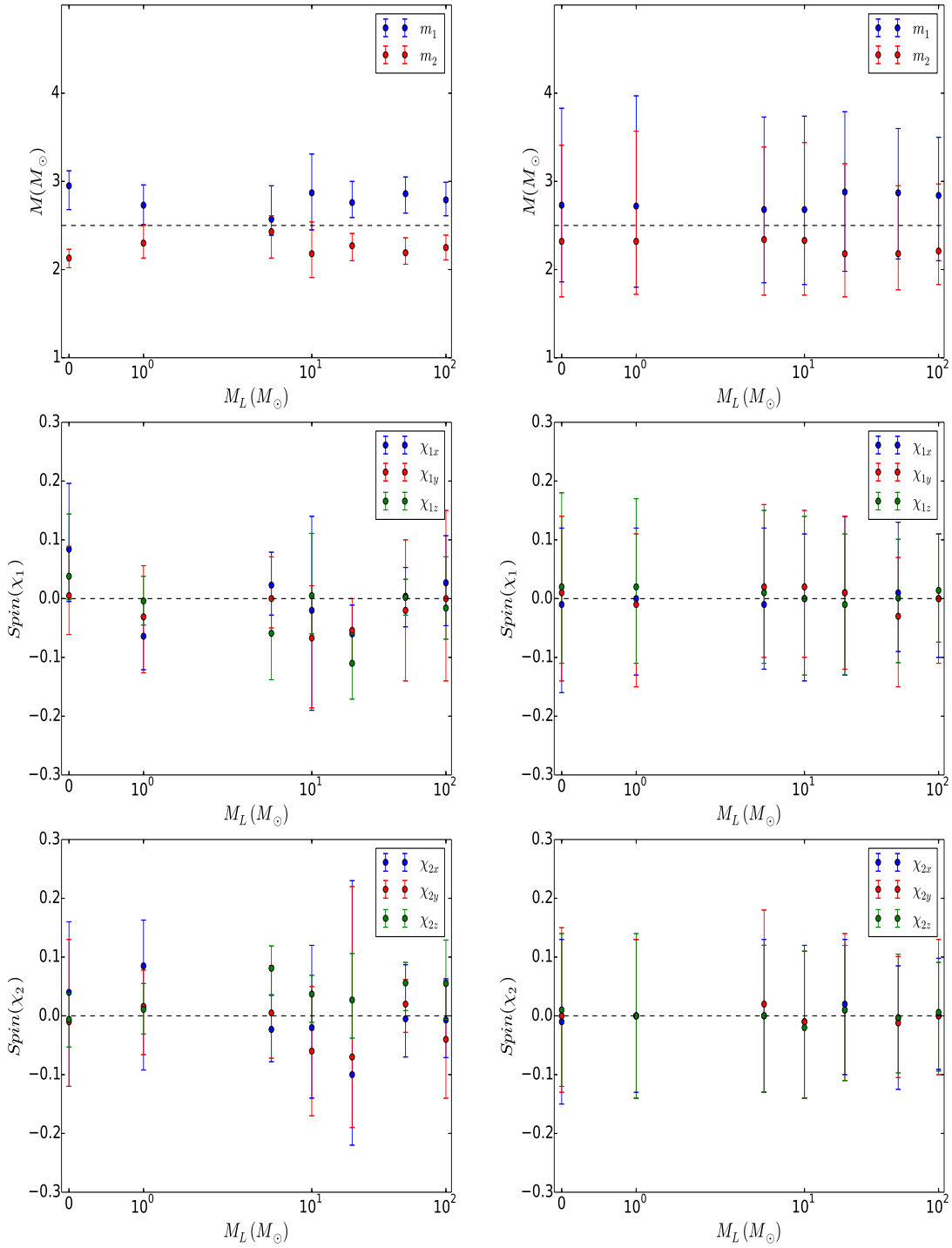

Figure 5.3: Parameter estimation of a lensed GW signal at high and small SNR values: The left column shows the parameter estimation for a GW signal at SNR value 34 (in unlensed case), whereas the right column shows the parameter estimation at SNR value 10 (in unlensed case). The x-axis represents the microlens mass. The y-axis represents the different parameter values. In different panels, the horizontal dotted line represents the input value of the corresponding parameters. The top row represents the mass estimation of binary components for different microlens values. The middle and bottom rows represent the spin component estimation for first and second binary components, respectively. The error bars show one sigma error in the estimation of different parameters.

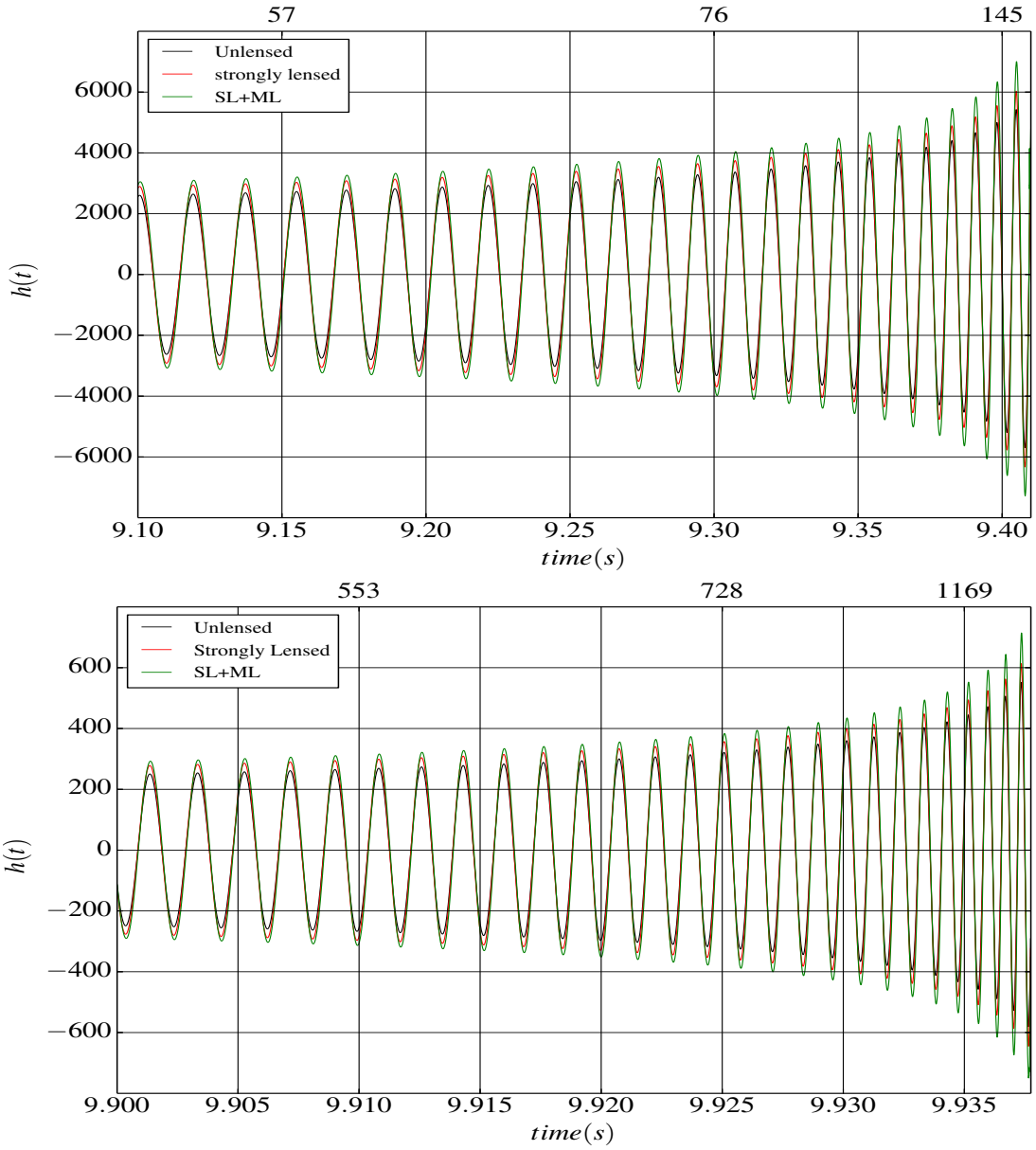

Figure 5.4: Cont.

where f is the frequency of the gravitational waves and t_d is the time delay between the images. Figure 5.1 shows the plot of the equation (5.8) for a point mass lens. The thin solid line denotes the condition $2\pi f t_d = 1$. Below this line, one should use the wave optics results as the wavelength of the gravitational waves is much larger than the path difference between the two images, which is of the order of the Schwarzschild radius of the lens. Above but near this line, the correction terms from diffraction effects continue to be non-negligible. As one moves away from this line, the correction terms due to diffraction effects become negligible, and finally one can use geometric optics if the wavelength of the gravitational wave is much smaller than the Schwarzschild radius of the lens. Geometric optics is a good approximation if we are a factor of at least a few above this line.

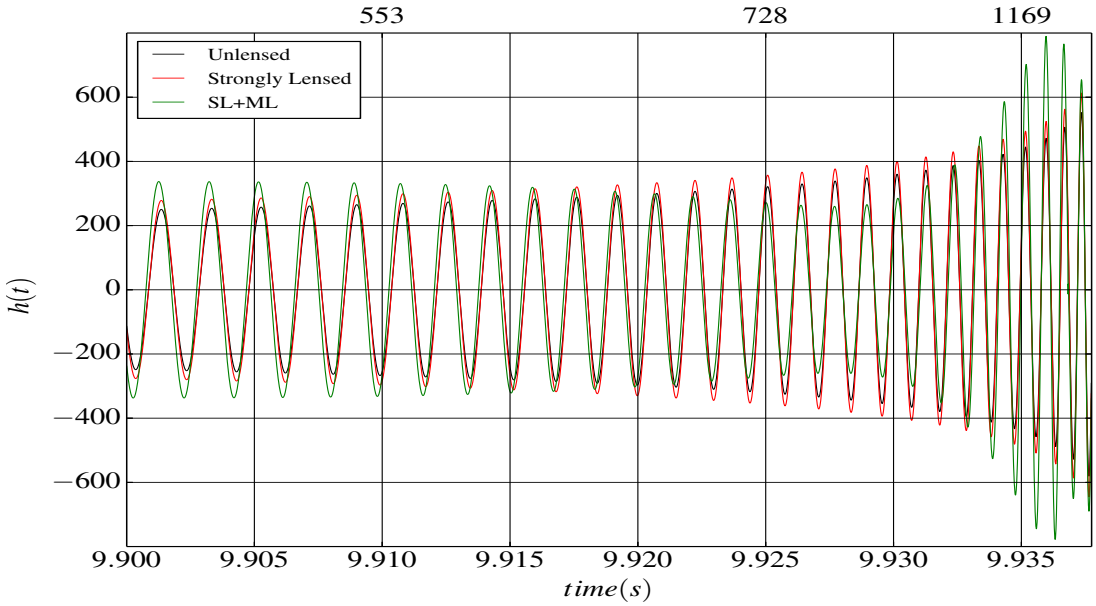

Figure 5.4: Effect of lensing on gravitational waveform in time domain. The top panel is for a 10 $M_\odot + 10\ M_\odot$ binary, the lower panels are for a 1 $M_\odot + 1\ M_\odot$ binary. The black curve shows unlensed signal, the red curve shows the effect of strong lensing (in the geometric limit), and the green curve shows the effect of micro-lensing in addition to strong lensing. The top panel includes micro-lensing by a 10 $M_\odot$ lens, the middle panel includes micro-lensing by a 1 $M_\odot$ lens, and the lowest panel includes micro-lensing by a 20 $M_\odot$ lens. In each panel the x−axis shows the time, the corresponding frequency of gravitational waves is marked on the top of each panel. Each panel shows the gravitational wave amplitude as a function of time (and frequency). The unlensed signal is amplified uniformly by strong lensing, independent of frequency. However, the inclusion of micro-lensing brings in the frequency dependence in the amplification where the amplitude of the signal gets amplified more at some frequencies. This can be seen in all the rows but it is seen most dramatically in the lowest row where this introduces a strong modulation. Such modulation is seen if we cover a wider range of frequencies, i.e., if the signal is from a lower mass source, or if the micro-lens is much more massive than a sun like star. There is also a frequency dependent phase shift that is obvious from lowest panel and can be read off in right panels of Figure 5.2.

The light and dark shaded regions represent the frequency ranges covered by LISA and LIGO, respectively. The horizontal lines (dotted, dashed, thick solid line) represent the frequency of the gravitational waves at the innermost stable circular orbit (ISCO) emitted by the source binaries of masses, $100M_\odot + 100M_\odot$, $10M_\odot + 10M_\odot$, $1M_\odot + 1M_\odot$, respectively. For the purpose of illustration, we have neglected the effects of eccentricity and post-Newtonian corrections while computing the relevant frequency. The corresponding time delay is shown in the right side of the plot. One can see that for most of the relevant sources, the frequency of gravitational waves at ISCO lies in the LIGO band and the wave effects are only important in case of a micro-lensing scenario (Christian et al., 2018).

The frequency dependent amplification and phase shift leads to chromatic effects and this is the key signature of wave effects. These effects modify the waveform from coalescing binaries as the frequency keeps on increasing with time in the signal. The changes can be large enough to lead to mis-identification of source properties. Christian et al. (2018) have shown that disentangling the effects of micro-lensing is feasible for detections with a high signal to noise ratio ($SNR \geq 30$).

5.3.2 Micro-lensing Effects

The possibility of strong lensing of gravitational waves gives us the opportunity to observe the same source more than once due to the nonzero time delays (Piórkowska et al., 2013; Smith et al., 2018; Li et al., 2018; Haris et al., 2018; Hannuksela et al., 2019). In general, these different signals have different constant amplification factor, depending on the geometry of the lensing system. However, as we know smaller mass compact objects (stars, stellar remnants, black holes) are a part of galaxies and can further affect the gravitational wave signal via micro-lensing. The lensing due to these micro-lenses can also help us in observing intermediate mass black holes (IMBH) (Lai et al., 2018). As mentioned above, in LIGO frequency range, only micro-lensing ($M_{lens} \leq 10^3$ $M_\odot$) can give rise to the significant frequency dependent effects.

For simplicity, we only consider a single object as a potential micro-lens. In order to calculate the effect of micro-lensing, we choose the object to be located at the origin. The effect of the galaxy as a whole does not vary significantly over the relevant length scale of a star. As a result, the effect of the galaxy can be describe in terms of constant external convergence (κ') and constant shear (γ_1', γ_2'). Due to the presence of external effects, the resultant lensing potential of the star will be modified and can be written as (Schneider et al., 1992):

$$\begin{aligned} \psi(x_1,x_2) &= \ln\left(\sqrt{x_1^2+x_2^2}\right) + \frac{\kappa'}{2}\left(x_1^2+x_2^2\right) \\ &\quad + \frac{\gamma_1'}{2}\left(x_1^2-x_2^2\right) + \gamma_2' x_1 x_2. \end{aligned} \tag{5.9}$$

Using equation (5.3) and (5.9), we can calculate the effect of the star on the amplification factor as well as the phase of the gravitational wave signal.

Here we show results for three different possibilities: non-zero convergence, non-zero shear, and non-zero convergence and shear for a lens at redshift $z = 0.05$ and the source positioned at $(y_1, y_2) = (1, 0)$ at redshift $z = 0.2$. The mass of the micro-lens is fixed to $10M_\odot$ and $20M_\odot$. As one can see from Figure 5.2, the non-zero value of

convergence (shear) introduces a frequency dependence in the amplification factor as well as in the phase (these would have been independent of frequency in the absence of micro-lensing). Further, this frequency dependence is highly sensitive to the lens parameters $(M, \kappa, \gamma_1, \gamma_2)$. For example, if we change the mass on the micro-lens from $10M_\odot$ to $20M_\odot$, the amplification and phase pattern show significant changes. Similarly, if we consider a different combination of $(\kappa, \gamma_1, \gamma_2)$ which is equivalent to shifting the position of the micro-lens, the amplification pattern changes (see Figure 5.2). The effect on the chirp signal from coalescing binaries is to modulate the amplitude as we have a frequency dependent amplification, and also to introduce time varying phase shifts.

The effect of these oscillations on parameter estimation is shown in Figure 5.3. We have considered the effect of the microlens and ignored the effect of the strong lens galaxy as that does not introduce any frequency dependent variations in the signal. The left and the right column represent the parameter estimation of different binary parameters for a 2.5 $M_\odot$ + 2.5 $M_\odot$ binary for different SNR values. The SNR value in the left column is 34 for the unlensed signal, whereas the SNR value in the right column is 10 for the unlensed signal. These cover a reasonable range in SNR and give us a glimpse of what to expect. Here we used PyCBC for parameter estimation (Biwer et al., 2019). As one can see in the right column of Figure 5.3, at small SNR values ($\sim$10), the estimated values of various binary parameters do not differ significantly within one sigma errors. However, if the SNR value is larger than 30, then the microlensing effects on the parameter estimation can be distinguished within one sigma errors. Hence, the effect of microlensing is to modify the estimated values of binary parameters. This can be seen in the middle and bottom panel of the left column of Figure 5.3, where a non-zero spin is estimated even though the input spin is zero. It is interesting to note that the extent of the allowed region remains similar to the case of no micro-lensing (marked by 0 on the x-axis) but the allowed region moves around with variation in the microlens mass. These modifications can be more significant if we also take into account the impact of the host galaxy as the effect of the host galaxy can further increase the SNR value (Figure 5.2).

This introduces a severe problem in identifying different counterparts of a strongly lensed GW signal as the micro-lensing can introduce a different type of frequency dependence in different images.

Keeping source properties the same, if we explore the effects with changes in the mass of the micro-lens, we find that the form of variation of amplification and phase shift with frequency is monotonic in the LIGO range for micro-lenses with a smaller mass ($\sim M_\odot$), whereas it undergoes oscillations for a larger mass ($> 10^2 M_\odot$). This is to

be expected as with larger masses we gradually approach the geometric limit.

For better visualization, Figure 5.4 represents the lensed waveform in the time domain. We show the expected signal in the final moments before coalescence for three cases. We see here that for the low mass binary, we can probe gravitational waves of a higher frequency and hence, we are able to see the effect of oscillation in amplification. No such feature is seen in the signal from the higher mass binary as it does not reach higher frequencies. However, a frequency dependent amplification is seen in all cases. There is a frequency dependent phase shift that is not obvious from these figures but which is large enough to mislead in the mapping from the signal to the source parameters. As micro-lensing does not affect each sight line in the same manner, a comparison of the red and the green color waveform in bottom panel of Figure 5.4 is a representation of the differences that we may encounter due to this effect. It is clear from here that it may be difficult to identify signal from different strongly lensed images as coming from the same source due to the variations introduced by micro-lensing.

The probability of a micro-lensing event depends on many factors but it is not small. We are doing a detailed estimation but a preliminary analysis suggests that a few percent of the images are likely to be affected by micro-lensing. This order of magnitude analysis is done for an elliptical galaxy acting as a gravitational lens with de Vaucouleurs profile along with the Salpeter initial mass function. The average microlensing event rate for such a galaxy lens is of the order of 10^{-2}. If we specifically consider the microlensing near half-light radius, then the value of optical depth is larger than the average value: this is perhaps more relevant as the impact parameter in most cases is of this order or smaller. Similarly, if we consider microlensing due to an edge-on spiral galaxy, then the probability of microlensing can further rise as the projected density of the microlenses within the disk is much higher. On the other hand, the probability for microlensing for off-plane images is much lower in this case.

5.4 Conclusions

We have described the effects of micro-lensing alone and in case of a strongly lensed GW signal. As shown above, micro-lensing is the only way in which lensed signal in LIGO frequency band can get frequency dependent effects. The micro-lens may reside in our galaxy or it may be embedded in a bigger lens, e.g., an intervening galaxy. The effects of micro-lensing depend strongly on the lens parameters. For large values of SNR (> 30), as we change any of the lens parameters, the variation of amplification and phase with frequency changes significantly. Because of the possibility that differ-

ent counterparts of strongly lensed GW signal can get affected differently by micro-lensing, or only one image may be affected significantly, it introduces a real challenge in identifying the counterparts of the strongly lensed GW signal. The other difficulty in identifying the different counterparts of a strongly lensed GW signal is the poor localization of the GW signal. However, this identification can be possible if SNR is large enough (more than about 30) but most detections fall below this threshold. Apart from that, if the magnification factor due to the strong lens is large, then the possibility of microlensing is unavoidable. In such a case, even a few solar mass microlens can introduce significant distortions in the observed GW signal (Diego et al., 2019).

The challenge can be turned into an opportunity if a counterpart is observed in the electromagnetic radiation as this may permit better localization and identification of the images. In such cases, we can recover information about the wave effects and parameters of the micro-lens. Here, the sensitivity of the amplification and phase difference to parameters of the lens are useful features. In addition, time delay measurements with optical counterparts can be used to infer a lot of information about the lens and cosmological parameters (Piórkowska et al., 2013; Hongsheng & Xilong, 2018).

Gravitational lensing in the LISA band by much heavier lenses retains effects of the wave nature and hence it should be possible to detect these (Liao et al., 2019). However, lens masses required are in a range where few potential lens candidates are available. We propose that super massive black holes in intervening galaxies may produce effects that can be tracked in the LISA band. Observations here are sensitive to the mergers of very massive black holes, or to other coalescing binaries at epochs much before the final merger. In the latter case, superposition of signals with different time delays can produce modulation effects (Takahashi & Nakamura, 2003; Sereno et al., 2010).

Micro-lensing can affect gravitational waves from distant sources even in the absence of strong lensing. This may happen due to a lens in an intervening galaxy or a lens in the Galaxy. The probability for this to happen is small in most directions but is relatively (Wood & Mao, 2005) very high in the galactic plane region. Given that this can affect signal from sources in more than 10% of the sky with a high probability, effects of micro-lensing need to be taken into account seriously. It has been shown (Christian et al., 2018) that for detections with a high SNR, it is possible to disentangle the micro-lensing effects and source parameter determination. However, it is important that for other events we budget for the uncertainty that is introduced because of the likelihood of micro-lensing.

Chapter 6

Summary and Future Work

In this thesis, we have studied the point singularities (swallowtail, hyperbolic umbilic, and elliptic umbilic) in gravitational lensing. In addition, we also studied the effect of strong and micro-lensing on gravitational wave signals.

In Chapter 2, we have discussed the algorithm that we developed to locate these point singularities and validated it in the case of ideal and actual lenses. The end product of this algorithm is a singularity map comprising all the point singularities and A_3-lines. These A_3-lines denote the points in the lens plane, which correspond to the cusps in the source plane. In Chapter 3, we applied our algorithm in the case of ten different cluster lenses from the Hubble Frontier Fields (HFF) Survey and Reionization Lensing Cluster Survey (RELICS) and constructed the corresponding singularity maps. For each cluster lens from the HFF survey, we have constructed four different singularity maps corresponding to mass models provided by different teams. In this work, we also calculated the point singularity cross-section for the James Webb Space Telescope (JWST) in filter F200W. In Chapter 4, we studied the effect of uncertainties associated with the mass models on the singularity maps. For this purpose, we have considered simulated and HFF cluster lenses. We showed that the cross-section estimations presented in Chapter 3 are the lower limit and one expect to observe at least one swallowtail and one hyperbolic umbilic in every five clusters. Here, we also estimated the cusp cross-section for HFF clusters. We find that we expect to observe at least 20-30 tangential and 5-10 radial three-image arcs in the Hubble Frontier Fields cluster lenses with the JWST.

In chapter 5, we investigated the effect of microlenses on the strongly lensed gravitational wave signal in ideal lensing scenarios. We find that micro-lensing combined with strong lensing can introduce a time-varying phase shift in the signal and hence can

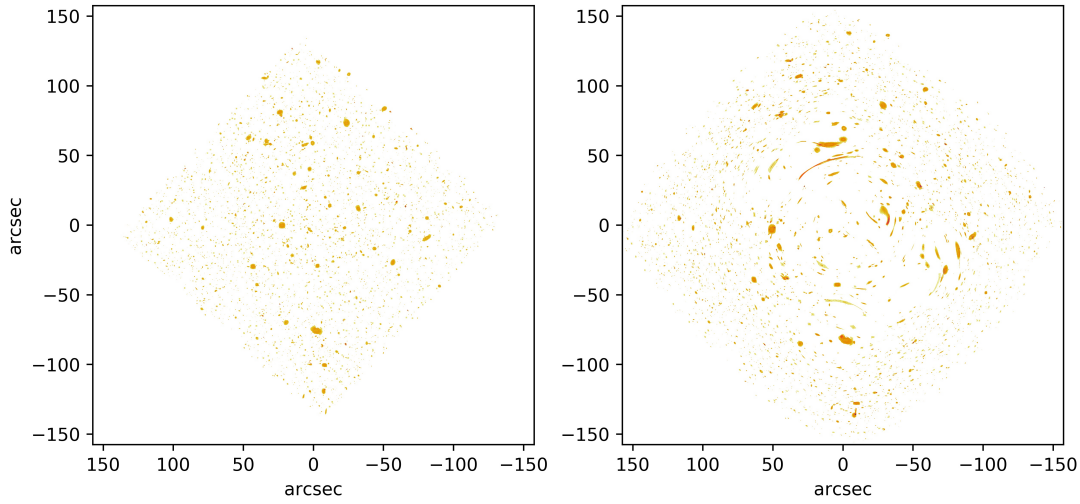

Figure 6.1: Strong lensing of HXDF from A370: The left panel represents the unlensed HXDF. The right panel represents the corresponding lensed HXDF due to the A370. One can see the formation of image formation near swallowtail (giant arc).

lead to detectable differences in the signal observed for different images produced by strong lensing. This, coupled with the coarse localization of signal source in the sky for gravitational wave detections, can make it challenging to identify the common origin of the signal corresponding to different images and use observables like time delay.

6.1 Strong Lensing of HXDF

So far, we have looked at the possibility of detecting image formation near point singularities with the JWST. However, another very exciting idea is to look for these point singularities with Hubble eXtreme Deep Field (HXDF, Illingworth et al., 2013) as a template of the source galaxy distribution. By using HXDF, one can verify the predictions based on different lens mass models. With different magnitude cuts on the lensed HXDF field, one should be able to illustrate why we have only detected a few image formations near point singularities. In this work, we will use HFF cluster lens models provided by the Williams group (discussed in Chapter 3 and 4) as they give the minimum number of point singularities and as they are superposition of a large number of Plummer models, hence, we can have an arbitrary resolution.

The other important part for the lensing of HXDF is the properties of source galaxies in the HXDF. One example of HXDF lensing is presented in Figure 6.1. The left panel represents the unlensed HXDF with the source cutouts taken from Nolan et al. (2020).

The right side panel represents the corresponding lensed HXDF field due to A370. The A370 is situated at $(18.72'', 5.22'')$ and rotated by an angle of 41°. In Nolan et al. (2020), only around half (~ 5200) of the (brightest) sources are considered for their study. But in our work, to get the correct estimates of image formation near point singularities, we need to consider all the sources (~ 10000) from HXDF. From this study, we will also be able to get realistic estimates of the time-delay between multiple images formed near point singularities.

The other obvious extension of the work presented in this thesis is to consider a larger sample of cluster lenses and revisit the cross-section estimations and the effect of uncertainties. From Chapter 4, it is evident that the best-fit mass models reconstructed using Grale will give the lower limit. However, the same cannot be said for the parametric mass models. Hence, it will be exciting to see how the uncertainties in the parametric model parameters affect the point singularity cross-section.

In Mishra et al. (2021), we have studied the effects of microlenses population on the strongly lensed gravitational wave signal. We see that the microlens population can introduce significant modulations in the strongly lensed signal, and these modulations are very sensitive to the strong lens magnification. Following Meena & Bagla (2020a, Chapter 5) and Mishra et al. (2021), we will study the effect of gravitational lensing on gravitational waves signal and the corresponding parameters in highly magnified regions in the galaxy and cluster scale lenses.

Bibliography

Abbott B. P., et al., 2019, Physical Review X, 9, 031040

Abdelsalam H. M., Saha P., Williams L. L. R., 1998, MNRAS, 294, 734

Acebron A., et al., 2018, ApJ, 858, 42

Acebron A., et al., 2019, ApJ, 874, 132

Acebron A., et al., 2020, ApJ, 898, 6

Akeson R., et al., 2019, arXiv e-prints, p. arXiv:1902.05569

Akutsu T., et al., 2018, Progress of Theoretical and Experimental Physics, 2018, 013F01

Arnold V. I., 1983, Catastrophe theory,

Arnold V. I., Shandarin S. F., Zeldovich Y. B., 1982, Geophysical & Astrophysical Fluid Dynamics, 20, 111

Atek H., Richard J., Kneib J.-P., Schaerer D., 2018, MNRAS, 479, 5184

Bagla J. S., 2001, in Brainerd T. G., Kochanek C. S., eds, Astronomical Society of the Pacific Conference Series Vol. 237, Gravitational Lensing: Recent Progress and Future Go. p. 77

Bahé Y. M., 2021, arXiv e-prints, p. arXiv:2101.12112

Baraldo C., Hosoya A., Nakamura T. T., 1999, Phys. Rev. D, 59, 083001

Berry M. V., Upstill C., 1980, Progess in Optics, 18, 257

Biwer C. M., Capano C. D., De S., Cabero M., Brown D. A., Nitz A. H., Raymond V., 2019, PASP, 131, 024503

Blandford R., Narayan R., 1986, ApJ, 310, 568

Blandford R. D., Kochanek C. S., Kovner I., Narayan R., 1989, Science, 245, 824

Bontz R. J., Haugan M. P., 1981, Ap&SS, 78, 199

Borra E. F., 2008, MNRAS, 389, 364

Bowler R. A. A., Jarvis M. J., Dunlop J. S., McLure R. J., McLeod D. J., Adams N. J., Milvang-Jensen B., McCracken H. J., 2020, MNRAS, 493, 2059

Bradač M., Schneider P., Lombardi M., Erben T., 2005, A&A, 437, 39

Broadhurst T., et al., 2005, ApJ, 621, 53

Broadhurst T., Diego J. M., Smoot George I., 2018, arXiv e-prints, p. arXiv:1802.05273

Broadhurst T., Diego J. M., Smoot George F. I., 2019, arXiv e-prints, p. arXiv:1901.03190

Caminha G. B., et al., 2017, A&A, 600, A90

Cerny C., et al., 2018, ApJ, 859, 159

Christian P., Vitale S., Loeb A., 2018, Phys. Rev. D, 98, 103022

Cibirka N., et al., 2018, ApJ, 863, 145

Cirasuolo M., et al., 2007, MNRAS, 380, 585

Cirasuolo M., McLure R. J., Dunlop J. S., Almaini O., Foucaud S., Simpson C., 2010, MNRAS, 401, 1166

Coe D., et al., 2013, ApJ, 762, 32

Coe D., et al., 2019, ApJ, 884, 85

Congdon A. B., Keeton C., 2018, Principles of Gravitational Lensing: Light Deflection as a Probe of Astrophysics and Cosmology

Cowley W. I., Baugh C. M., Cole S., Frenk C. S., Lacey C. G., 2018, MNRAS, 474, 2352

Dai L., Venumadhav T., 2017, arXiv e-prints, p. arXiv:1702.04724

Davies A., Serjeant S., Bromley J. M., 2019, MNRAS, 487, 5263

Deguchi S., Watson W. D., 1986a, Phys. Rev. D, 34, 1708

Deguchi S., Watson W. D., 1986b, ApJ, 307, 30

Diego J. M., 2019, A&A, 625, A84

Diego J. M., Protopapas P., Sandvik H. B., Tegmark M., 2005, MNRAS, 360, 477

Diego J. M., Tegmark M., Protopapas P., Sandvik H. B., 2007, MNRAS, 375, 958

Diego J. M., Hannuksela O. A., Kelly P. L., Pagano G., Broadhurst T., Kim K., Li T. G. F., Smoot G. F., 2019, A&A, 627, A130

Dodelson S., 2003, Modern cosmology

Dodelson S., 2017, Gravitational Lensing

Dyson F. W., Eddington A. S., Davidson C., 1920, Philosophical Transactions of the Royal Society of London Series A, 220, 291

Ebeling H., Stockmann M., Richard J., Zabl J., Brammer G., Toft S., Man A., 2018, ApJL, 852, L7

Einstein A., 1905, Annalen der Physik, 322, 132

Einstein A., 1911, Annalen der Physik, 340, 898

Einstein A., 1915, Sitzungsberichte der Königlich Preußischen Akademie der Wissenschaften (Berlin), pp 831–839

Ellis R. S., 2010, Philosophical Transactions of the Royal Society of London Series A, 368, 967

Gardner J. P., et al., 2006, Space Sci. Rev., 123, 485

Ghosh A., Williams L. L. R., Liesenborgs J., 2020, MNRAS, 494, 3998

Gilmore R., 2007, Catastrophe Theory

Grillo C., et al., 2015, ApJ, 800, 38

Hannuksela O. A., Haris K., Ng K. K. Y., Kumar S., Mehta A. K., Keitel D., Li T. G. F., Ajith P., 2019, ApJL, 874, L2

Haris K., Mehta A. K., Kumar S., Venumadhav T., Ajith P., 2018, arXiv e-prints, p. arXiv:1807.07062

Hartle J. B., 2003, Gravity : an introduction to Einstein's general relativity

Hawking S. W., Ellis G. F. R., 1973, The large-scale structure of space-time

Hidding J., Shandarin S. F., van de Weygaert R., 2014, MNRAS, 437, 3442

Hoag A., et al., 2016, ApJ, 831, 182

Hogg D. W., 1999, arXiv e-prints, pp astro–ph/9905116

Hongsheng Z., Xilong F., 2018, arXiv e-prints, p. arXiv:1809.06511

Illingworth G. D., et al., 2013, ApJS, 209, 6

Ishigaki M., Kawamata R., Ouchi M., Oguri M., Shimasaku K., Ono Y., 2015, ApJ, 799, 12

Ivezić Ž., et al., 2019, ApJ, 873, 111

Jaki S. L., 1978, Foundations of Physics, 8, 927

Jauzac M., et al., 2014, MNRAS, 443, 1549

Jauzac M., et al., 2015, MNRAS, 452, 1437

Johnson T. L., Sharon K., Bayliss M. B., Gladders M. D., Coe D., Ebeling H., 2014, ApJ, 797, 48

Jullo E., Kneib J. P., Limousin M., Elíasdóttir Á., Marshall P. J., Verdugo T., 2007, New Journal of Physics, 9, 447

Kassiola A., Kovner I., Fort B., 1992, ApJ, 400, 41

Kawamata R., Ishigaki M., Shimasaku K., Oguri M., Ouchi M., Tanigawa S., 2018, ApJ, 855, 4

Kelly P. L., et al., 2016, ApJL, 819, L8

Kelly P. L., et al., 2018, Nature Astronomy, 2, 334

Kennefick D., 2019, No Shadow of a Doubt: The 1919 Eclipse That Confirmed Einstein's Theory of Relativity. Princeton University Press

Kneib J.-P., Natarajan P., 2011, A&A Rev., 19, 47

Kochanek C. S., 2006, arXiv e-prints, pp astro–ph/0407232

Kovner I., 1987, ApJ, 321, 686

Lai K.-H., Hannuksela O. A., Herrera-Martín A., Diego J. M., Broadhurst T., Li T. G. F., 2018, Phys. Rev. D, 98, 083005

Lam D., Broadhurst T., Diego J. M., Lim J., Coe D., Ford H. C., Zheng W., 2014, ApJ, 797, 98

Laureijs R., 2009, arXiv e-prints, p. arXiv:0912.0914

Lawrence J. K., 1971, Nuovo Cimento B Serie, 6B, 225

Lewis A., Challinor A., 2006, Phys. Reports, 429, 1

Li S.-S., Mao S., Zhao Y., Lu Y., 2018, MNRAS, 476, 2220

Liao K., Biesiada M., Fan X.-L., 2019, ApJ, 875, 139

Liesenborgs J., de Rijcke S., Dejonghe H., Bekaert P., 2007, MNRAS, 380, 1729

Liesenborgs J., Williams L. L. R., Wagner J., De Rijcke S., 2020, MNRAS, 494, 3253

Lorentz H. A., 1952, The Principle of Relativity: a collection of original memoirs on the special and general theory of relativity

Lotz J. M., et al., 2017, ApJ, 837, 97

Mahler G., et al., 2019, ApJ, 873, 96

Matsunaga N., Yamamoto K., 2006, Journal of Cosmology and Astroparticle Physics, 2006, 023

McCully C., Keeton C. R., Wong K. C., Zabludoff A. I., 2014, MNRAS, 443, 3631

McLeod D. J., McLure R. J., Dunlop J. S., Robertson B. E., Ellis R. S., Targett T. A., 2015, MNRAS, 450, 3032

Meena A. K., Bagla J. S., 2020a, MNRAS, 492, 1127

Meena A. K., Bagla J. S., 2020b, MNRAS, 492, 3294

Meena A. K., Bagla J. S., 2021, MNRAS,

Meneghetti M., et al., 2017, MNRAS, 472, 3177

Meneghetti M., et al., 2020, Science, 369, 1347

Merten J., et al., 2011, MNRAS, 417, 333

Michell J., 1784, Philosophical Transactions of the Royal Society of London, 74, 35

Mishra A., Meena A. K., More A., Bose S., Singh Bagla J., 2021, arXiv e-prints, p. arXiv:2102.03946

Misner C. W., Thorne K. S., Wheeler J. A., 1973, Gravitation

Mohammed I., Saha P., Williams L. L. R., Liesenborgs J., Sebesta K., 2016, MNRAS, 459, 1698

Mortlock A., McLure R. J., Bowler R. A. A., McLeod D. J., Mármol-Queraltó E., Parsa S., Dunlop J. S., Bruce V. A., 2017, MNRAS, 465, 672

Moutard T., Sawicki M., Arnouts S., Golob A., Coupon J., Ilbert O., Yang X., Gwyn S., 2020, MNRAS, 494, 1894

Nakamura T. T., 1998, Phys. Rev. Lett., 80, 1138

Nakamura T. T., Deguchi S., 1999, Progress of Theoretical Physics Supplement, 133, 137

Narayan R., Bartelmann M., 1996, arXiv e-prints, pp astro–ph/9606001

Newton Isaac S., 1952, Opticks

Nityananda R., 1990, Pictures of gravitational lensing. pp 1–12, doi:10.1007/BFb0009226

Nolan L., Mechtley M., Windhorst R., Knierman K., Ashcraft T., Cohen S., Tompkins S., Will L., 2020, arXiv e-prints, p. arXiv:2012.09994

Oguri M., 2010, PASJ, 62, 1017

Ohanian H. C., 1974, International Journal of Theoretical Physics, 9, 425

Okabe T., et al., 2020, MNRAS, 496, 2591

Ono Y., et al., 2018, PASJ, 70, S10

Orban de Xivry G., Marshall P., 2009, MNRAS, 399, 2

Paraficz D., Kneib J. P., Richard J., Morandi A., Limousin M., Jullo E., Martinez J., 2016, A&A, 594, A121

Paterno-Mahler R., et al., 2018, ApJ, 863, 154

Petters A. O., Levine H., Wambsganss J., 2001, Singularity theory and gravitational lensing

Piórkowska A., Biesiada M., Zhu Z.-H., 2013, Journal of Cosmology and Astroparticle Physics, 2013, 022

Planck Collaboration et al., 2020, A&A, 641, A6

Priewe J., Williams L. L. R., Liesenborgs J., Coe D., Rodney S. A., 2017, MNRAS, 465, 1030

Raney C. A., Keeton C. R., Brennan S., Fan H., 2020, MNRAS, 494, 4771

Refsdal S., 1964a, MNRAS, 128, 295

Refsdal S., 1964b, MNRAS, 128, 307

Refsdal S., 1966a, MNRAS, 132, 101

Refsdal S., 1966b, MNRAS, 134, 315

Remolina González J. D., Sharon K., Mahler G., 2018, ApJ, 863, 60

Roberts D. H., Greenfield P. E., Hewitt J. N., Burke B. F., Dupree A. K., 1985, ApJ, 293, 356

Robertson A., 2021, arXiv e-prints, p. arXiv:2101.12067

Rodney S. A., et al., 2015, ApJ, 811, 70

Rosswog S., 2015, International Journal of Modern Physics D, 24, 1530012

Ryder L., 2009, Introduction to General Relativity

Schechter P., 1976, ApJ, 203, 297

Schneider P., 1985, A&A, 143, 413

Schneider P., 2005, arXiv e-prints, pp astro–ph/0509252

Schneider P., Weiss A., 1986, A&A, 164, 237

Schneider P., Ehlers J., Falco E. E., 1992, Gravitational Lenses

Sendra I., Diego J. M., Broadhurst T., Lazkoz R., 2014, MNRAS, 437, 2642

Sereno M., Sesana A., Bleuler A., Jetzer P., Volonteri M., Begelman M. C., 2010, Phys. Rev. Lett., 105, 251101

Sereno M., Jetzer P., Sesana A., Volonteri M., 2011, MNRAS, 415, 2773

Smith G. P., et al., 2009, ApJL, 707, L163

Smith G. P., Jauzac M., Veitch J., Farr W. M., Massey R., Richard J., 2018, MNRAS, 475, 3823

Soldner J., 1804, Berliner Astronomisches Jahrbuch, p. 161

Stewart I., 1982, Reports on Progress in Physics, 45, 185

Suyu S. H., Halkola A., 2010, A&A, 524, A94

Takahashi R., 2017, ApJ, 835, 103

Takahashi R., Nakamura T., 2003, ApJ, 595, 1039

Ulmer A., Goodman J., 1995, ApJ, 442, 67

Varvella M. A., Angonin M. C., Tourrenc P., 2004, General Relativity and Gravitation, 36, 983

Vega-Ferrero J., Diego J. M., Bernstein G. M., 2019, MNRAS, 486, 5414

Virbhadra K. S., Ellis G. F. R., 2000, Phys. Rev. D, 62, 084003

Walsh D., Carswell R. F., Weymann R. J., 1979, Nature, 279, 381

Wambsganss J., 2006, arXiv e-prints, pp astro–ph/0604278

Wei J.-J., Wu X.-F., 2017, MNRAS, 472, 2906

Weinberg S., 1972, Gravitation and Cosmology: Principles and Applications of the General Theory of Relativity

Will C. M., 1988, American Journal of Physics, 56, 413

Williams C. C., et al., 2018a, ApJS, 236, 33

Williams L. L. R., Sebesta K., Liesenborgs J., 2018b, MNRAS, 480, 3140

Wood A., Mao S., 2005, MNRAS, 362, 945

Yuan T. T., Kewley L. J., Swinbank A. M., Richard J., 2012, ApJ, 759, 66

Yung L. Y. A., Somerville R. S., Finkelstein S. L., Popping G., Davé R., 2019, MNRAS, 483, 2983

Zheng W., et al., 2012, Nature, 489, 406

Zitrin A., Broadhurst T., 2009, ApJL, 703, L132

Zitrin A., et al., 2009, MNRAS, 396, 1985

Zitrin A., et al., 2010, MNRAS, 408, 1916

Zitrin A., et al., 2013, ApJL, 762, L30

Zwicky F., 1937a, Phys. Rev., 51, 290

Zwicky F., 1937b, Phys. Rev., 51, 679

de Laplace P., 1795, Exposition Du Systême Du Monde